IntechOpen

Proceedings of the 4th International Conference on Innovations in Automation and Mechatronics Engineering

Edited by Sanket N. Bhavsar, Anand Y. Joshi and Ketan M. Tamboli

Proceedings of the 4th International Conference on Innovations in Automation and Mechatronics Engineering

Edited by Sanket N. Bhavsar, Anand Y. Joshi and Ketan M. Tamboli

Published in London, United Kingdom







IntechOpen






Supporting open minds since 2005

Proceedings of the 4th International Conference on Innovations in Automation and Mechatronics Engineering
http://dx.doi.org/10.5772/intechopen.76640
Edited by Sanket N. Bhavsar, Anand Y. Joshi and Ketan M. Tamboli

First published in London, United Kingdom, 2019 by IntechOpen
eBook (PDF) Published by IntechOpen, 2019
IntechOpen is the global imprint of INTECHOPEN LIMITED, registered in England and Wales, registration number: 11086078, The Shard, 25th floor, 32 London Bridge Street
London, SE19SG – United Kingdom
Printed in Croatia

British Library Cataloguing-in-Publication Data
A catalogue record for this book is available from the British Library

Additional hard and PDF copies can be obtained from orders@intechopen.com

Proceedings of the 4th International Conference on Innovations in Automation and Mechatronics Engineering (ICIAME2018)
Edited by Sanket N. Bhavsar, Anand Y. Joshi and Ketan M. Tamboli
p. cm.
Print ISBN 978-1-78985-297-4
Online ISBN 978-1-78985-298-1
eBook (PDF) ISBN 978-1-83962-030-0

Preface

The Mechatronics Department (Accredited by National Board of Accreditation, New Delhi, India) of the G H Patel College of Engineering and Technology, Gujarat, India arranged the 4th International Conference on Innovations in Automation and Mechatronics Engineering 2018, (ICIAME 2018) on 2–3 February 2018. This gathering was in continuation of the past effective three conferences ICIAME–2016, ICIAME–2014 and ICIAME–2013. The conference was financially supported by the All India Council of Technical Education (AICTE), New Delhi, India and Charutar Vidya Mandal (CVM), Gujarat. In this regard, the determination and peer-review of the papers has been finished thanks to the joint effort of the Scientific and Organizing Committees. It is believed that the outcomes of this conference will lead to solving several multidisciplinary issues in society.

The papers presented during the conference were based on Automation, Optimization, Computer Aided Design and Manufacturing, Nanotechnology, Solar Energy etc.

The keynote discourses were conveyed in ICIAME–2018 by Professor S.K.Saha of IIT Delhi on "Robotics and Automation in India" and by Dr. M.K.Gupta, Engineering Design and Analysis Group, Institute for Plasma Research (IPR), Gandhinagar, Gujarat, India on "Mechatronics Drivers in Research".

We trust that the speakers and the representatives had a productive trade and engaged in dialogues on specialized and logical improvements and issues amid the gathering. We would like to thank all included individuals who enabled us to enhance the nature of the papers at high worldwide standard level. The organizing panel is especially appreciative to the Chairman, Charutar Vidya Mandal and All India Council for Technical Education (AICTE), New Delhi, for subsidizing the gathering. We would like to thank the Advisory committee members and commentators for their unequalled help and delegates for their commitments to making this meeting an effective one.

Dr. Sanket N. Bhavsar
Professor & Head

Dr. Anand Y. Joshi
Professor

Dr. Ketan M. Tamboli
Associate Professor

Mechatronics Department
G. H. Patel College of Engineering and Technology
Bakrol Road, Vallabh Vidyanagar – 388120, Gujarat, India

ORGANIZING COMMITTEE

Conference Patron

Dr. C. L. Patel
Chairman, Charutar Vidya Mandal

Conference Chairman

Dr. Himanshu B. Soni
Principal
G. H. Patel College of Engineering and Technology

Conference Convener

Dr. Sanket N. Bhavsar
Head, Mechatronics Department
G. H. Patel College of Engineering and Technology

Organizing Secretaries

Dr. Anand Y. Joshi
Dr. Ketan M. Tamboli

Organizing Committee Members

Dr. Vinod N. Patel
Dr. Yogesh A. Chauhan
Prof. Saurin M. Sheth
Dr. Ajay M. Patel
Prof. Sandip C. Patel
Prof. Pathik P. Patel
Prof. Tejas D. Patel
Prof. Bhavik A. Ardeshana
Prof. Umang B. Jani

G H PATEL COLLEGE OF ENGINEERING AND TECHNOLOGY
VALLABH VIDYANAGAR – 388120

Mechatronics Department

Vision

The department aims to educate students in global standards by way of imparting the responsible, worthy, and exploratory approach, and thereby enabling them to face industrial challenges in the ever-changing technical era by providing a platform to learn and execute the multidisciplinary subjects with focus on Design, Control and Automation aspects.

Mission

To accomplish our vision of everlasting improvement, the Mechatronics Programme has the prime mission of providing a high-quality education with

M1. A curriculum that provides synergistic integration of engineering fundamentals with theory and applications.

M2. The faculty committed to offer their broad and practical experience that will promote professional growth and prepare students for a variety of engineering careers, graduate studies, and continuing education.

M3. Project experiences that build on fundamentals and develop innovative ideas for betterment of society.

M4. Interdisciplinary facilities and equipment that are readily accessible.

M5. An environment that is conducive to learning and encourages students from different genders and backgrounds.

Programme educational objectives

Programme educational objectives of the Mechatronics Department are best outlined in terms of goals for its graduates. Graduates from the Mechatronics Department will be:

PE01. Effective multidisciplinary engineers, well educated in the basic engineering sciences and fundamentals of mechanical, electrical, electronics and control engineering.

PE02. Capable of designing, analyzing, manufacturing and testing “smart” and “eco friendly” products with help of controllers, sensors and actuators to build a digital India.

PE03. Knowledgeable, good presenter, active team member, effective leader, individual responsible citizen and ambitious to secure high merit to make them employable.

Programme outcomes

Mechatronics Programme graduates have the ability to:

1. Use knowledge of mathematics, science, and mechatronic engineering to frame and unravel problems.

2. Exhibit the knowledge of electrical and electronic circuits, control system, logic design and image processing using hardware and soft programming for automation.

3. Demonstrate the knowledge of statics, dynamics and solid mechanics related to Mechatronics systems.

4. Synthesize and analyze mechanisms which integrate computers, sensors, and actuators to meet the needs for evaluating system performance with respect to specifications.

5. Understand general engineering and production fundamentals by experimental studies.

6. Use of current industry / shop floor standard using various engineering tools.

7. Understand the fundamentals of management, optimization and current standards and developments on the front of quality assurance and reliability.

8. Converse technical matters efficiently in oral, written, and graphical form.

9. Function independently to prove their knowledge of multiple disciplines of engineering.

10. Understand their professional and ethical responsibilities, the impact of their activities on society and the environment, and appreciate contemporary issues facing society.

11. Use information resources and recognize the importance of continued learning.

Chapter

Effect of Variable Process Parameter on Ultimate Tensile Strength and Elongation of Aluminum Alloy AA7075 T6 Welded Plate Joints

Vrajesh Patel, Tejas Chauhan and Nikul Patel

Abstract

Aluminum alloy is currently widely used for structural purposes because of its unique properties. In this research work, we weld aluminum alloy plates using FSW with different process variable parameters such as tool pin geometry, traverse speed, and tool rotating speed. Three types of FSW tool pin geometry (square pin, cylindrical straight pin and threaded straight cylindrical pin) and three different speeds (tool traverse speed and tool rotation speed) were selected. For analyzing the effect of process parameter, we carried out a tensile test to measure UTS along with elongation of the welded joint.

1. Introduction

In 1991, friction stir welding (FSW) was discovered by Thomas [1] and this is very useful for welding non-ferrous materials (for example, aluminum and magnesium) and this process solved many problems related to traditional welding techniques.

All industries associated with fabrication are under pressure to produce stronger and lighter products from metals whilst having lower energy consumption, less contamination of harmful material to the environment, producing at a low cost and producing faster than before. FSW is a solid-state joining process that requires less energy. Its mechanical process is able to produce high strength welding between different materials (similar and dissimilar) and it offers a possibly lower-cost solution, therefore solving the above challenges.

2. Literature survey

Hard and brittle stir zone (SZ) of welds obtained by polygonal pin geometry were compared to cylindrical pin geometry for equal shoulder bottom face [2]. The peak temperature during the welding process increased with an increase of tool speed and decreased with an increase in the welding speed for all shoulder diameters [3]. The welding process depends on heat generation and the heat is caused by friction between

the tool shoulder and the plate surface. High friction leads to high heat which lead to good welding (defect-free welding) using different variable welding process parameters [4]. Square pin tool geometry allows for better mechanical properties followed by hexagonal, octagonal pin tool profile [5]. Defects such as tunnel defect, cracks, pin holes, are due to unsuitable and inadequate flow of metal in the area [6]. The thermal cycle (hot to cold) is what increases the welding (mechanical) properties. Heat generation is strongly corelated to all post-weld mechanical properties [7]. Tensile strength (TS) of the dissimilar aluminum plates (AA6061-T651 plate) increases when heat input is lower and the good slurry from both the materials joined can be created at lower welding temperatures and higher tool rotating speeds [8]. Due to friction, heat generation occurred and plastic flow grain reordering occurred and the weld has been achieved [9]. When welding thermoplastic materials, it is found that the weld zone created using the threaded pin profile tool required less force. Square, triangular and grooved with square pin geometry created a defect-free weld with the same process variable parameter [10]. The overall response of mechanical properties is contingent on the ratio of the tool rotating speed to the tool travel speed [11]. Preheating of the plates is advantageous for refining the quality of the weld as well as an increase in the tool travel speed for material with a higher melting point such as steel [12].

3. Material and tool selection

3.1 Plate material

In this research work, we selected aluminum alloy AA7075 T6 plates for the experiments. The chemical composition of this material is shown in **Table 1**. The size of the plate for experiments 150 × 100 × 6 mm based on a literature survey and requirements of tensile test specimen as per the standards.

3.2 Tool material

For the joining of the aluminum alloy plate, the FSW tool was made from H13 material. This is suitable for machining as well as having enough strength for FSW. The following (**Tables 2** and **3**) show the chemical composition and mechanical properties of the plate material before welding. General dimensions for the FSW tool are shoulder diameter, length and pin length as 18, 25 and 5.8 mm respectively with pin diameter 6 mm. Three tool pin geometries were used [threaded straight cylindrical pin (TSCP), straight cylindrical pin (SCP) and square pin (SP)]. All these tools were made on conventional lathe machines at the GIDC, Vallabh Vidyanagar.

Element	Al	Zn	Si	Mg	Cu	Fe	Mn	Cr	Ni	Pb	Ti
Percentage	89.7	5.78	0.05 Max	2.69	1.3	0.5	0.03 Max	0.2	0.01	0.01	0.06

Table 1.
Chemical composition of plate material (according to ASTM E 8).

Element	Cr	V	Mr	Mo	Si	C	Cu	Ni	P	S
Content (%)	4.75–5.50	0.80–1.20	0.20–0.50	1.10–1.75	0.80–1.20	0.32–0.45	0.25	0.3	0.03	0.3

Table 2.
Chemical composition of H13.

Element	Density (lb./in^3)	Specific gravity	Machinability
Content	0.280	7.75	65–70%

Table 3.
Mechanical properties of H13.

4. Experiment

For experiment purpose, we select three tool rotation speed (710 rpm, 960 rpm, and 1400 rpm) and welding speed ranges from 60 to 140 mm/min based on literature survey. In this investigation, there are three variable parameters selected (and performed experiments based on different combination), and the remaining parameters are kept constant. All nine experiments were carried out to find the suitable parameter combination that gives high tensile strength at the joint. The process parameters for the eight experiments are shown in **Table 4**.

A conventional vertical milling machine was used to perform the experiments. Aluminum alloy plates were mounted on the machine work table with the help of a base plate, four clamps and nut screws that were tightened by spanner (shown in **Figures 1** and **2**). All experiments were carried out after setting the process parameter according to **Table 4**.

Experiment no.	Tool rotating speed (rpm)	Welding speed (mm/min)	FSW tool
1	1400	140	TSCP
2	960	90	TSCP
3	710	105	TSCP
4	1400	125	SCP
5	960	80	SCP
6	960	60	SCP
7	1400	85	SP
8	710	105	SP

Table 4.
Variable process parameter.

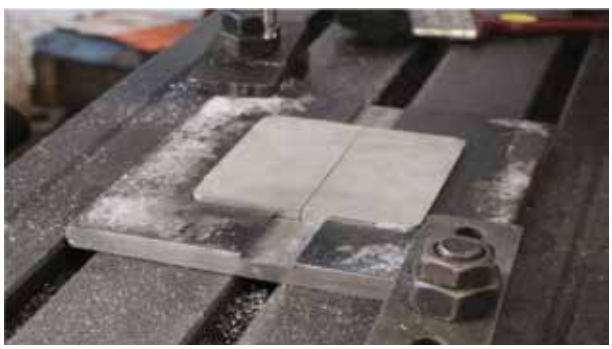

Figure 1.
Base plate and plate set-up.

Figure 2.
Welding of Al alloy 7075 T6.

The test specimen for tensile test was cut from the welded plates as per the ASTM E-8 standard for 6 mm plate thickness for aluminum alloy. Overall length of the test specimen is 100 mm.

5. Result and discussion

Testing of the welded plates carried out as per the standard procedure for measuring ultimate tensile strength (UTS) and yield strength (YS). **Figure 3** shows the specimen before the tensile test, which are cut from the welded plates. All the test specimens brokenearer to the weld zone, which is shown in **Figures 4–6** and the results of the tensile specimen are shown in **Table 5**.

From the results of tensile testing, we can easily see that the UTS values obtained for the three different pin geometries are different. The results of the square pin

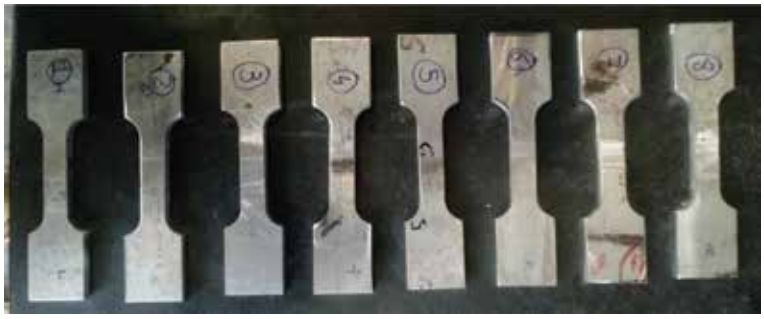

Figure 3.
Tensile test specimen.

Figure 4.
Tested specimen.

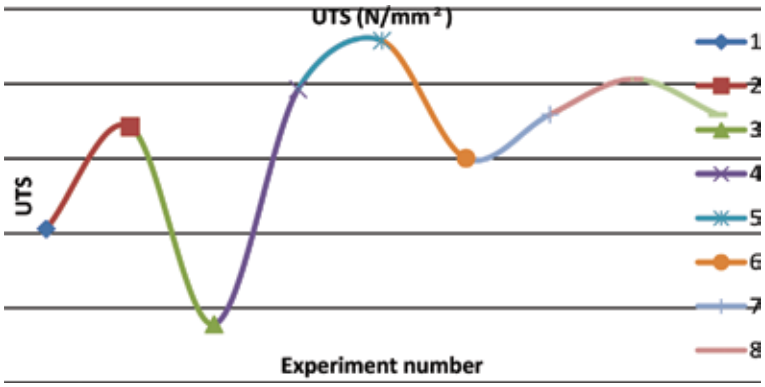

Figure 5.
Graph of experiment VS UTS.

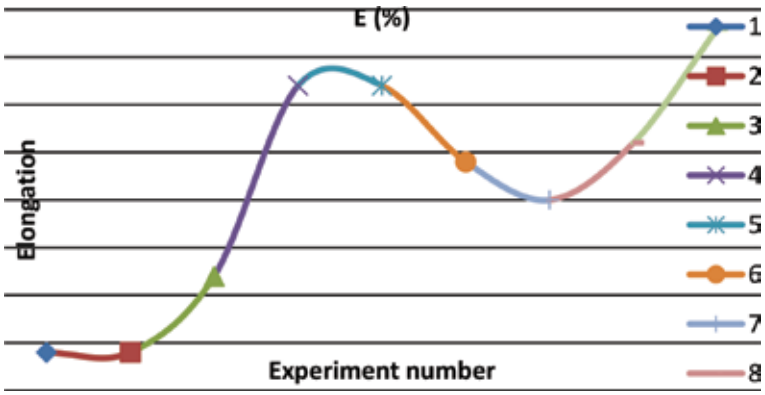

Figure 6.
Graph of experiment VS elongation.

Experiment no.	FSW tool	UTS (N/mm^2)	YS (N/mm^2)	Elongation (%)
1	TSCP	103.1	60.39	0.4
2	TSCP	171.36	84.56	0.4
3	TSCP	39.28	0.244	1.2
4	SCP	196.45	164.92	3.2
5	SCP	228.96	26.72	3.2
6	SCP	150.19	137.11	2.4
7	SP	179.44	90.94	2
8	SP	203.18	200.26	2.6

Table 5.
Tensile testing result.

and straight cylindrical pin gave better results compared to the threaded straight cylindrical pin. Material flow during the welding from the advancing side to the retracting side was good when using the square pin profile because the percentage elongation is highest in the square pin profile. When we are observing the results of elongation for experiments 4, 5, and 6, the heat generation is higher with the increasing tool rotation speed. The results of experiment 5 for UTS shows that the

straight cylindrical pin profile gave better results at a low speed with high traverse speed. For generating heat, friction is necessary and if the traverse speed is more with high rotation speed then proper bonding of the two plates does not happen and the joint strength reduces as was observed in the results of experiment 1.

6. Conclusions

FSW is a solid state welding process, where the joining of two plates is performed under recrystallize temperature. Our experiment on aluminum alloy AA 7075 T6 tested different welding parameters, such as welding speed, tool rotating speed ranging from 710 to 1400 rpm, welding speed (tool travel speed) ranging from 60 to 140 mm/min, and three tool pin geometries such as square pin, cylindrical straight pin, and cylindrical threaded straight pin.

From the tensile test results, we obtained a 228.96 UTS at TRS of 710 rpm, WS of 105 mm/min with the square pin.

Author details

Vrajesh Patel, Tejas Chauhan and Nikul Patel*
Ipcowala Institute of Engineering and Technology (IIET), Dharmaj, Gujarat, India

*Address all correspondence to: nikpatel25@yahoo.com

References

[1] Thoas WM, Nicholas ED, Needham JC, Murch MG, Temple SP, Dawes CJ. Friction Stri Butt Welding. International Patent Application No PCT/GB92/02203. 1998

[2] Mehta KP, Badheka V. Influence of tool pin design on properties of dissimilar copper to aluminum friction stir welding. 2017;**27**

[3] Venkateshwarlu G, Harishkumar C. Simulation study of friction stir weld aluminum 7075 alloy. 2016;**4**

[4] Patel N, Bhatt KD, Mehta V. Influence of tool pin profile and welding parameter on tensile strength of magnesium alloy AZ91 during FSW. 2016;**23**

[5] Singh DP, Singh V, Kumar S. Optimization of process parameters for friction stir welded aa7075 composite joints by Taguchi method. 2016;**4**(1)

[6] Bayazid SM, Farhangi H, Ghahramani A. Effect of pin profile on defects of friction stir welded 7075 aluminum alloy. 2015;**11**

[7] Dickson SB. An investigation of friction stir welding parameter effects on post weld mechanical properties in 7075AA. 2015

[8] Ravikumar S, Seshagiri Rao V, Pranesh RV. Effect of process parameters on mechanical properties of friction stir welded dissimilar materials between aa6061-t651 and aa7075-t651 alloys. 2014;**4**

[9] Venugopal T, Srinivasa Rao K, Prasad Rao K. Studies on friction stir welded AA 7075 aluminum alloy. 2014;**57**

[10] Panneerselvam K, Lenin K. Investigation on effect of tool forces and joint defects during FSW polypropylene plate. 2012;**38**

[11] Biswas P, Kumar DA, Mandal NR. Friction stir welding of aluminum alloy with varying tool geometry and process parameters. 2011;**226**

[12] Mishra RS, Ma ZY. Friction stir welding and processing. 2005;**50**

Chapter

Water Desalination Using Offset Solar Parabolic Dish Concentrator: A Review

Heman M. Pandya, C. O. Yadav and P. V. Ramana

Abstract

Few desalination systems exist that are not energy intensive and which do not utilize any conventional sources of energy. There is a great potential to be harnessed through solar energy and thermal desalination is one such process with little investment and the potential to produce potable water for up to 5–10 years at the least. Efforts have been made to make solar distillation systems cheaper and more capable of achieving higher yields of distilled water. An offset parabolic dish works on the principle of concentrating solar power technology, which generates higher distilled water yields with lower production costs. This review paper summarizes the optimum feasible design options available for manufacturing the offset parabolic dish concentrator for desalination purposes. The construction and performance of offset parabolic dish concentrator depends on several key features such as reflecting materials used for the concentrator, shape, size of the aperture area of the concentrator, diameter of dish concentrator, focal length of the offset parabolic dish concentrator, geometric concentration ratio (CR), and rim angle.

Keywords: offset parabolic dish concentrator, Scheffler dish, concentrating solar power (CSP), water distillation, desalination unit, small-scale solar still

1. Introduction

The solar water desalination process is one of the best and low-cost routes to obtain potable water through evaporation and condensation.

There have been 400 million people who have used desalinated water in 2015 and it was reported by Dr. Md. Eaqub Ali that by 2025, 14% of the global population would be forced to use sea water. By 2030, the global water demand will be 16,900 billion m^3 (Bnm^3) and 2400 Bnm^3 shortfalls of water would be generated. This water shortfall can be provided by various desalination processes [1].

There are four types of parabolic dishes: (a) Axial or front feed prime focus parabolic dish, (b) Offset parabolic dish, (c) Cassegrain, and (d) Gregorian parabolic dish.

The offset parabolic shape eliminates aperture blockage and prevents the accumulation of ice and snow by placing the receiver below the dish reflective aperture region. The offset dish is a portion of a much larger paraboloid. The reflector/concentrator is an asymmetric segment of a paraboloid, so the focus is

located on the side and does not record a shadow as in the front receiver dish. In the offset design, the receiver is positioned outside on a boom sticking out from the bottom edge of the dish.

The offset-axis dish design offers several distinct advantages over its prime focus counterpart. There is no receiver blockage and this is an important consideration when the reflecting aperture is less than 1 m in diameter. Better stability and lower wind resistance is provided by this shape (geometry).

Certain disadvantages also exist with solar based dish systems, such as these systems need tracking, they tend to be the more expensive option when compared to non-tracking desalination systems. In addition, maintenance of the system, such as timely seasonal changes in the tracking system for proper altitude tracking, also requires skilled technical personnel.

Wear and tear of the abrasive film and replacement of broken reflecting glass or regular removal of dust from the surfaces of the concentrator are a few of the issues present in almost all concentrating solar technologies.

2. Literature review

- Hafton Asmelash et al. [2] designed and developed an offset dish concentrator with the dimensions of 90 cm (major dia.) by 80 cm (minor dia.), for the purpose of cooking. Its maximum temperature of 94°C was achieved within 25 min with water in the cooking vessel. With such encouraging results, it can also be used in many other applications in the future.

- Pavlovic et al. [3] presented the method of designing, constructing and performing optical ray tracing analysis of a solar concentrator for medium temperature applications. In order to minimize the design efforts, they decided to utilize a commonly available offset parabolic antenna dish as their reflector. Their reflector was made from combining three individual offset parabolic antenna dishes. The total heat flux recorded at the focal region was 2188 W.

- Munir et al. [4] presented a simple and tangible method to construct the Scheffler concentrator with an 8 m^2 surface area. In their paper, they have presented step-by-step analytical calculations to design the dish concentrators' parabolic curve and its elliptical frame. Their design offered a new prospect of potential application in the domestic market.

- Chandak et al. [5] designed, developed, and experimented with a multistage evaporation system using a Scheffler solar concentrator. They obtained 2.3 times more distilled water output from their system as compared to that of a single stage distillation unit. They concluded that the Scheffler dish design was promising for the commercial scale application.

- Gadhia and Kinjavedkar [6] focused on giving a comprehensive review of solar reflector technologies. Their findings proved that when mirror is used as a reflective material in a Scheffler dish, the best results were obtained.

- Bhasme [7] studied the performance of a parabolic solar reflector and Scheffler solar reflector for their thermal efficiency and losses. The main

Major features	References	Focus	Methodology
Dish concentrator shape and diameter	[8]	Circular shaped dish having 5, 10 and 20 m dish diameters	Theoretical
	[9]	Spherical shaped solar dish having 25 m dish diameter	Experimental
Reflector material	[10]	Polished stainless steel 0.5 mm thickness reflector surface	Theoretical
Focal length	[10]	Parabolic square dish with focal length of 1 m	Theoretical
Rim angle	[10]	Parabolic square dish having a 44.5° rim angle	Theoretical
Solar radiation	[11]	Paraboloid shaped dish was analyzed using Monte-Carlo ray tracing method and Computational Fluid Dynamics (CFD) method	Numerical
Concentration ratio	[12]	Triangular facets Solar dish concentrator with a mean concentration ratio of 333.5	Theoretical

Table 1.
Seven major features of offset parabolic dish design in foregoing research.

dependent factors in her comparative analysis were: (a) the geometry of the reflectors having a diameter of 1.5 m and (b) the radiation of the sun. For better reflectivity in both receiver and concentrator, stainless steel was used. She utilized Matlab Simulink software to compare the Scheffler dish concentrating ratio to that of a parabolic dish collector. The results showed an 8% better efficiency of the Scheffler reflector when compared to the parabolic collector.

2.1 Major features affecting the design of the offset parabolic dish concentrator

Table 1 summarizes seven key features that make a significant difference to the design of the offset solar parabolic dish concentrator.

The diameter of the dish determines the power or heat flux generated by the parabolic dish. This value is usually decided so that minimum solar radiation of 600–1000 W/m^2 is collected [13]. Concentration ratio greater than 10 is advisable in any solar dish design. Researchers in Ref. [13] reported that rim angle values near 45° lead to the highest concentration ratio and better thermal performance of CSP systems.

3. Conclusions

This feasibility study brings forward the various factors that affect the solar offset parabolic dish when using it as an independent single desalination unit. We can establish certain design parameters that are responsible for obtaining optimal performance from the offset parabolic dish systems. These features are rim angle, the reflective material used for the concentrator, shape of the dish concentrator, and the concentration ratio.

Using a solar offset parabolic dish as a reflector improves temperature concentration at the focal point (point focus) with minimum cosine losses when compared to prime focus parabolic dish systems. There is a low yield problem when making use of solar energy for production of potable water in the form of a stand-alone distillation unit.

Researchers have worked on designs based on the offset type of dish geometry. Although this technology can be made available on a smaller scale, there seems to be a shortage of exploration. As of today, scarcely any reported research works on concentrating solar power for desalination process with smaller aperture area of 1–2 m^2 range are available.

Author details

Heman M. Pandya*, C. O. Yadav and P. V. Ramana
Mechanical Engineering Department, Sardar Vallabhbhai Patel Institute of Technology (SVIT), Vasad, Gujarat, India

*Address all correspondence to: hemanpandya82@gmail.com

References

[1] Chandrashekara M, Yadav A. Water desalination system using solar heat: A review. Renewable and Sustainable Energy Reviews. 2017;**67**:1308-1330. DOI: 10.1016/j.rser.2016.08.058

[2] Asmelash H, Kebedom A, Bayray M, Mustofa A. Performance investigation of offset parabolic solar cooker for rural appplications. International Journal of Engineering Research & Technology. 2014;**3**(12):2278-0181

[3] Pavlovic S, Stefanovic V, Mancic M, Spasic Z. Development of mathematical model of offset type solar parabolic concentrating collector. Annals of the Faculty of Engineering Hunedoara. 2016;**14**(1):19

[4] Munir A, Hensel O, Scheffler W. Design principle and calculations of a Scheffler fixed focus concentrator for medium temperature applications. Solar Energy [Internet]. Elsevier BV. 2010;**84**(8):1490-1502. DOI: 10.1016/j.solener.2010.05.011

[5] Chandak A, Dubey D, Kulkarni R. Development of 2.3 m dia. In: Solar Community Dish Cooker, Presented at Asia Regional Workshop on Solar Cooking and Food Processing; Apr 2007; Kathmandu, Nepal; 2007. pp. 16-17

[6] Gadhia D, Kinjavedkar C. Comprehensive review of solar reflectors technologies. Sun Focus. 2014;**2**(1):13-16

[7] Bhasme S. Comparative evaluation of parabolic collector and Scheffler reflector for solar cooking. International Journal of Engineering. 2016;**9**(1):1-16

[8] Hijazi H, Mokhiamar O, Elsamni O. Mechanical design of a low cost parabolic solar dish concentrator. Alexandria Engineering Journal. 2016;**55**(1):1-1. DOI: 10.1016/j.aej.2016.01.028

[9] Lovegrove K, Burgess G, Pye J. A new 500 m^2 paraboloidal dish solar concentrator. Solar Energy. 2011;**85**(4):620-626. DOI: 10.1016/j.solener.2010.01.009

[10] El-Kassaby MM. New solar cooker of parabolic square dish: Design and simulation. Renewable Energy. 1991;**1**(1):59-65. DOI: 10.1016/0960-1481(91)90104-w

[11] Li Z, Tang D, Du J, Li T. Study on the radiation flux and temperature distributions of the concentrator receiver system in a solar dish/Stirling power facility. Applied Thermal Engineering. 2011;**31**(10):1780-1789. DOI: 10.1016/j.applthermaleng.2011.02.023

[12] Ma H, Jin G, Zhong X, Xu K, Li Y. Optical design of a solar dish concentrator based on triangular membrane facets. International Journal of Photoenergy. 2012;**2012**:1-5. DOI: 10.1155/2012/391921

[13] Hafez AZ, Soliman A, El-Metwally KA, Ismail IM. Design analysis factors and specifications of solar dish technologies for different systems and applications. Renewable and Sustainable Energy Reviews. 2017;**67**:1019-1036. DOI: 10.1016/j.rser.2016.09.077

Chapter

A Critical Study and Review on Abrasive Flow Micro Machining Process for Parameter Optimization and Process Implementation

Pragnesh D. Panchal and Sanket N. Bhavsar

Abstract

Modern times cannot be imagined without the use of hybrid-machining processes to achieve improvement in surface finishes. Abrasive flow machining (AFM) is one of these processes. It is a non-traditional machining technique that can be used for deburring and polishing to achieve surfaces such as complex geometries and edges by using a flow of pressurized abrasive laden viscoelastic polymer. It is very capable and appropriate for the finishing of complicated inner and outer surfaces and it has been experimentally confirmed that AFM can improve surface quality significantly. The proper combination of manufacturing circumstances is one of the most significant aspects to take into consideration in the popularity of industrialized processes. This paper highlights some of the existing methods of AFM and its effort to optimize them in order to improve the surface finish with few outlays.

Keywords: abrasives, AFM, surface finish, material removal rate

1. Introduction

Today's modern industry requires highly accurate and precise small-sized products. The majority of time taken and the most labor-demanding section of the process in today's manufacturing is the supreme finishing of intricate parts of a small size. Moreover, surface roughness of the final product has a significant role in various industries such as aerospace, automotive and biomedical, etc. A tiny burr or a cut will cause giant losses such as collapse of aerospace devices, energy loss in engines, breakage of components etc. In the earlier years, industries were using conventional super-finishing processes to acquire the necessary smoothness on the product. These traditional processes are not suitable for intricate geometries and complicated profiles to be machined to a higher level of finishing requirements. Advanced finishing processes have become more popular because the complicated inside geometrical features in various engineering materials can be finished with a desired accuracy. The aim of achieving nano level surface smoothness during machining is easily achieved by these advanced processes, which are demanded of today's industry.

Abrasive flow machining (AFM) was first described and patented by McCarty, the president of Extrude Hone Corporation in 1970 [1]. Because of its capability to machine interior and curved surfaces, it is considered as a suitable surface finishing process to finish internal complex geometry of work pieces. Presently AFM is well known as one of the greatest techniques for finishing of multifaceted geometries not easily reached by the traditional techniques. Investigators are always trying to achieve better results in the AFM process. The proper combination of manufacturing conditions is one of the chief aspects to improve the performance of newly developed processes and mainly in processes associated to AFM. This paper presents some of the literature available on the AFM process for process parameter optimization and to achieve a superior surface finish.

2. AFM process parameters and classifications

2.1 AFM process parameters

Rhoades [2–4] describe the fundamental theory of AFM process and recognized its process parameters. He reported that to facilitate the depth of cut first and foremost depends upon extrusion pressure, relative hardness, sharpness and also abrasive grain size. The controllable AFM process parameters are classified as in **Table 1** [5–9]. Perry showed that AFM can be used in engineering applications such as deburring, improving surface finish, contouring, elimination of recast layers generated due to thermal processing, etc. [10].

2.2 Classification of AFM machines

Abrasive flow machines are basically distributed into three categories: one way AFM, two way AFM, and orbital AFM. A short description of these types is provided below. In a one way AFM arrangement, the abrasive media enters forcefully into the work piece passage at an opening position and then exits on the other side, leaving a smooth internal passage to mark its passage [11]. For a more powerful polish, two way AFM arrangements might be employed. In a two way AFM arrangement, two hydraulic cylinders can control the abrasive media flow. These cylinders push and pull the media through the work piece [12]. It gives an extremely polished, smoother end result in less time compared to a one way AFM, which is shown in **Figure 1**. In the orbital AFM, orbital vibrations of a low amplitude are used to achieve the desired surface finish requirements (**Figure 2**) [13].

AFM process parameters		
Medium parameters	**Machine parameters**	**Work-piece parameters**
1. Abrasive type	1. Extrusion pressure	1. Initial surface
2. Abrasive size	2. Number of cycles	2. Material type
3. Abrasive concentration		3. Material hardness
4. Additives		4. Passage geometry
5. Polymer type and concentration		

Table 1.
Classification of AFM process parameters [5–9].

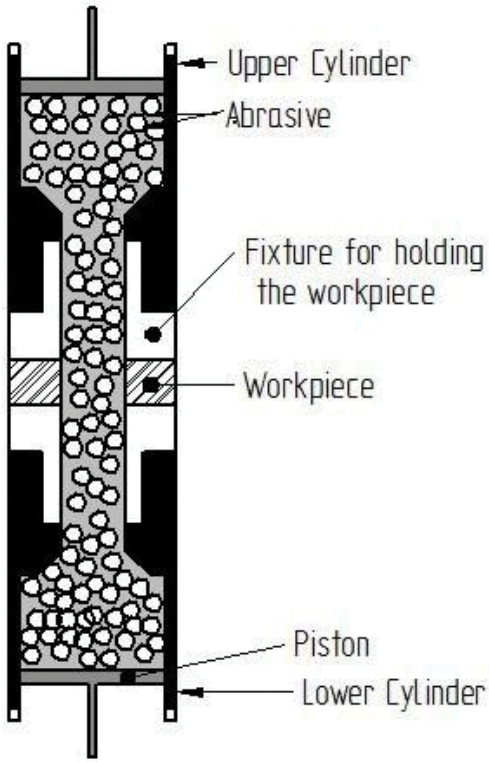

Figure 1.
Two-way AFM process.

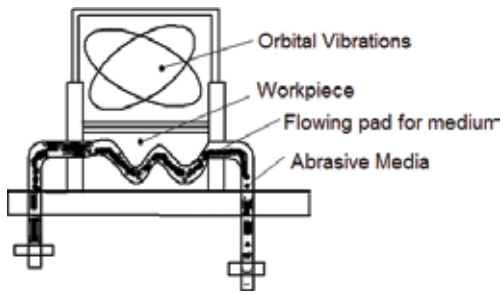

Figure 2.
Orbital AFM process.

AFM makes it feasible to polish and smooth the area that could not be easily reached by enabling the media to flow from beginning to end of the object internally. **Figure 3** shows the mechanism of material removal for different AFM processes. The following modes have been identified for metal deformation in abrasive machining process. First, elastic deformation related to abrasion; second, plastic deformation where a greater part of the object is displaced without being removed; and third, micro-cutting where material is eliminated in the form of chips of a micro size. The existence of any particular mode of deformation basically depends on the magnitude of cutting forces exerted on an individual grain, and the resistive force offered by work piece.

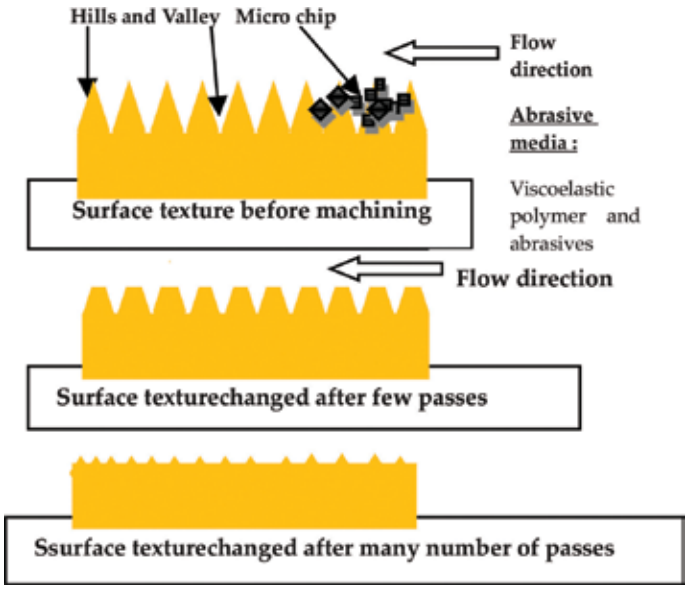

Figure 3.
Mechanism of material removal for AFM processes.

3. Experimental investigation explored in abrasive flow machining

Investigations by experimentation have been approved by a variety of investigators and reported that the total time to reach the essential finish is longer if the material deletion rate is low. To improve the performance of the AFM process, a variety of investigators have developed the mixed-mode machining processes in which different machining processes are used in conjunction with the AFM process to obtain a superior material removal rate (MRR) and obligatory surface finish in a smaller amount of time. Several of the latest developments in mixed-mode AFM processes are described here. Loveless [14] stated that dissimilar types of machining operations used to prepare the object before carrying out AFM is necessary and affects surface finish obtained throughout the process. The outcome shows that extrusion pressure did not have an essential effect while the type of machining method affected both metal removal and surface finish results. It also has been reflected that the viscosity of media significantly affected surface roughness. Authors [15] introduced a newly developed hybrid process called R-AFF. In this process, they rotated the work piece to increase the interaction between the work piece and the abrasive particles, which leads to improvements in the material removal rate and surface finish. The result shows that R-AFF can produce a 44% improvement in surface smoothness and an 81.8% improvement in MRR when compared to the AFF process. Researchers [16] inserted a drill bit in the experimental set-up to control the path of medium flow. This has been called the Drill Bit Guided Abrasive Flow Finishing (DBG-AFF) by researchers. The experiments were conducted on AISI 1040 and AISI 4340 materials. The arbitrary motion of abrasive particles generated by this arrangement helped to increase the interaction of fresh abrasive particles with work piece surface. Superior finishing rate and texture improvement have been reported in DBG-AFF when compared to AFM and R-AFF. **Figure 4** shows the DBG-AFF process. Authors [17] also tried to introduce the action of a centrifugal force on the abrasive laden viscous material. This experiment was carried out by inserting a rotating rod through the passage of the work piece. It was reported that the centrifugal force created by this rod is useful for the improvement in surface finish and material removal rate.

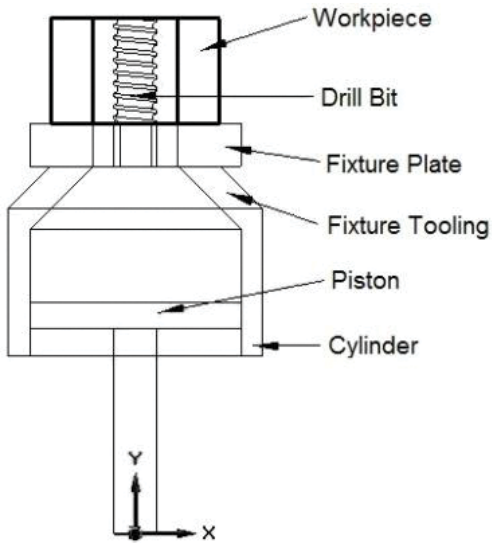

Figure 4.
Schematic diagram of DBG-AFF.

3.1 Modeling and optimization

It is essential to construct a mathematical model to understand the effect of various process parameters to achieve desired surface finish in a limited time period, that is, rate of material removal.

The neural network technique has been utilized for the purpose of developing a model of AFM process by researchers [18]. Five significant process parameters have been reported and are as follows. Parameters related to mechanical properties of the work piece, machining behavior, technical specification of set-up, process objectives, and viscosity of working media. This model primarily reduces the development time for new applications of the method and provides the data on effect of input variables on output parameters. Finite element model (FEM) has been used to forecast the stresses induced during AFM and forces exerted on the work piece surface [19]. Using this approach, they calculated the force exerted by each abrasive particle and depth of indentation produced on the work piece. Fletcher et al. [20] introduced a new relationship between media rheological properties and the AFM process. They investigated the shear rate of the polymer when it passes through the restricted area of the work piece. It was observed that the rate of shear increases in this case. They also concluded that better surface finish can be obtained by increasing the length of the piston stroke. Higher shear stress is generated on the wall and the coefficient of viscosity decreases because of the increase in piston stroke. The effect of the tangential force and related specific energy have also been investigated based on five process parameters such as hardness of the work piece, applied pressure, number of cycles, grain size, and number of active grains [21].

3.2 Developments in the abrasive medium

Abrasive medium is the most important and central ingredient of the AFM process. The abrasive medium is the viscoelastic polymers that act as mover media and abrasive particles that act as a wounding device to remove the rough material from the work piece. Numerous studies and investigations have been carried out in this area and they have tried to introduce a new substitute media for AFM process.

Some fresh advancement in the abrasive media by various researchers for AFM process is described in this part.

Wang et al. [22] developed an abrasive gel that has silicone rubber (P-silicone) and silicone rubber with additives (A-silicone). They concluded that silicone rubber (P-silicone) and silicone rubber with additives (A-silicone) are more suitable as media because they are easily available and also cost-effective. They also concluded that the surface finish is improved with A-silicone abrasive media with the number of cycles being less than five. Sankar et al. [23] used styrene-butadiene rubber (SBR) as the media and silicon carbide—SiC as the abrasives to study the effect during finishing on three types of work piece materials in AFM process. They proposed that surface roughness increases step-by-step as weight fraction of oil increase up to 10% and then starts falling. They also concluded that rheological properties of the media affect the material removal rate (MRR) and surface finish.

4. Various applications of AFM

Many industries and investigators applied AFM process on a variety of components for achieving greater surface finish. Some of the applications of the AFM process are as follows.

4.1 Machining of industrial and bio-medical components

Li et al. [24] used AFM equipment to achieve better surface roughness for a nonlinear tube runner in the military and civil field. Result shows that an AFM tool is important to achieve better surface integrity. Xu et al. [25] showed that AFM achieved better quality in helical gears. Wang et al. [26] improved the quality of the nozzle that is used in the diesel engine using the AFM process. Kumar et al. [27] introduced rotational-magnetorheological abrasive flow finishing (R-MRAFF) to achieve nano level surface roughness while finishing freeform components.

4.2 Machining of MEMS (micro-electro-mechanical systems)

Using the electron discharge machining process, we produced the micro channels but this process is prone to produce a recast layer in the area of machining. Focused ion beam (FIB) milling is also used to machine micro channels [28]. Microchannels are fundamental structure blocks of micro fluidic technology. Yan et al. [29] used a media to eliminate the recast layer from the micro channels formed by wire-EDM. They showed that the quality of the channels is improved with the use of the AFM process by removing recast layer and burrs. A miniaturized part such as fuel injector, micro filter, and ink-jet printer nozzle has a micro bore. These micro bores are finished with the help of AFM to offer better surface finish by removing internal unevenness.

5. Conclusion

The following concluding remarks are concluded from the above evaluation. AFM is a well-recognized superior finishing process. It uses abrasive laden medium that has the viscoelastic polymer and acts as a mover medium. Abrasive particles act as a cutting tool and remove the material from the work piece. AFM is normally

useful to finish multifaceted shapes for improved surface smoothness values. To overcome the drawback of low finishing rate, researchers have projected a mixture of AFM machines like as Orbital AFM, MRAFF, R-AFF, DBG-AFF etc. These processes have been effectively useful to finish works with complicated profiles generally used in bio medical, aerospace, automotive, die mold industries and the power sector. There is a need for more hybrid processes that improve the surface finish significantly. Abrasive flow machining is a possible candidate for further developments.

Author details

Pragnesh D. Panchal[1] and Sanket N. Bhavsar[2*]

1 Gujarat Technological University, Ahmedabad, Gujarat, India

2 Mechatronics Department, G H Patel College of Engineering and Technology, Vallabh Vidyanagar, Gujarat, India

Address all correspondence to: sanketbhavsar@gcet.ac.in

References

[1] McCarty RW. Method of Honing by Extruding. United States Patent US3521412 (A); 1970

[2] Rhoades LJ. Orbital and/or reciprocal machining with a viscous plastic medium. Patent number WO 90/05044, USA; 1990

[3] Rhoades LJ. Abrasive flow machining. Manufacturing Engineering. 1988;**2**:75-78

[4] Rhoades LJ. Abrasive flow machining: A case study. Journal of Material Processing Technology. 1991;**28**:107-116

[5] Sankar MR, Jain VK, Ramkumar J. Abrasive Flow Machining (AFM): An Overview. INDO-US WORKSHOP on Smart Machine Tools. Intelligent Machining Systems and Multi-Scale Manufacturing; 2008

[6] Hiremath SS, Vidyadhar HM, Singaperumal M. A novel approach for finishing internal complex features using developed abrasive flow finishing machine. International Journal of Recent advances in Mechanical Engineering (IJMECH). 2013;**2**(4):37

[7] Jain VK, Adsul SG. Experimental investigations into abrasive flow machining. International Journal of Machine Tools and Manufacture. 2000;**40**:1003-1021

[8] Santhosh Kumar S, Hiremath SS. A review on abrasive flow machining (AFM). Global colloquium in recent advancement and effectual researches in engineering, science and technology. (RAEREST 2016). Procedia Technology. 2016;**25**:1297-1304

[9] Baraiya R, Jain V, Gupta D. Abrasive flow machining: An area seeking for improvement. IOSR Journal of Mechanical and Civil Engineering. (IOSR-JMCE). Special Issue—AETM'16

[10] Perry WB. Abrasive liquid slurry for polishing and radiusing a microholes. Patent number 6,132,482, USA; 2000

[11] Rhoades LJ, Kohut TA, Nokovich NP. Unidirectional Abrasive Flow Machining. Patent number 5367833, USA; 29 November 1994

[12] Rhoades LJ, Kohut TA. Reversible Unidirectional AFM. Patent number 5,070,652, USA; 10 December 1991

[13] Gilmore JR, Rhoades LJ. Abrasive polishing Method, Apparatus and Composition. Patent Number 6,273,787, USA; 14 August 2001

[14] Loveless TR, Willams RE, Rajurkar KP. A study of the effects of abrasive flow finishing on various machined surfaces. Journal Material Processing Technology. 1994;**47**:133151

[15] Ravi Sankar M, Jain VK, Ramkumar J. Rotational abrasive flow finishing (RAFF) process and its effects on finished surface topography. International Journal of Machine Tools & Manufacture. 2000;**50**:637-650

[16] Sankar MR, Mondal S, Ramkumar J. Experimental investigations and modeling of drill bit guided abrasive flow finishing (DBGAFF) process. International Journal of Advanced Manufacturing Technology. 2009;**42**:678-688

[17] Walia RS, Shan HS, Kumar P. Abrasive flow machining with additional centrifugal force applied to the media. Machining Science and Technology. 2006;**10**(3):341-354

[18] Billo RE, Petri KL, Bidanda B. A neural network process model for abrasive flow machining operations. Journal of Manufacturing Systems. 1998;**17**(1):52-64

[19] Jain RK, Jain VK, Dixit PM. Modeling of material removal and surface roughness in abrasive flow machining process. International Journal of Machine Tool & Manufacture. 1999;**39**:1903-1923

[20] Fletcher AJ, Hull JB, Mackie J, Trengove SA. Computer modeling of the Abrasive Flow Machining process. Proceeding of International Conference on Surface Engineering; Toronto; 1990. pp. 592-601

[21] Jain RK, Jain V. Specific energy and temperature determination in abrasive flow machining process. International Journal of Machine Tools and Manufacture. 2001;**41**(12):1689-1704

[22] Wang AC, Weng SH. Developing the polymer abrasive gels in AFM process. Journal of Materials Processing Technology. 2007;**192-193**:486-490

[23] Sankar MR, Jain VK, Ramkumar J, Joshi YM. Rheological characterization of styrene-butadiene based medium and its finishing performance using rotational abrasive flow finishing process. International Journal of Machine Tools and Manufacture. 2011;**51**(12):947-957

[24] Li J, Yang L, Liu W, Zhang X, Sun F. Experimental research into technology of abrasive flow machining nonlinear tube runner. Advances in Mechanical Engineering. 2014;**6**:752353-752353

[25] Xu YC, Zhang KH, Lu S, Liu ZQ. Experimental investigations into abrasive flow machining of helical gear. Key Engineering Materials. 2013;**546**:65-69

[26] Wang WL, Jung D, Knafl A, Jacobs TJ, Hu SJ, Assanis DN. Experimental investigation of abrasive flow machining effects on injector nozzle geometries, engine performance, and emissions in a (DI) diesel engine. International Journal of Automotive Technology. 2008;**9**(1):9-15

[27] Kumar S, Jain VK, Sidpara A. Nano finishing of freeform surfaces (knee joint implant) by rotational-magneto rheological abrasive flow finishing (R-MRAFF) process. Precision Engineering. 2015;**42**:165-178

[28] Bhavsar SN, Aravindan S, Venkateswara Rao P. A critical review on microtools fabrication by focused ion beam technology (FIB) technolgy. In: Proceedings of the 2009 International conference of mechanical engineering (ICME'09), under world congress on engineering (WCE 2009); 1-3 July 2009; London, U.K. pp. 1510-1515

[29] Yan BH, Tzeng HJ, Hsu RT, Lin YC. Self-modulating abrasive medium and its application to abrasive flow machining for finishing micro channel surfaces. The International Journal of Advanced Manufacturing Technology. 2006;**32**(11-12):1163-1169

Chapter

Analyzing the Effect of Variable Process Parameters in Friction Stir Welding of Aluminum Alloys on Hardness

Vrajesh Patel, Nikul Patel and K. D. Bhatt

Abstract

Aluminum is one of the rare earth metals that has a high strength to weight ratio. Aluminum alloys are used for many different applications. Aluminum is a highly reactive metal with oxygen at the recrystallization temperature when applying conventional joining processes. The friction stir welding process was used in this research work to join AA 7075 T6 aluminum alloy plates. We used different process variable parameters such as tool pin geometry, tool rotation speed, and tool travel speed (welding speed). We also analyzed the effect of different process variable parameters on the hardness of the welded plates.

Keywords: friction stir welding, AA7075 T6, hardness, aluminum alloys, tool geometry

1. Introduction

Friction stir welding (FSW) is categorized as a solid state joining process. This process is performed below the recrystallizing temperature. It was invented by Wayne Thomas at TWI United Kingdom in 1991 [1]. FSW needs less energy input, is an environmentally friendly process, with repeat mechanical processes able to produce a very high strength welding process in a wide range of materials. This process is capable of producing high-quality and defect-free welds of 2xxx and 7xxx series aluminum alloys [2]. Different materials can be welded together with different aluminum alloys as there is no melting during the welding process [2]. The effect of different tool rotation speeds along with the different process parameters on AA 6063, T5, and T4 work pieces has been previously observed. The researcher observed that different tool rotation speeds did not result in significant differences in the hardness of welded plates by FSW, except for the width of the softened/partially melted area in the weld of AA 6063-T5 [3]. Regarding the mechanical properties of similar and dissimilar AA5182-H111 and AA6016-T4 metals, the researcher reported that both alloys showed a hardness deviation unswerving with the microstructure evolution across the thermo mechanical affected zone (TMAZ) [4, 5]. The overall mechanical properties depend on the ratio of the tool rotation speed to the welding speed [6, 7]. When the fracture location is at the body of the base metal or at the heat affected zone (HAZ) then the hardness value is high, but is lower hardness in comparison with the stirred zone.

The fracture location of the joints was in the HAZ of the AA6061 side due to a lower hardness value [8, 9]. The reason for the lower value could be the poor fusion of the two plates. This research work presents the effects of various process variable parameters on the hardness of welded aluminum plates by FSW.

2. Experiment

Aluminum alloy AA 7075 T6 was selected for experimental joints using FSW process. The experimental set up and typical welded plate is shown in **Figures 1** and **2**.

The plates are sized at 150 × 100 × 6 mm for butt joining. **Tables 1** and **2** show the chemical composition and mechanical properties of the plate material. The FSW is carried along the plate surface horizontally. The process parameters that are highly influential on FSW joints are tool rotating speed, tool travel speed, and tool pin profile. Three different pin profile tools are used to fabricate the joints that are made from the H13 tool steel. They are shown in **Figure 3**. The tool was held in the vertical arbor using a suitable collate. The edge of the plate was clamped on the bed with a zero root gap. The clamping of the plate was done to avoid vibration and translation force. After that, the rotating tool plunged in the butt joint until the shoulder touched the surface of the plate, then the tool ran at a pre-determined speed. The selected range of process parameters were divided into nine experiments based on previous research work. Nine experiments and their selected welding parameter are shown in **Table 3**.

Figure 1.
Experimental setup of FSW.

Figure 2.
Welded plate.

Metal	Al	Si	Fe	Cu	Mn	Mg	Cr	Ni	Zn	Ti	Pb
Percentage	89.7	0.05 Max	0.5	1.3	0.03 Max	2.69	0.2	0.01	5.78	0.06	0.01

Table 1.
Chemical composition of plate material (according to ASTM E 8).

Ultimate tensile strength (Mpa)	Yield strength (Mpa)	Tensile elongation (%)	Micro hardness (VHN)
572	503	11	175

Table 2.
Mechanical properties of plate material.

Figure 3.
FSW tools (a) straight cylindrical pin, (b) threaded straight cylindrical pin, (c) square pin.

Experiment no.	Tool rotational speed (rpm)	Traverse speed (mm/min)	Tool pin profile
1	1400	125	SCP
2	960	80	SCP
3	960	60	SCP
4	1400	85	SP
5	710	105	SP
6	1400	90	SP
7	1400	140	TSCP
8	900	90	TSCP
9	710	105	TSCP

Table 3.
Process parameter.

3. Result and discussion

Hardness is the property of the material that enables it to resist plastic deformation and penetration. As our material was nonferrous and an aluminum alloy, we measured the HRB of the material at different locations such as at the weld zone, at the HAZ, and at the parent material. The test was carried on the Rockwell hardness testing machine at ambient temperature. The hardness results are shown in **Table 4**.

As we can see in **Table 4**, the highest hardness at the weld zone was achieved when the tool rotation speed was high with tool traverse speed at 85 mm/min with the square pin profile. As the tool rotation speed decreases, the hardness with different tool pin profile also decreases. The hardness value at the HAZ is highest when

Experiment no.	Hardness at weld zone (HRB)	Hardness at HAZ (HRB)		Hardness of parent metal (HRB)
1	71	95	71	66
2	74	65	80	62
3	47	48	53	59
4	86	93	97	57
5	52	56	52	60
6	49	54	57	62
7	60	50	49	67
8	75	43	53	64
9	54	52	54	68

Table 4.
Hardness testing results.

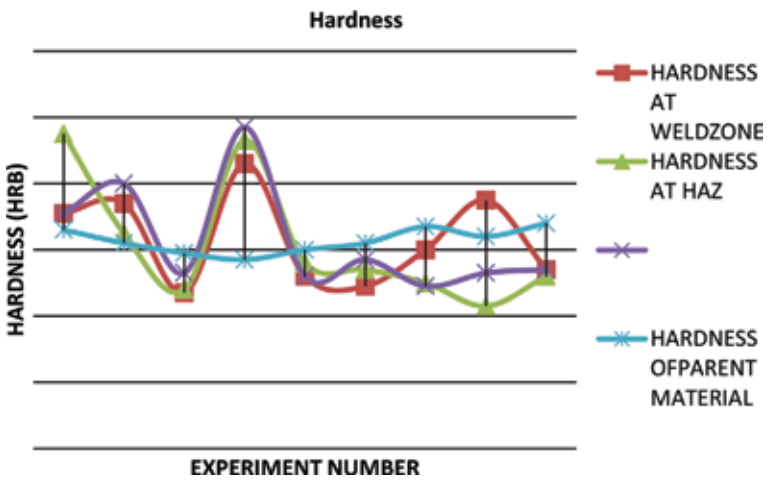

Figure 4.
Graph of experiment VS hardness.

the tool rotation speed was high with the straight cylindrical pin profile and it was achieved with a high traverse speed of tool during welding.

Figure 4 shows the hardness at different zones in the different experiments. As the value of the traverse speed decreases, the value of hardness at the heat affected zone also decreases and at a lower traverse speed, the hardness at the weld zone is also lowest. The highest hardness was obtained at the weld zone with the square pin profile and at the HAZ with the straight cylindrical pin profile. In the threaded straight cylindrical pin profile, the hardness was lower when compared to the other two pin profiles.

4. Conclusion

The hardness was measured at the weld zone, the heat affected zone, and the parent metal and from the results, we can say that using the SP profile with a higher tool rotation speed results in a high hardness at the weld zone and the heat affected zone. Welding with SCP at a lower tool traverse speed results in lower hardness at

the weld zone. Using threaded straight cylindrical pin (TSCP) at a higher tool rotating speed and welding speed (tool traveling speed) results in a hardness of the weld zone somewhat similar to the hardness of the parent metal.

Acknowledgements

We are very thankful to M/s. Ajay Engineering, V. U. Nagar and M/s. Kalika Industries, V. U. Nagar, for their support in helping us to complete this experiment. Special thanks to Er. Digvijay Varma for his help with this experiment.

Abbreviations

N (RPM)	tool rotary speed
WS (mm/sec)	welding speed
TSCP	threaded straight cylindrical pin
SCP	straight cylindrical pin
SP	square pin
HAZ	heat-affected zone

Author details

Vrajesh Patel[1], Nikul Patel[1] and K. D. Bhatt[2]

1 IIET, Dharmaj, India

2 BVM, V. V. NAGAR, India

References

[1] Thomas WM, Nicholas ED, Needham JC, Murch MG, Temple SP, Dawes CJ. Friction Stir Butt Welding. International Patent Application No PCT/GB92/02203. 1991

[2] Su JQ, Nelson TW, Mishra R, Mahoney M. Microstructural investigation of friction stir welded 7050-T651 aluminium. Acta Materialia. 2003;**51**(3):713-729

[3] Sato YS, Urata M, Kokawa H. Parameters controlling microstructure and hardness during friction-stir welding of precipitation-hardenable aluminum alloy 6063. Metallurgical and Materials Transactions A. 2002

[4] Leitao C, Leal RM, Rodrigues DM, Loureiro A, Vilaca P. Mechanical behaviour of similar and dissimilar AA5182-H111 and AA6016-T4 thin friction stir welds. Materials and Design. 2009;**30**:101-108

[5] Bayazid SM, Farhangi H, Ghahramani A. Effect of pin profile on defects of friction stir welded 7075 aluminum alloy. 2015;**11**

[6] Steven B. Dickson. An Investigation of Friction Stir Welding Parameter Effects on Post Weld Mechanical Properties in 7075AA; 2015

[7] Biswas P, Kumar DA, Mandal NR. Friction stir welding of aluminum alloy with varying tool geometry and process parameters. 2011;**226**

[8] Ravikumar S, Seshagiri Rao V, Pranesh RV. Effect of process parameters on mechanical properties of friction stir welded dissimilar materials between aa6061-t651 and aa7075-t651 alloys. 2014;**4**

[9] Panneerselvam K, Lenin K. Investigation on effect of tool forces and joint defects during FSW polypropylene plate. 2012;**38**

Chapter

Performance Evaluation of Deep Cryogenic Treatment on M2 HSS Tool Steel

Aaditya Patel, Yagnesh Mehta, Jay Chauhan, Yogesh Dabhi, Unnati Joshi and Sanjiv Rajput

Abstract

In the present work, we have attempted to develop a setup that aims at performing cryogenic treatment in a way that gradually reduces the temperature and avoids the thermal cracking of tools due to the large temperature gradient. For experimental purposes, deep cryogenic treatment (at 77 K) was performed on M2 High speed steel and machining studies were conducted on EN-9 material by means of both deep cryogenically treated and untreated tools. Micro-structural examination, hardness and tool wear were studied with the help of a metallurgical microscope, Rockwell hardness and toolmakers microscope respectively. The results reveal that fine carbide precipitation occurring at cryogenic temperature is responsible for enhancing the wear resistance property of the tools. Results also show that there was no noteable change in the hardness values of the tools.

Keywords: cryogenic treatment, liquid nitrogen, M2 HSS, carbide precipitation, tool wear

1. Introduction

In a world of advanced technologies, the requirement for materials to possess properties such as high wear resistance, superior strength, light weight and the ability to perform under extreme conditions is increasing. Thus, there is an indirect demand to develop tool materials with greater resistance and strength that are able to cut work piece materials with higher resistance. The necessity to increase the efficiency and effectiveness of production of a product resulted in emergence of new tool materials such as cermet, ceramics, cemented carbide and ultra-hard materials. In spite of the fact that High Speed Steel (HSS) was developed more than a 100 years ago, it is still widely used in modern day industries. Its major applications include taps, drill bits, broaches, single point cutting tools and also in place of carbide tools with fairly low economical cutting speeds [1, 2].

The property of the material mainly depends on the chemical composition and microstructure. So to alter the properties of a material either the chemical composition or microstructure must change. Heat treatment is the process that is utilised to change the microstructure of the material [1–3]. The regular heat treatment process for tool steels includes heating the raw material up to the austenitizing temperature and then carrying out suitable quenching methodology to achieve the required

hardness. In the quenching process, the Austenite (soft phase) present in the steel is converted to Martensite, which is considered the hardest phase when compared to other phases. One of the key aspects of this process is the formation of Martensite, which starts and finishes at a particular temperature. In regular heat treatment, the lowest temperature achieved after quenching is room temperature (30°C) but the Martensite finish temperature for tool steel is around −50°C and hence there is always retained Austenite present in the material [3–5].

It is a widely established fact that a long exposure time of a material to very low temperature triggers some definite changes. This caused the tool manufacturers to start exploring the true potential of "Cold Treatment", that is a process in which a material is exposed to a temperature lower than the surroundings.

1.1 Cryogenic treatment

Cryogenic treatment is an auxiliary process to the regular heat treatment process. After performing the regular heat treatment process on the steel, it's time for it to undergo cryogenic treatment. The first step of the cryogenic treatment process is to gradually cool down the steel that is at room temperature to a temperature of 77 K (boiling point of liquid nitrogen) at a particular cooling rate. Gradual cooling of the material is done because if it is directly exposed to liquid nitrogen than the material will experience thermal shock and it will make the steel brittle. After achieving the temperature of 77 K, the steel is kept at that temperature for a certain period of time so that the changes that are occurring during the process are throughout the material and uniform properties are obtained by doing so. The next step is to bring the material back to room temperature at a specific heating rate. After this heating process, the material is passed through tempering cycles to regain the lost ductility and to relieve stresses.

2. Experiment

The experiment was preceeded by designing and manufacturing the setup suitable for performing cryogenic treatment. The setup was designed taking into consideration the thermal and mechanical aspects during its functioning. **Figure 1** shows the actual view of the setup.

Figure 1.
Arrangement of the cryogenic treatment setup.

2.1 Working of the setup

The flow of liquid nitrogen takes place from the Dewar to the copper coils in the setup with the help of an extraction pump. Before pumping liquid nitrogen into the setup, a vacuum i created in the annular space provided in the setup to reduce heat transfer by conduction and convection. The tool is kept in a beaker that is surrounded by copper coils. As liquid nitrogen flows through the copper coils, it gradually reduces the tool's temperature to a desired temperature. A thermocol box is provided at the exit of the copper coil for storing the liquid nitrogen. After attaining a stable temperature, a liquid nitrogen bath is provided for soaking the tool for a duration of 24 hours. A tempering process is carried out to regain the lost ductility and increase the toughness in the tool. The temperature of the tool is measured with the help of RTD, which is connected to the data logger. The data logger takes the temperature reading every 10 seconds.

After completion of the cryogenic treatment cycle, the tool undergoes various tests that help in validating the benefits of cryogenic treatment. These tests include checking for wear on the tool after a given time, hardness and microstructure examination.

For experimentation purposes, M2 HSS Tool Steel was used. It is one the most widely used tool materials in simple turning operation. The physical characterisation of the tool was measured with the help of a spectrometer, toolmakers microscope, Rockwell hardness tester, and metallurgical microscope.

3. Results and discussion

3.1 Chemical composition

The Spark Spectrometer was used to measure the composition of the specimen and also to verify its contents with ASME standards (**Table 1**).

ID	%C	%Mn	%Si	%S	%P	%Cr	%Ni	%Mo	%V	%Co	%W
Test Piece	0.712	0.339	0.497	0.014	0.108	3.92	0.64	4.146	1.650	0.370	6.35

Table 1.
Chemical composition of M2 HSS tool.

3.2 Microstructure examination

The microstructure examination was performed using standard half inch M2 HSS tool steel. The first step in this process is specimen preparation, which includes polishing the specimen with emery paper and then etching it in a solution of 3% Nital. A metallurgical microscope was used to analyse the microstructure of both the cryogenically treated and untreated specimen. **Figures 2** and **3**, represent the microstructure of both specimens taken at 200X magnification.

Fine carbide precipitation (black spots) was observed widely in **Figure 2** compared to **Figure 3**, which is a direct correlation to the improvement in dimensional stability as well as wear resistance of the tool [6, 7].

Figure 2.
Microstructure of cryogenically treated tool.

Figure 3.
Untreated tool.

3.3 Tool wear and tool life measurement

The measurement of tool wear of both the specimens was carried out using identical working conditions during turning operations on a lathe machine (**Table 2**).

The following parameters for speed, feed and depth of cut were maintained for both the untreated and cryogenically treated tools. Before the experiment, the length of wear lend was measured with the help of a toolmakers microscope (**Table 3**).

Normal rake angle (°)	Normal clearance angle (°)	Side cutting edge angle (°)
5	3	30

Table 2.
Tool geometry for experimentation purpose.

Machining parameters	Value
Work piece material and diameter	EN 9, Ø80 mm
Spindle speed	190 rpm
Depth of cut	2.5 mm
Feed	0.125 mm/rev
Machining time	500 sec

Table 3.
Machining parameters set on the lathe machine during turning operation.

After 500 seconds of machining, tool wear lend was measured with the help of toolmakers microscope (**Figure 4**).

The tool wear experiment revealed performance improvements in the cryogenically treated tool when compared to the one not treated. The cryogenically treated tool showed less wear during the course of the experiment, nearly 150 μm less than its counterpart (**Table 4**) (**Figure 5**).

The tool life experiment was carried out by keeping the same machining parameters constant for both the tools (**Table 5**).

The percentage increase in tool life after cryogenic treatment can be calculated by:

Percentage increase in tool life = $(T1-T2)/T2$ = 48.07%.

Figure 4.
Wear measurement of the specimens using a toolmakers microscope.

Time (min.)	Tool wear (μm)	
	Cryogenically treated tool	Untreated tool
0	0	0
10	120	130
30	290	410
55	490	610
70	670	820

Table 4.
Wear measurement after specific intervals of time.

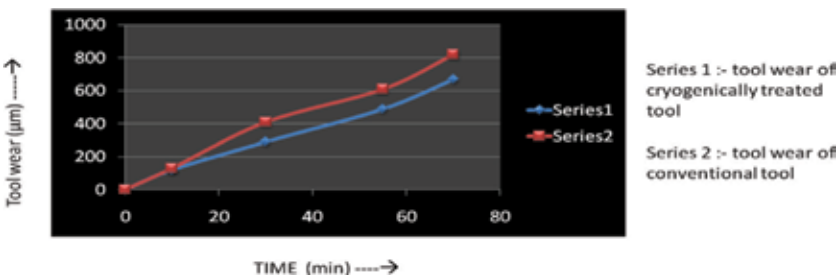

Figure 5.
Performance analysis of cryogenically treated tool and untreated tool.

Tools	Tool life (min)
Cryogenic treated tool	77 min (T1)
Conventional tool	52 min (T2)

Table 5.
Tool life values for both the tools.

3.4 Hardness measurement

The hardness of the specimens was measured using the Rockwell hardness tester.

Values in **Table 6** reveal that there is no change in hardness values of the tools [7].

Sr. No.	Tool	Hardness values (HRC)	Average hardness (HRC)
1.	Cryogenically treated tool	65, 66, 64	65
2.	Untreated tool	64, 66, 65	65

Table 6.
Hardness values in HRC.

4. Conclusions

1. The performance of the cryogenically treated tool was found to be superior when compared to the untreated tool. The dimension stability of the tool improved as a result of fine carbide precipitation occuring due to long hours of soaking at the cryogenic temperature. This is evident from the microstructure examination as well as from the subsequent tool wear experiment which shows nearly 150 μm less tool wear taking place on the cryogenically treated sample.

2. The tool life of the cryogenically treated tool increased by nearly 48.07%.

3. There was no change in the hardness values of the tools, which shows that cryogenic treatment does not influence the hardness values of the sample and has only impacted on the microstructure of the specimen.

Author details

Aaditya Patel*, Yagnesh Mehta, Jay Chauhan, Yogesh Dabhi, Unnati Joshi and Sanjiv Rajput
Department of Mechanical Engineering, A. D. Patel Institute of Technology, Gujarat, India

*Address all correspondence to: adityapatel17@gmail.com

References

[1] da Silva F'v J, Emmanuel O, Antonio E, Souza M Jr. Performance of cryogenically treated HSS tools. Wear. 2006;**261**:674-685. DOI: 10.1016/j.wear.2006.01.017

[2] Podgornika B. Deep cryogenic treatment of tool steels. Journal of Materials Processing Technology. 2016;**229**:398-406. DOI: 10.1016/j.jmatprotec.2015.09.045

[3] Molinari A, Pellizzari M. Effect of deep cryogenic treatment on mechanical properties of tool steels. Journal of Materials Processing Technology. 2001;**118**:350-355. DOI: 10.1016/S0924-0136(01)00973-6

[4] Tyshchenko AI et al. Low-temperature martensitic transformation and deep cryogenic treatment of a tool steel. Materials Science and Engineering: A. 2010;**527**(26):7027-7039. DOI: 10.1016/j.msea.2010.07.056

[5] Zhirafar S, Rezaeian A, Pugh M. Effect of cryogenic treatment on the mechanical properties of 4340 steel. Journal of Materials Processing Technology. 2007;**186**(1):298-303. DOI: 10.1016/j.jmatprotec.2006.12.046

[6] Huang JY, Zhu YT, Liao XZ. Microstructure of cryogenic treated M2 tool steel. Materials Science and Engineering A. 2003;**339**:241-244. DOI: 10.1016/S0921-5093(02)00165-X

[7] Zare A, Mansouri H, Hosseini SR. Effect of deep cryogenic treatment on the microstructure and mechanical properties of HY-TUF steel. Metallography, Microstructure, and Analysis. 2015;**4**:169-177. DOI: 10.1007/s13632-015-0206-4

Chapter

Effect on Cutting Force during Hard Machining of AISI D2 Tool Steel Using AlCrN Coated Tool

Ravikumar Dasharathlal Patel and Sanket N. Bhavsar

Abstract

At present, milling is the most suitable process among other all process for making molds, dies, automotive parts and aerospace parts, which are manufactured from hard tool steel. Tool steel (D-Grade tool steel) materials are largely used in the manufacture of cold forming dies due to the excellent wear characteristics and deep hardening. AISI D2 tool steel is used as the work material for the current experiment. Many researchers demonstrated that AlCrN coating, which has been developed recently, provided better wear protection than TiAlN coating. The present paper provides the details of machining experiments of AISI D2 tool steel using an AlCrN coated end mill tool. The aim of the present study is to develop a relationship between cutting force and input parameters (cutting speed, feed, depth of cut and width of cut). First and second order models were developed using Response Surface Methodology (RSM). The predicted cutting force results are shown in terms of first and second order equations. Comparision of both models (1st and 2nd order) for the prediction of cutting force during machining of AISI D2 tool steel was performed during this research work.

Keywords: milling, hard machining, AISI D2 steel, AlCrN coated tool, RSM CCD, ANOVA

1. Introduction

In the global market, satisfaction of customer requirements without compromising quality is becoming a major issue to sustain in the competitive market. One of the most widely used manufacturing processes is the milling process, which is interrupted cutting process to remove chips to obtain the required shape [1]. In manufacturing industries, the milling process is widely used to manufacture dies, automobile parts and aerospace industries. The cutting circumstances are more adverse than in turning [2]. The milling process for hard materials has reduced lead time and machining costs compared to other traditional processes [3]. In die and mold-making industries, machining of hard material is a challenging task due to high tool wear, higher tooling and handling cost [4]. Gaitonde et al., undertook an experiment on AISI D2 tool steel to evaluate machinability with analysis of cutting temperature, tool wear and surface roughness [5]. For hard machining, tool wear and temperature at the tool tip were the major issues [6]. To overcome this, coating on the tool can effectively improve the tool life. Coating of a cutting tool enhances the wear resistance, oxidation resistance, reduces temperature variation in tool and improves lubricity of the tool [7]. Experiments were carried out on austenitic

stainless steel using hard AlTiN, AlCrN PVD coated tool. The AlCrN-based coatings have superior oxidation resistance and hot hardness when compared to AlTiN ones [8]. Hard machining in dry conditions gave the best results and substantial advantages such as lower manufacturing costs, reduced time for finish machining and improved surface quality [9]. Some research work has proved that there is high tool flank wear in up-milling operations compared to down-milling operations [1]. Tongchao Ding et al. milled AISI H13 steel with optimal cutting parameters and analyzed the significant effect on cutting force and surface roughness [10]. Experimental investigations were carried out by end milling process on hardened Impax Hi hard tool steel (55 HRC) by Bala Murugan Gopalsamy et al. [11]. Experimental and theoretical study has been undertaken on heat flow when machining of AISI H13 and AISI D2 tool steel by using ball nose end mills (TiAlN and tipped with PCBN) [12]. Flank wear is the main type of tool wear. Chipping, adhesion and attrition were responsible for flank wear. Due to this, tool life is less than 40 m length of cut when end milling of AISI D2 tool steel (58 HRC) [13]. End milling of AISI D2 tool steel is analyzed to develop the tool life model using PVD TiAIN coated carbide end mill tool. Lajis et al. developed a mathematical model that indicates the relationship between tool life and machining variables by using the concept of RSM [4]. Researchers also developed a mathematical model to predict cutting forces during machining of complex surfaces [14].

No much work has been done on AISI D2 tool steel with AlCrN coated end mill tool. At present, hardened AISI D2 tool steel is mostly machined by AlCrN coated carbide. The aim of this paper is to develop the relationship between the output response (cutting force) and input parameters (cutting speed, feed, depth of cut and width of cut) when AISI D2 tool steel is machined by an AlCrN coated tool.

2. Experimental details

As part of the current research work, AISI D2 tool steel with a hardness of 62 HRC was hard machined. The chemical composition of the cut material can be found in **Table 1**.

The hardness of 59 HRC of the testing samples was achieved by hardening (with oil quenching) at 970°C followed by 2 hours of tempering at 710°C.

Machining was done on 40 × 80 × 16 mm AISI D2 tool steel (59HRC). Cutting experiments were carried out by Jyoti CNC machining Centre PX10. Walter made AlCrN coated tool (MC232-10.0W4B-WJ30ED) with a 10 mm diameter and four flute flat end mills were used for experimental work (shown in **Figure 1**). A tool dynamometer (9272, Kistler made) was mounted on the table of the machine tool to measure the cutting force signals during machining as shown in **Figure 2**. The signals were amplified through a charge amplifier and analog signals were converted using A/D acquisition card (PCI-6-23E, NI) and stored in a computer. LabVIEW was employed for cutting force data acquisition.

For the performance of experiments with four factors at five levels, RSM CCD design of experiment was employed to conduct the milling experiments. The RSM is helpful for analyzing, developing, improving and optimizing a process [15].

C	Si	Mn	Cr	Mo	V	W
1.560	0.280	0.340	11.700	0.560	0.210	0.460

Table 1.
Chemical composition (average %) of machined AISI D2 tool steel.

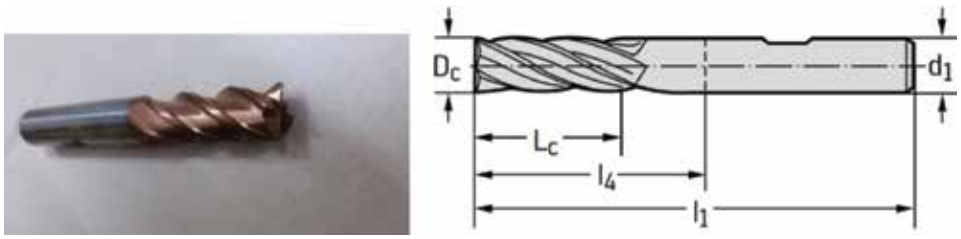

Figure 1.
AlCrN coated tool.

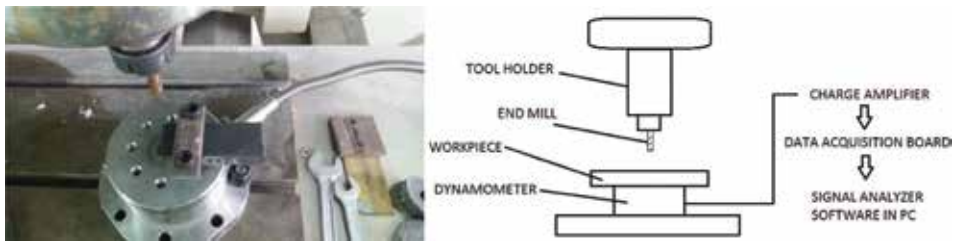

Figure 2.
Experimental setup.

Input variables	Lowest	Low	Centre	High	Highest
	$-\sqrt{2}$	−1	0	+1	$+\sqrt{2}$
Cutting speed (Vc)	50	87.5	125	162.5	200
Feed (mm/min)	50	237.5	425	612.5	800
Depth of cut (mm)	0.1	0.325	0.55	0.775	1
Width of cut (mm)	2	4	6	8	10

Table 2.
Independent variable with levels.

RSM CCD was chosen because of the minimum number of experimental trials required as well as it is more efficient in handling a large number of factor variables compared to traditional factorial design. As shown in **Table 2**, the four factors to be considered were cutting speed, feed, radial depth of cut, and axial depth of cut.

3. Experimental results and discussion

For experiment work, experiments were performed for cutting speeds (Vc) from 50 to 200 m/min, feed (fz) at 50–800 mm/min, axial depth of cut (ap) from 0.1 to 1 mm and width of cut (ae) from 2 to 10 mm for PVD coated AlCrN coated end mill tool to achieve relationship between four input parameters (cutting speed, feed, depth of cut and width of cut) with cutting force.

A Central Composite Design (CCD) is the best design to fit for four factor and five level design. It is a very efficient design for fitting the second order model [16]. Design expert 6 was used to analyze the mathematical models for both the first order model and second order model. The overall cutting conditions with CCD are presented in **Table 3**. The normal force, feed force and axial force were recorded during each experiment and are given in **Table 3**.

Run order	C.S. (m/min)	FEED (mm/min)	DOC (mm)	WOC (mm)	Normal force Fx (N)	Feed force Fy (N)	Axial force Fz (N)
1	125	425	1	6	21.784	21.972	678.493
2	87.5	612.5	0.775	4	21.784	21.972	892.151
3	162.5	612.5	0.325	8	21.784	21.972	419.052
4	162.5	612.5	0.325	4	6.519	21.972	525.881
5	87.5	612.5	0.325	4	21.784	21.972	632.709
6	87.5	237.5	0.775	8	21.784	21.972	876.890
7	125	425	0.55	6	37.152	21.900	557.006
8	87.5	612.5	0.775	8	6.519	37.231	1456.818
9	125	50	0.55	6	21.784	21.972	449.574
10	125	425	0.55	6	36.998	22.102	555.993
11	50	425	0.55	6	21.784	37.231	983.719
12	125	425	0.55	6	37.112	21.889	556.216
13	162.5	237.5	0.775	4	21.784	37.231	327.484
14	125	425	0.55	6	37.099	21.823	556.901
15	87.5	612.5	0.325	8	21.784	21.972	1151.593
16	125	425	0.55	10	37.048	21.972	876.890
17	87.5	237.5	0.775	4	21.784	37.231	586.926
18	162.5	237.5	0.325	4	21.784	21.972	434.313
19	162.5	237.5	0.325	8	21.784	21.972	510.619
20	125	425	0.55	6	37.048	21.972	556.403
21	125	425	0.55	2	21.784	21.972	495.358
22	162.5	612.5	0.775	8	37.048	37.231	785.322
23	87.5	237.5	0.325	8	21.784	21.972	937.935
24	162.5	237.5	0.775	8	21.784	21.972	632.709
25	125	425	0.1	6	21.784	21.972	266.439
26	200	425	0.55	6	21.784	52.490	571.664
27	125	425	0.55	6	37.111	22.001	555.982
28	87.5	237.5	0.325	4	37.048	21.972	541.142
29	125	800	0.55	6	21.784	21.972	693.755
30	162.5	612.5	0.775	4	21.784	21.972	495.358

Table 3.
Design cutting condition with CCD and experimental results.

By using the experimental investigation, cutting force values were obtained in set experimental conditions. The following Linear model and Quadratic model of cutting force prediction has been developed, followed by ANOVA analogy.

The F-value obtained with linear model is 14.68, which implies that the model is significant.

Final Equation in Terms of Actual Factors:

$$Fz = 423.87335 - 4.18837^{*}CS + 0.44427^{*}FEED + 319.35593^{*}DOC + 64.54246^{*}WOC \quad (1)$$

The F-value obtained with quadratic model is 18.87, which implies that the model is significant.

Final Equation in Terms of Actual Factors:

$$Fz = +617.35850 - 6.72213^{*}CS + 0.67715^{*}FEED - 247.57141^{*}DOC + 58.86704^{*}WOC - 7.73236E-003^{*}CS^{*}FEED - 1.00470^{*}CS^{*}WOC + 1.33395^{*}FEED^{*}DOC + 0.047393^{*}CS^{2} + 10.93859^{*}WOC^{2} \quad (2)$$

First and second order CCD models were represented by Both Eqs. (1) and (2) respectively, Results have indicated that cutting speed would give significant effect on cutting force values followed by feed and depth of cut.

From the above results, it is indicated that the error of linear model is much more compared to the error of quadratic model. The average error of the linear model was 0.06 derived by the equation and average error of linear model was 0.02 derived by the equation. From that comparison, it is clear that the quadratic model is more reliable to predict the cutting force model with CCD design. Also it is revealed that the Central Composite Design (CCD design) is a very efficient design for fitting the second order model [13].

By using Eqs. (1) and (2), theoretical values are calculated and compared with practical value from **Table 3**. From that comparison, the average errors for linear and quadratic models are calculated using following equation;

Average Error (ε) for Linear model.

Avg ε (linear) = Σ sum of linear errors/Σ Total number of trial (T) = 0.06.

Average Error (ε) for Quadratic model.

Avg ε (quad) = Σ sum of quadratic errors/Σ Total number of trial (T) = 0.02.

From the above result, the percentage average error between measured and predicted cutting force of both models is less than 10% as well as the average percentage error for quadratic model being less than 5%.

4. Conclusion

This research work has been carried out to develop a mathematical model to predict cutting forces in end milling of AISI D2 tool steel by using the experimental results obtained through the concept of RSM. From the result, the first order (linear) model as well as the second order (quadratic) mathematic model have been developed. Validity or adequacy of the models has been evaluated by ANOVA, which indicates that the models are reliable. These models are valid within the ranges of the cutting parameters in end milling which for cutting speeds (Vc) was from 50 to 200 m/min, feed (fz) was from 50 to 800 mm/min, axial depth of cut (ap) from 0.1 to 1 mm and width of cut (ae) from 2 to 10 mm. Both models (linear and CCD quadratic) have shown similar trends. The percentage average of error between the measured and predicted cutting force of both models is less than 10% but we found that the average percentage error is less than 5% for the quadratic model.

Author details

Ravikumar Dasharathlal Patel[1] and Sanket N. Bhavsar[2]

1 GTU, Gujarat, India

2 G H Patel College of Engineering and Technology, Gujarat, India

References

[1] Chen XQ, Li HZ, Zeng H. An experimental study of tool wear and cutting force variation in the end milling of Inconel 718 with coated carbide inserts. Journal of Materials Processing Technology. 2006;**180**:296-304

[2] Chahal M, Singh V, Garg R. Optimum surface roughness evaluation of dies steel H-11 with CNC milling using RSM with desirability function. International Journal of Systems Assurance Engineering and Management. June 2017;**8**(2):432-444

[3] Gopalsamy BM, Mondal B. Experimental investigations while hard machining of DIEVAR tool steel (50 HRC). The International Journal of Advanced Manufacturing Technology. 2010;**51**:853-869

[4] Lajis MA, Karim ANM, Amin AKMN, Hafiz AMK, Turnad LG. Prediction of tool life in end milling of hardened steel AISI D2. European Journal of Scientific Research. 2008;**21**(4):592-602

[5] Gaitonde VN, Karnik SR, Maciel CHA, Rubio JCC, Abrão AM. Machinability evaluation in hard milling of AISI D2 steel. Materials Research. 2016;**19**(2):360-369

[6] Valera H, Bhavsar SN. Experimental investigation of surface roughness and power consumption in turning operation of EN 31 alloy steel. Procedia Technology. 2014;**14**:528-534. DOI: 10.1016/j.protcy.2014.08.067

[7] Liew WYH. Low-speed milling of stainless steel with TiAlN single-layer and TiAlN/AlCrN nano-multilayer coated carbide tools under different lubrication conditions. Wear. 2010;**269**(7-8):617-631

[8] Endrino JL, Fox-rabinovich GS, Gey C. Hard AlTiN, AlCrN PVD coatings for machining of austenitic stainless steel. Surface and Coating Technology. 2006;**200**:6840-6845

[9] Tang L, Huang J, Xie L. Finite element modeling and simulation in dry hard orthogonal cutting AISI D2 tool steel with CBN cutting tool. The International Journal of Advanced Manufacturing Technology. 2011;**53**:1167-1181

[10] Tongchao Ding YW, Zhang S, Zhu Ding X. Empirical models and optimal cutting parameters for cutting forces and surface roughness in hard milling of AISI H13 steel. International Journal of Advanced Manufacturing Technology. 2010;**51**:45-55

[11] Gopalsamy BM, Mondal B, Arntz K, Klocke F, Ghosh S. Investigations on hard machining of Impax Hi hard tool steel investigations on hard machining of Impax Hi hard tool steel. International Journal of Material Forming. 2009;**2**:145-165

[12] Lincoln Cardoso Brandao ARR, Coelho RT. Experimental and theoretical study of workpiece temperature when end milling hardened steels using (TiAl)N-coated and PcBN-tipped tools. Journal of Materials Processing Technology. 2008;**199**:234-244

[13] Koshy P, Dewes RC, Aspinwall DK. High speed end milling of hardened AISI D2 tool steel (58 HRC). Journal of Materials Processing Technology. 2002;**127**:266-273

[14] Gosai M, Bhavsar SN. Experimental study on temperature measurement in turning operation of hardened steel (EN36). Procedia Technology. 2016;**23**:311-318. ICIAME 2016. https://doi.org/10.1016/j.protcy.2016.03.032

[15] Mountgomery D. Design and Analysis of Experiments. SAS Institute Inc; 2013

[16] Bhavsar SN. An approach for selection of variable feed rate for quality machining of sculptured surfaces. Journal-Institution of Engineers India Part PE Production Engineering Division. 2007;**87**(Pt 2):36-41

Chapter

A Review on Development and Fabrication Methodology for Vacuum Vessel from Aluminum Alloy

Rushit Mistry and Kaushal Bhavsar

Abstract

A vacuum vessel is an inflexible walled element inside which air and gases are evacuated, the outcome is a low-weight district vessel that is alluded to as a vacuum. A vacuum vessel is used in many applications, among one is in the space field for placing and carrying loads into space. The focus of this paper is to study and analyze the vacuum vessel, its development material and fabrication method by which vacuums that are sound, defect-free, leak-proof with a uniform strength are produced. After studying various research analyses and undergoing a literature review, Friction Stir Welding (FSW) has been proven to be a successful joining procedure for high strength aluminum alloys. This procedure has large benefits related to fusion and arc welding processes for joining aluminum alloy. This vacuum vessel work has been compiled for space application.

Keywords: aluminum alloy, vacuum vessel, fabrication methodology, friction stir welding, space application

1. Introduction

1.1 Significance of vacuum and vacuum vessel

The word "vacuum" comes from the Latin word "vacuus" which means empty or void of stuff. The vacuum categories include natural vacuum and artificial vacuum. Space is a region with supreme zero pressure from a natural vacuum. A perfect or entire vacuum, which suggests an area that is entirely void of matter, is unachievable on earth, but it is possible to generate and hold the lower pressure region referred to as an artificial vacuum by means of a vacuum vessel and vacuum generation pump. The objective of artificial vacuum generation techniques is to simulate the vacuum pressure environment. A vacuum in space can have a pressure less than 760 Torr.

A vacuum vessel is a compact, rigid, closed chamber in which air and other gas molecules have been evacuated by a vacuum pump. A vacuum vessel isolates the partial vacuum region from the outside atmosphere. The lowest pressures inside the vessel is reached by using modern vacuum pumping strategies where large amounts of molecules are evacuated. The core of the vacuum framework is the

vacuum chamber, which is customized to each application. It encloses the application and reliably splits it from the outside or protects the surrounding from the processes inside. A vacuum vessel has numerous isolating ports that are covered with the flanges and this enables instruments or windows to be introduced in the dividers of the vessels.

1.2 Vacuum vessel classification

a. Based on manufacturing methods

   1. Welded vacuum vessels

   2. Forged vacuum vessels

   3. Formed (extrude) vacuum vessels

   4. Blow mold vacuum vessels

b. Based on geometric configuration

   1. Plate to plate (square) vacuum vessels

   2. Cylindrical vacuum vessels

   3. Spherical vacuum vessels

   4. Monocopue vacuum chambers

c. Based on type of vacuum

   1. Low vacuum vessels (25–760 Torr)

   2. Medium vacuum vessels (10^{-3}–760 Torr)

   3. High vacuum vessels (10^{-9}–10^{-3} Torr)

   4. Ultra-high vacuum vessels (10^{-12}–10^{-9} Torr)

2. Findings of literature review

2.1 Vacuum vessel configuration with developing method

The vacuum vessel has been developed for different applications according to the need of the achieved required vacuum range. For different material, many different methods are used for manufacture according to the type of base material used for the vacuum vessel. To develop a vacuum vessel, the following procedures have been used: arc welding methods like GTAW-Gas Tungsten Arc Welding, GMAW-Gas Metal Arc Welding, SAW -Submerge Arc Welding, MIEA-Modified Indirect Electric Arc welding and other non-convectional welding procedures such as Nd-YAG laser beam welding, FSW-Friction Stir Welding and Electron Beam welding.

2.1.1 FSW-friction stir welding fabrication to develop vacuum vessel

The friction stir welding process is shown in **Figure 1** and is an autogenous joining technique in the solid state and it uses an in-between non-consumable revolving tool with an appropriate geometry profiled shoulder and probe pin that is produced from a harder material than the workpiece material. The rotating tool is plunged into the weld joint and compelled to navigate the joint line, heating the adjoining segments by interfacial and internal friction between the tool and base material, thus producing a weld joint through extruding, forging and stirring the materials of the workpiece.

The benefits of FSW include the ability to join aluminum alloy materials, which are difficult to fusion weld, for example, 2XXX and 7XXX series aluminum alloys. Other benefits of the FSW process are that it is easy to weld any configuration even a long weld, there is low distortion with fine microscopic structure, excellent mechanical properties proven by fatigue, shear and tensile tests, no shielding gases and consumable fill up welding rods required [1].

Dalder et al. [2] constructed a thick wall AA2219 material pressure vessel using a Bobbin tool friction stir welding (BTFSW). The whole research project was divided into two sections. The first section of research was focused on the development of the essential process to make defect-free circumferential weld joints between two 102 cm internal diameter hemispheres made from aluminum alloy AA2219 by means of BTFSW. The second section of the project involved signifying that the developed weld joint was essentially adequate for the intended service period. This literature work revealed that the spherical configuration vacuum vessel of aluminum alloy AA2219 was successfully welded by the bobbin friction stir welding. From closing out the circumferential weld, a keyhole is present due to bobbin tool retraction. Friction plug welding was used to close the hole with the same material as the pressure vessel.

2.1.2 Fusion welding-TIG (tungsten inert gas) welding

Jadeja et al. [3] has been working on Limiter-based ADITYA tokamak, which was developed into the diverter designed ADITYA-U tokamak. The main feature of the ADITYA tokamak was that the rectangular cross-section of the vessel was

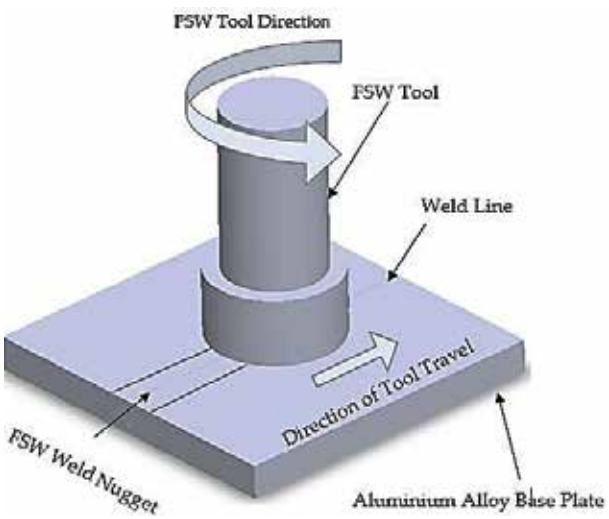

Figure 1.
Principle of friction stir welding.

replaced by a circular cross-section to accommodate additional poloidal coils in the space between the wall of the vessel and toroidal field coil. The upgraded stainless steel SS304 L vacuum vessel has a spherical configuration developed by the manual operated TIG welding. To produce the joint in the section of the vessel and to join the nozzle and flanges attached to vacuum vessel outer surface, TIG welding was used to achieved ultra-high vacuum range of 1×10^{-9} mbar pressure in the chamber.

Ishimaru [4] has recognized research work on the aluminum alloy vacuum vessel in achieving an ultimate pressure of 10^{-13} Torr. Vacuum beam chambers in accelerators generally require a complicated profile, having a distributed pump and heating and cooling structures. A complicated cross-section of the vessel was developed by an extrusion process using porthole dies. Aluminum alloy 6063-T6 provides superior performance during extrusion. The outer body and main chamber were developed by a special extrusion process and the three pieces of the main chamber were joined by tungsten inert gas (TIG) manual welding.

Chen et al. [5] has focused his research work on the bending magnet of SRRC synchrotron light source developed from AA6061-T6. To develop a 35 mm thick vessel, the AA6061-T6 plate is first machined with NC machining in an ethyl alcohol vapor. Subsequent to machining, the two thick plates of the B-chamber were extruded to obtain an elliptical cross-section and after that chamber, TIG welding was used with no other chemical cleaning procedure. For long circumferential welding, the base material was preheated up to 70–80°C to prevent deformation. Then TIG welding was used for fabrication. After fabrication, at 150°C bakeout temperature, an ultimate vacuum pressure of 1×10^{-10} Torr and leak rate of 1×10^{-10} torr.l.s^{-1} was achieved.

Reich et al. [6] has conducted his research work on the development of vacuum vessels of wendelstein 7-X in, which is the superconducting magnet system that is bounded among two toroidal formed vacuum vessels. Research work has established a manufacturing process adopted for fabrication. A one side (V) weld seam and double face (X) weld seam are filled and welded by TIG welding on stainless steel 316 LN ASTM. For the port, the opening is fabricated by water jet abrasive machining. During fusion welding the of vacuum vessel: weld distortion, backing out of vessel for higher temperature, non-uniform strength and quality of the weld are the problems faced during fabrication of vacuum vessel. Aluminium alloy can get oxide, warpage and distortion on the weld.

2.2 Vacuum system material selection

The general outline design of the vacuum structure is controlled by the kind of the progress involved and the ultimate vacuum pressure to be achieved in a specific application. The definite design outline will be influenced by the appropriateness and scope of the materials and accessible components obtainable and thus the particular choice of vacuum material is crucial for the performance and cost of the vacuum system to be optimized.

Vacuum vessel material selection criteria:

1. The material provides a lower surface and volumetric outgassing rate.

2. Completely non-magnetizable metal, which means magnetically neutral and relative permeability $\mu = 1$

3. The material has superior thermal conductivity. High and ultra-high vacuum levels require quicker and high vacuum pumping so this material can bake-out quickly and consistently yet at low temperatures.

4. Material with minimum residual radioactivity.

5. The material has higher chemical and corrosion resistance with excellent machinability and high weldability.

2.2.1 Vacuum vessel materials

The following are vacuum vessel materials which are most widely used.

1. **Austenitic stainless steel** is the most recognized and preferred material for high and ultra-high vacuum vessel systems. The outgassing rate for stainless steel is 6×10^{-9} Torr liter/sec/cm^2.

   - **304 L stainless steel:** a lower carbon variant of steel that is used for ultra-high vacuum region requirement system.
   - **316 L stainless steel:** low carbon and magnetic stainless steel
   - **321 stainless steel**: preferred when low magnetic permeability is needed.

2. **Mild steel** is utilized for modest vacuum pressure above 10^{-6} Torr. Material outgassing rate is lower (5×10^{-6} Torr liter/sec/cm^2) with proper (e.g. nickel) plating.

3. **Aluminum and its alloys** [7] are another class of widely recognized vacuum materials for space industry utilization. They possess excellent machinability and have a lower outgassing rate of 7×10^{-11}. Among the aluminum alloy series, 2XXX (Al-Cu), 6XXX (Al-Mg-Si) and 7XXX (Al-Zn) series alloys are easily and readily welded for vacuum application by solid-state friction stir welding. Aluminum wire rings are also utilized as economical gaskets in demountable seals. Ishimaru [8] has developed an aluminum alloy ultra-high vacuum system for the purpose of constructing a high-energy particle accelerator. During the course of the development; however, it turned out that it exhibits an extremely low outgassing rate less than 10^{-13} Torr/liter/cm^2.

   Chen et al. [6] developed and tested an aluminum vacuum chamber for bending magnet of the SRRC synchrotron light source. An aluminum alloy was chosen because it showed the minimum residual radioactivity among the available materials. Aluminum composites are generally utilized for the ultra-high vacuum chambers because of their advantageous qualities such as great machinability, high thermal conductivity and low outgassing rate.

4. **Copper** has good machinability with higher corrosion resistance. Typically, copper is incompatible for a high vacuum because of its outgassing difficulty. Copper is impervious to hydrogen and helium and has low affectivity to water vapor, yet it is assaulted by mercury.

5. **Nickel** is usually recognized as a mechanical component in vacuum tubes. It is fairly economical with respectable spot weldability and machinability with a high melting point and is resistant to many corrosive fluids and atmospheres.

6. **Tungsten** material is utilized when vacuum systems are subjected to high-temperature applications as well as for electron/ion filaments optics. When

No	Flange type	Vacuum level	Sealing mechanism
1	KF Flange	Medium to Very High Vacuum	Rubber type O-ring gasket 1. Neoprene: Up to High Vacuum 2. Viton: High and Very High Vacuum
2	ASO/IS		
3	Conflat	Ultra-high vacuum	Metal-based sealing
4	NEC		

Table 1.
Sealing mechanism selection [10].

tungsten is mechanically deformed or subjected to the extremely high-temperature region, it becomes brittle [9].

7. **Brass** is reliable for applications wherever a higher corrosion resisting ability and outgassing rate of 8×10^{-7} order is required. The outgassing rate of zinc can be controlled by nickel plating it. Adding zinc into brass may cause some difficulties for high and ultra-high vacuum region.

2.2.2 Flange and sealing mechanism material

In a vacuum system, the selection of the sealing material between two contacting surfaces depends upon the flange type used. Following are the different sealing materials used (**Table 1**).

3. Applications of vacuum vessel

1. **Space environment simulation technology**: The most widely used vacuum vessel for space application is used in the space environment simulation laboratory. An ultra-high vacuum vessel provides a space vacuum situation on earth so that we can learn about the behaviour of any component in space. The vacuum vessel provides approximately the same vacuum pressure as in space.

2. **Product testing and laboratory applications**: To conduct product testing and study their behaviour at variable pressures facilitated by different vacuum pressure range of vacuum vessel.

3. **Carrying loads into space**: A vacuum vessel is used to carry and hold a load into space. While on earth, the load is put into the vacuum vessel and it will be opened in a vacuum.

4. **Holding and processing plasma at low pressure**: To successfully hold and maintaining plasma below atmospheric pressure, a vacuum vessel is needed. The vacuum vessel is provided with a protective layer which cannot react with the atmosphere and plasma.

5. **Thermal vacuum imitation**: This is a vacuum chamber in which radiative thermal environs have been controlled. The thermal vacuum simulation vessel provides a space where superior temperature and inferior atmospheric state is necessary for research.

6. **Different atmospheric pressure simulation**: A vacuum vessel provides a low pressure region which is below the atmospheric pressure to hold and store different chemicals at different pressures and allows them to be processed within the chamber.

7. **Leak testing of the packaging**: For any vacuum packaged object, it is leak tested in a vacuum chamber. If any leak is present in the packaging, the pressure rises in the vacuum vessel.

4. Conclusion

Aluminum and its alloys have been widely used in the space, aerospace and aircraft industry because of their certain suitable property like high strength to weight ratio, low outgassing rate (1×10^{-6} Torr-L/sec-cm^2), high resistance to corrosion, high thermal conductivity, low solubility of hydrogen, economy and easy availability when compared to stainless steel. For space application, the product is lightweight, durable and extraordinarily strong, space-age aluminum alloys were the best choice to build vacuum vessels that have a very low outgassing rate and high vacuum holding capacity. To develop an aluminum alloy square configuration vacuum system, there are many methods, for example, friction stir welding fabrication process which results in sound, defect-free, leak-proof uniform material joints between two joining surfaces of aluminum alloys. Vacuum vessels developed by this method have very good dimensional stability without distortion of the surface, low leak rate with a high vacuum holding capacity when compared to fusion and arc welding.

Acknowledgements

The author would like to thank the Department of Mechanical Engineering, LDRP- ITR, Gandhinagar, Gujarat for their support.

Author details

Rushit Mistry and Kaushal Bhavsar*
Department of Mechanical Engineering, LDRP-ITR, Gandhinagar, Gujarat, India

*Address all correspondence to: kaushal_me@ldrp.ac.in

References

[1] Mishra RS, Ma ZY. Friction stir welding and processing. Materials Science & Engineering R: Reports. 2005;**50**(1-2):1-78. DOI: 10.1016/j.mser.2005.07.001

[2] Dalder EC, Pastrnak JW, Engel J, Forrest RS, Kokko E, Ternan KM, et al. Bobbin-tool friction-stir welding of thick-walled aluminum alloy pressure vessels. Welding Journal. 2008;**87**(4):40-44. 2007 Jun 6;87(UCRL-JRNL-233687)

[3] Jadeja KA, Bhatt SB, Rathod K, Patel KM, Prajapati VR, Acharya KS, et al. ADITYA upgrade vacuum vessel: Design, construction, testing, installation and operation. Fusion Engineering and Design. 2017;**124**:558-561. DOI: 10.1016/j.fusengdes.2017.03.148

[4] Ishimaru H. Ultimate pressure of the order of 10^{-13} Torr in an aluminum alloy vacuum chamber. Journal of Vacuum Science & Technology, A: Vacuum, Surfaces, and Films. 1989;**7**(3):2439-2442. DOI: 10.1116/1.572695

[5] Chen JR, Chen GS, Wang DJ, Hsiung GY, Liu YC. An aluminum vacuum chamber for the bending magnet of the SRRC synchrotron light source. Vacuum. 1990;**41**(7-9):2079-2081

[6] Reich J, Gardebrecht W, Hein B, Missal B, Tretter J, Wanner M, et al. Manufacture of the vacuum vessels and the ports of Wendelstein 7-X. Fusion Engineering and Design. 2005;**75**:565-569. DOI: 10.1016/j.fusengdes.2005.06.245

[7] Suemitsu M, Kaneko T, Miyamoto N. Aluminum alloy ultrahigh vacuum chamber for molecular beam epitaxy. Journal of Vacuum Science & Technology, A: Vacuum, Surfaces, and Films. 1987;**5**(1):37. DOI: 10.1116/1.574134

[8] Ishimaru H. Developments and applications for all-aluminum alloy vacuum systems. MRS Bulletin. 1990;**15**(7):23-31. DOI: 10.1116/1.572695

[9] Sanderson A, Punshon CS, Russell JD. Advanced welding processes for fusion reactor fabrication. Fusion Engineering and Design. 2000;**49**:77-87. DOI: 10.1016/S0920-3796(00)00407-5

[10] Avasthi DK, Tripathi A, Gupta AC editors. Proceeding of the school on Ultra High Vacuum Techniques. Allied Publishers Pvt. Limited;1999. p. 192-194

Chapter

An Optimization Model for a Manufacturing Plant Using Cellular Manufacturing: A Review

Mrugesh S Mistry and Kirti H Niralgikar

Abstract

Using machine cells, different machines are orderly clustered together with an aid of group technology concepts contributing towards lean manufacturing. Among the different optimization techniques, the suitable one can be adopted for optimization of manufacturing plant using cellular manufacturing. Plant layouts and the sequence of operations are to be analyzed. In the present work, by considering the static part population, a robust cellular manufacturing system is likely to be developed by considering multiple processing routes since robustness is the most advanced, trending, modern and prominent approach of cellular manufacturing. The cost can be considered as an objective function and can be optimized using Computer Aided Process Planning (CAPP) concepts as the CAPP is the only bridge (link) between CAD and CAM modules and is essential in all of the industries. Here, the review regarding the CMS and robustness is undertaken and highly emphasized.

Keywords: cellular manufacturing, robust CMS design, static part population, multiple processing routes, CAPP

1. Introduction

Job shop and flow type manufacturing systems are the traditional manufacturing systems that do not satisfy needs of clients with low manufacturing operations cost and cannot maintain a quality level that signifies a capable production system. Mostly, time spent in non-productive activities by the jobs in job shop manufacturing majorly waiting in the queue is high and rest time spent is in lot setup and processing. For high production volume, the operation sequence of the product is considered for arrangement of machines and that is how line manufacturing works flow. The machines are specialized which are intended to perform limited fixed operations. So, flow line manufacturing system is not flexible. Nowadays the product design phase demands manufacturing systems which can be configured again as per requirement and these manufacturing systems should be innovative enough to eliminate most of the drawbacks of conventional manufacturing methodology. Different types of parts can be recognized and put together in terms of their similarities in design and/or manufacturing attributes. GT is a unique philosophy whose concept is to find the solution of many questions with general rules. Efforts in terms of time and cost can be decreased using GT concepts (see **Figure 1**) (**Table 1**).

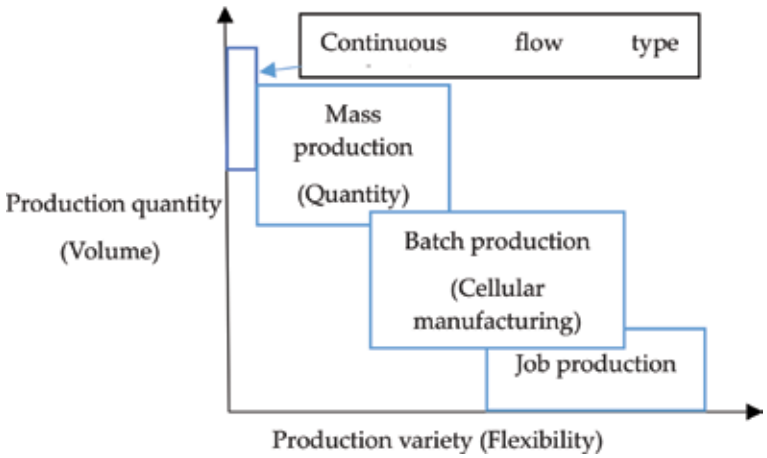

Figure 1.
Different levels of production quantity (volume) and product variety (flexibility) for production systems.

Sr. no.	Type of production	Type of facility used	Type of layout used
1.	Job shop production	Stand-alone machines	Fixed position layout and process layout
2.	Batch (lot) type production	Cellular manufacturing system (CMS)	Cellular layout and process layout
3.	Mass (quantity) production	Transfer lines	Process layout
4.	Flow (continuous) type production	Continuous lines	Product layout

Table 1.
Types of facilities and layouts used for different types of production systems.

2. Cellular manufacturing philosophy

In recent trends, a prominent example of GT implementation is the cellular manufacturing philosophy. The similarity in design and/or manufacturing attributes among parts promotes standardization and common processing. The specialty of CMS is to divide the available machines into some machine cells [1]. CMS increases the flexibility and variety in production. This leads to limiting the drawbacks of job shop and flow type manufacturing philosophies. CMS offers main advantages like significant improvement in material flow, reduction in material storage, reduction in material handling. These advantages give reduced cumulative lead time as an outcome [1].

2.1 CMS approaches

Generally, there are two types of CMS approaches for the creation of machine cells and part families. (1) Simple CMS approach: This is used to alter part machine matrices and (2) The sophisticated CMS approach: This one is used to handle constraints like maximum cell numbers, varying demand for products and setup. Under each of these two, there are again two types of CMS according to part population. (1) CMS with static part population: The market demand and part

population remain constant over a certain period of time in this type of CMS. This CMS is best suited for a single level planning horizon. (2) CMS with dynamic part population: The market-based environment is considered in this type of CMS. Particularly, varying demand of product in market and the machine breakdown have an effect on the performance of a CMS design from one period to other.

In real world manufacturing cases, design of CMS becomes difficult and essentially requires allotment of resources in various machine cells and creation of part families. Therefore, a robust CMS design is necessary to be obtained to manage changes in size of the product demand, processing times, sequence of operations, material handling, plant layout and maintenance of machines without affecting the continuity of production [1].

2.2 A robust CMS design approach

In a particular cellular manufacturing environment, a robust model for constant production can be designed. Each part has multiple process plans and alternative process routes. Design of robust machine cell is considered where static part population is assumed. A part goes through the sequence of multiple manufacturing operations. The sequential operations are carried out in different machine cells. They include similar machines having more than one scope of operations and restricted potential for processing part families [1].

Before clustering the machine cell, it is essential to determine the process route which is optimal rather than adopting multiple process routes predefined by users. At the starting of planning phase, this model can arrange machines in manufacturing cells and the optimum production plan can be determined after that. The motive of a robust CMS design approach is to optimize overall cost. Overall cost is affected by different costs: [1]. machine attainment cost (C_1), machine working cost (C_2), production cost for part operation (C_3), intercellular material handling cost (C_4), intracellular material handling cost (C_5) and subcontracting cost for part operation (C_6).

A robust CMS design has the following constraints [1]. Each machine has a part operation assigned to it. The part demand is satisfied in a predefined time frame. Inner part operation is limited to the capacity and availability of machines. The material flow conservation is taken into consideration. The number of machine types is less than or equal to the total number of the same machines. The cell size ranges between upper and lower cell limits. Logical binary and positive integers are essential for the formulation of equations with restrictions and constraints (**Figure 2**).

2.3 Robust optimization model (ROM)

This model was introduced in 1995 by Mulvey for handling the trade-off associated with the anticipated cost and its varying randomly determined programs [2].

Robustness has two types: solution robustness in which solution is near to optimum total scenarios and model robustness in which solution is near to feasible in total scenarios [2].

The main objective of robustness is "to find a robust solution which ensures that any realization of the scenario is almost the optimum in response to changing input data. Solution of model robustness should be robust with respect to feasibility if it remains "almost" feasible for all the scenarios" [2]. The goal of the proposed model is to optimize total cost of holding, material handling, external transportation and fixed costs for carrying out manufacturing operations for each part in each plant, machine attainment cost and to meet uncertainty demands in various cases [2].

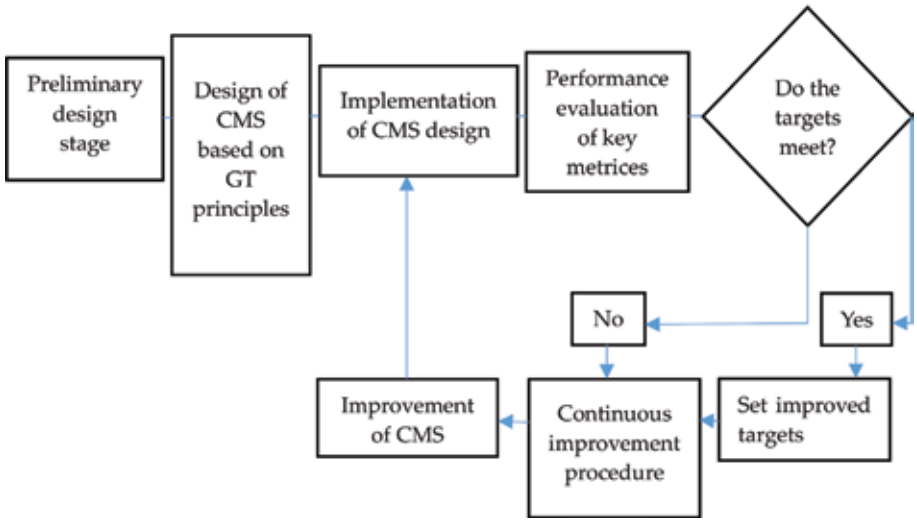

Figure 2.
A robust machine cell design flow-chart.

3. Description of CMS study

Eric Molleman et al. proposed that cellular manufacturing system (CMS) should reflect the interrelated features like cell formation and functionally organized manufacturing units. Analysis of these features offers some factors that are required to be taken into consideration. The data mentioned here depends on document study and asking questions of different level employees. The documents analyzed consist of process planning sheets, performance reports and review cards of important meetings and audits.

The main merit of cellular manufacturing is its ability to connect all types of sequential operations in the organization. Various manufacturing steps are put together through GT. Moreover, the sequential support functions including process planning and production planning can be more easily functionalized in the case of CM [3]. Logendran et al. found that allocation of parts and machines to every machine cells in CMS results in different types of features consisting grouping of parts into part families that is done by attainment of machines to part families and simultaneous arrangement of parts using GT. A relevant model and an algorithm have been developed and presented for converting an actual FM system into a CM system. All operational conditions and factors related to the analysis have been included in the development of the model [4]. Bazargan-Lari et al. described the use of the latest included model for designing cellular manufacturing, including the parts/machines and their clustering and material layout designs. Combined layout design can be extended to address all stages in the design of machine cells. It was shown how the real cell-formation algorithms can be modified and used to generate various part machine incident matrices. This proposed, combined model provides multiple efficient alternative solutions according to different cell-partition methods. It offers the means to calculate every alternative of major benefits and criteria such as needed area for manufacturing, calculation of material handling, machine criteria, planning horizon etc. The capacity of the proposed method was shown by applying it to a real manufacturing CM case [5]. Selim Akturk reported that the motive of the model is to optimize the altering cost of production subject to manufacturing and inventory balance constraints for part families and different items, capacity feasibility constraints for GT cells and resources over the planning horizon. An average planning model of the cell loading problem

for CM systems has been developed to optimize the variable production cost. The proposed approach has several merits over models in the current literature on layer by layer planning and cell formation [6]. Shayan et al. reported some of the major results and discussions of the effects of using a cellular manufacturing environment on the production rate of people, management and facilities. The cell formation in the industrial production unit under investigation clearly has positive results on the employee's behavioral patterns such as committed work approach, innovative work patterns that causes better productivity. The performance improvement in turn decreases the production costs and causes quality improvement of the production [7]. Urban Wemmerlöv et al. reported a large number of research topics related to cellular manufacturing, discussed the necessity for their investigation and suggested proper methods for their study [8]. Ghezavati et al. reported a novel mathematical robust approach for a cellular manufacturing problem combined with important factors of supply chain network qualities in the presence of uncertain inner parameters and exterior parameters [9]. Wang et al. prescribed an assignment of machine-cells to linear locations in order to optimize the material handling cost for different cells occurred because of problematic machines in a cellular manufacturing system [10]. Burgess et al. compared a factory designed as a traditional job shop for the identical firm structured as a hybrid firm including cellular manufacturing unit [11]. Javadi et al. presented a comprehensive model for cell formation and layout design in CMS [12]. Cao et al. formulated a mathematical programming technique for optimal lot division into alternative ways to consider for the effect of manufacturing run length on part quality in a CMS environment [13]. Logendran et al. developed and presented a new approach consisting of two important factors for deciding optimal and near-optimal machine-part incident matrix clustering in cellular manufacturing [14]. Madhusudanan Pillai et al. presented a new approach of robust design for creating part families and machine cells that can handle all the variations in demands and product mixes without any relocations [15]. Taboun et al. presented a mixed integer mathematical model for simultaneous machines and parts grouping and assignment when part incident machine mix matrices and demand changes across multiple timeframes according to forecasts and/or product life cycles [16]. Mak et al. presented a method to solve the manufacturing cell formation and the production scheduling problems for designing virtual VCMS [17]. Bazargan-lari et al. developed a new model based on merging pre-emptive goal programming and simulated annealing for machine layout in cells [18]. Mohammad Rezaei-Malek et al. considered decision-making as an operator's personal quality index for designing a psychologically consistent CMS [19]. Vohra et al. presented a non-heuristic network approach to creating manufacturing cells with the least intercellular movements [20].

4. Conclusions

Considering single period production planning and part population with static market demand, a novel design of robust CMS can be developed.

- Without affecting the machine cell configuration, flexibility in planning of manufacturing operations can be obtained through RCMS. Also, the overall cost can be optimized as an objective function using robustness.

- The model can deal with the practical and realistic CMS problems. Thus, the technique of the robustness would be used to validate the results of CMS studies.

- Therefore, the details of this present reviewed work can be implemented to an industrial case study of a radiator manufacturing plant using CMS regarding robustness.

Author details

Mrugesh S Mistry and Kirti H Niralgikar*
Sardar Vallabhbhai Patel Institute of Technology (SVIT), Vasad, India

*Address all correspondence to: kirtiniralgikar.mech@svitvasad.ac.in

References

[1] Deep K, Singh PK. Design of robust cellular manufacturing system for dynamic part population considering multiple processing routes using genetic algorithm. Journal of Manufacturing Systems. 2015;**35**:155-163. DOI: 10.1016/j.jmsy.2014.09.008

[2] Aalaei A, Davoudpour H. A robust optimization model for cellular manufacturing system into supply chain management. International Journal of Production Economics. 2016;**183**(c): 667-679. DOI: 10.1016/j.ijpe.2016.01.014

[3] Molleman E, Slomp J, Rolefes S. The evolution of cellular manufacturing system—A longitudinal case study. International Journal of Production Economics. 2002;**75**:305-322. DOI: 10.1016/S0925-5273(01)00139-6

[4] Logendran R. Methodology for converting a functional manufacturing system into a cellular manufacturing system. International Journal of Production Economics. 1993;**29**:27-41. DOI: 10.1016/0925-5273(93)90021-C

[5] Bazargan-Lari M, Kaebernick H, Harraf A. Cell formation and layout designs in a cellular manufacturing environment a case study. International Journal of Production Economics. 2010;**38**(7):1689-1709. DOI: 10.1080/002075400188807

[6] Selim Akturk M, George R. Wilson: A hierarchical model for the cell loading problem of cellular manufacturing systems. International Journal of Production Economics. 2010;**36**(7):2005-2023. DOI: 10.1080/002075498193084

[7] Shayan E, Sobhanallahi A. Productivity gains by cellular manufacturing. Production Planning and Control: The Management of Operations. 2010;**13**(6):507-516. DOI: 10.1080/09537280210157983

[8] Wemmerlöv U, Hyer NL. Research issues in cellular manufacturing. International Journal of Production Economics. 2010;**25**(3):413-431. DOI: 10.1080/00207548708919850

[9] Ghezavati VR, Sadjadi SJ, Dehghan Nayeri M. Integrating strategic and tactical decisions to robust designing of cellular manufacturing under uncertainty fixed suppliers in supply chain. International Journal of Computational Intelligence Systems. 2012;**4**(5):837-854. DOI: 10.1080/18756891.2011.9727835

[10] Wang S, Sarker BR. Locating cells with bottleneck machines in cellular manufacturing systems. International Journal of Production Economics. 2010;**40**(2):403-424. DOI: 10.1080/00207540110073109

[11] Burgess AG, Morgan I, Vollmann TE. Cellular manufacturing: Its impact on the total factory. International Journal of Production Economics. 2007;**31**(9):2059-2077. DOI: 10.1080/00207549308956844

[12] Javadi B, Jolai F, Slomp J, Rabbani M, Tavakkoli-Moghaddam R. An integrated approach for the cell formation and layout design in cellular manufacturing systems. International Journal of Production Economics. 2013;**51**:6017-6044. DOI: 10.1080/00207543.2013.791755

[13] Cao D, Defersha FM, Chen M. Grouping operations in cellular manufacturing considering alternative routings and the impact of run length on product quality. International Journal of Production Economics. 2008;**47**(4): 989-1013. DOI: 10.1080/00207540701529543

[14] Logendran R. Impact of sequence of operations and layout of cells in cellular manufacturing. International Journal of Production

Economics. 2007;**29**(2):375-390. DOI: 10.1080/00207549108930077

[15] Madhusudanan Pillai V, Subbarao K. A robust cellular manufacturing system design for dynamic part population using a genetic algorithm. International Journal of Production Economics. 2008;**46**(18):5191-5210. DOI: 10.1080/00207540701332658

[16] Taboun SM, Merchawi NS, Ulger T. Part family and machine cell formation in multi period planning horizons of cellular manufacturing systems. Production Planning and Control: The Management of Operations. 2010;**9**(6):561-571. DOI: 10.1080/095372898233812

[17] Mak KL, Peng P, et al. An ant colony optimization algorithm for scheduling virtual cellular manufacturing systems. International Journal of Computer Integrated Manufacturing. 2007;**20**(6):524-537. DOI: 10.1080/09511920600596821

[18] Bazargan-lari M et al. An approach to the machine layout problem in a cellular manufacturing environment. Production Planning and Control: The Management of Operations. 2010;**8**(1):41-55. DOI: 10.1080/095372897235550

[19] Rezaei-Malek M et al. Towards a psychologically consistent cellular manufacturing system. International Journal of Production Economics. 2010;**55**(2):492-518. DOI: 10.1080/00207543.2016.1192299

[20] Vohra T et al. A network approach to cell formation in cellular manufacturing. International Journal of Production Economics. 2007;**28**(11):2075-2084. DOI: 10.1080/00207549008942854

Chapter

A Review on Machinability Aspects of Ti-6Al-4V: A Titanium Grade 5 Alloy

Ayanesh Y. Joshi and Anand Y. Joshi

Abstract

Ti-6Al-4V (Grade 5) is a very popular titanium alloy used in the automobile, biomedical, chemical and aerospace industries as it possesses properties like high strength to low weight ratio, capability to retain strength even at elevated temperatures, corrosion resistance and very good biocompatibility. However, Ti-6Al-4V possesses low machinability owing to its properties of low thermal conductivity, high hardness and high chemical reactivity at elevated temperatures, and low elasticity. This paper reviews the machining difficulties conferred by various researchers and their apparent solution, which can assist in reducing tool wear and achievement of a high surface finish. The impact of titanium properties on the machinability is also discussed in the paper.

Keywords: titanium alloy, Ti-6Al-4V, machinability, tool-wear, lubrication effect, chip formation

1. Introduction

Titanium and titanium alloys find their extensive application in the field of aerospace as they have excellent specific strength (ratio of strength to weight) even at raised temperatures, in addition to their exceptional corrosion resistance and their fracture resistant characteristics. These characteristics have resulted in rapid growth of titanium industries in the last few decades [1]. Titanium is gaining popularity in commercial and industrial applications, such as chemical processing, surgical implantation, petroleum refining, nuclear waste storage and pollution control, food processing, electro-chemical and marine applications [2, 36]. However, titanium and titanium alloys are expensive because of the difficulty of melting, intricacy of the extraction-process, fabrication and machining complications [2, 3]. Basic formation methods like forging (isothermal), casting and powder metallurgy are followed to reduce the costs of titanium components [4, 5]. Longer service life and excellent properties counterbalance the high cost of production.

The machinability of titanium and titanium alloys is poor because of several properties of the materials. Siekmann pointed out that "Irrespective of the techniques that are employed to transform titanium into chip, it's machining would always be a problem." [6]. Chemically, titanium is very reactive and, hence, during machining it might get welded to the cutting tool and lead to chipping and early

failure of the tool. The tool/workpiece interface temperature will be high as it has low thermal conductivity, which affects the tool life adversely. Because of the high strength maintained at elevated temperatures and low elasticity, its machinability is further impaired [7]. Many large companies like Rolls-Royce and General Electrics have invested large sums of money in developing techniques to reduce machining cost because of poor machinability of these alloys.

Researchers have attempted various methods to improve machining of titanium alloy but cost is still a challenge to the titanium alloy part manufacturer and hence, research has to focus on new technologies and methods. This article emphasizes metallurgical aspects, chip formation, tool wear, lubrication during machining and surface integrity of Ti-6Al-4V. These factors are responsible for manufacturing challenges during working with titanium alloy. At the end, observations are summarized along with some recent techniques and future research scope.

2. Metallurgical aspects of Ti-6Al-4V, titanium alloy–grade 5

Titanium is an element (atomic number 22; atomic weight 47.9 and symbol Ti) [8]. Pure titanium experiences a transformation (allotropic) at 882°C, changing from the α - phase (low-temperature CPH structure) to the β - phase (higher-temperature BCC structure). Alloying elements, such as oxygen (O) and aluminum (Al) cause an increase in the transformation temperature, whereas tin (Sn) dissolved in titanium, does not have such an effect, such elements are called α - stabilizers. Elements that decrease the phase-transformation temperature are called β - stabilizers. Significant β alloying additions are vanadium (V), molybdenum (Mo) and niobium (Nb). They are generally transition metals [9]. Elements are alloyed in titanium to stabilize the α - phase or β - phase that modifies the transformation temperature and changes the shape as well as the extent of α + β field [10, 11]. Aluminum (Al) is a strengthening element at ambient and elevated temperatures up to 550°C. The density (low) of Al is a vital advantage. O, N and C are observed as impurities in commercial alloys. For strength and fabricability, O is used as a strengthening agent to provide various grades of commercially pure titanium.

The alloys are categorized into four main groups; (1) **Unalloyed Titanium:** Alloys have excellent corrosion resistance but low strength properties which can be improved by adding O and Fe. (2) **α and near-α Alloys:** These alloys contain α stabilizers and have an exceptional creep resistance property. These alloys have very minimum quantity β stabilizers, but behave more like conventional α alloys. (3) **α + β Alloys:** At room temperatures, these alloys offer a mixture of α and β stabilizers. They are largely used in aerospace industries and an example is Ti-6Al-4V. (4) **β Alloys:** Alloys have significant quantity of β stabilizers and a high density and high hardenability [39].

Wt %	Material	Wt %	Material
0.005%	Yttrium (Maximum)	5.5–6.75%	Aluminum
0.20%	Oxygen (Maximum)	0.05%	Nitrogen (Maximum)
0.40%	Other Elements (Total)	3.5–4.5%	Vanadium
0.08%	Carbon (Maximum)	0.015%	Hydrogen (Maximum)
Balance	Titanium	0.30%	Iron (Maximum)

Table 1.
Chemical composition of Ti-6Al-4V.

In the late 1940s, the Ti-6Al-4V alloy was developed. Ti-6Al-4V is sometimes called TC4 and is a two phase α + β titanium alloy, with aluminum and vanadium as alpha and beta stabilizer respectively. The Ti-6Al-4V alloy is the most commonly and commercially used titanium alloy. **Table 1** shows the chemical composition and **Table 2** shows the physical properties of the alloy.

It is noted from the property table that the alloy has good Mechanical properties with respect to steel but has poor thermal properties. Ti alloys specific heat is higher than steels but its volumetric specific heat is less as the density is much lower. The strength is because of the alloying content but an increase in β content results in poor machinability.

Property	Ti-6Al-4V (annealed bar)	Ti-6Al-4V (solution treated and aged bar)	AISI-1045 (cold drawn)
Tensile strength (MPa)	895	1035	625
Yield strength (MPa)	825	965	530
Elongation (%)	10	8	12
Reduction in area (%)	20	20	35
Modulus of elasticity tension (GPa)	110	—	207
Hardness (Hv)	340	360	179
Density g/cm^3	4.42	—	7.84
Specific heat J/kg.°C	560	—	486
Thermal conductivity W/m.K	7.2	—	50.7

Table 2.
Physical properties - Ti-6Al-4V.

3. Machining of titanium alloy

Machinability of any material refers to the ease with which a material/metal can be cut (machined) permitting removal of material with satisfactory finish efficiently. The machinability index of a material is usually determined based on measures such as cutting force, chip formation, tool wear, cutting temperature, tool life, surface integrity and chip size.

Ti-6Al-4V is categorized as a difficult to machine material by traditional methods because of its physical, chemical and mechanical properties. Ti-6Al-4V has high hardness, low elastic modulus, low thermal conductivity, strength at elevated temperature and metallurgical characteristics that make it slightly more difficult to machine than equivalent hardness steels. The influence of titanium alloys properties on its machinability is summarized in **Table 3** [13–16, 19].

Metallurgical properties of the material challenge the workpiece material in the region near the cutting edge and lead to a severe strain and numerous physical and metallurgical alterations [17]. Poor thermal conductivity of the alloys results in accretion of heat in the primary shearzone that results in localized shear and chip segmentation, leads to temperature increases and α - β phase transformation in the secondary deformation zone [18].

Property	Description
Thermal conductivity	• Concentration of heat on the tool cutting edge and face as the thermal conductivity is low causes a negative effect on tool life
Chemical reactivity	• Reactivity with gases such as hydrogen, oxygen and nitrogen leads to formation of hydrides, oxides and nitrides respectively which cause reduction in the fatigue strength of the alloy • Development of hard solid-solution owing to internal diffusion of oxygen and nitrogen cause surface hardening which increases tool wear and reduces the fatigue strength of machined surface • Smearing and chipping of the workpiece surface as reaction between workpiece and cutting tool material causes rapid tool wear
Elastic modulus	• Because of low elastic modulus, slender workpiece allows deflection under tool pressure, causing chatter and tolerance problems
Hardness and strength	• Higher cutting forces are required to machine because of high temperature strength and hardness of titanium alloys, resulting in deformation of the cutting tool during cutting process • Because of high dynamic shear strength of the alloy, during cutting process abrasive saw-tooth edges are generated which induces tool notching
Work hardening	• The work hardening causes nonexistence of built-up edge at the rake surface of the tool which increases the shearing angle that results in a thin-chip to contact a fairly trivial area on the cutting face and hence subsequent raise in bearing loads per unit area • Because of the friction between the chip and the bearing area combined with high bearing stress, there is a remarkable heat increase in a very small area of the cutting tool which results in formation of craters close to the cutting edge and promotes rapid tool breakdown

Table 3.
Titanium properties and its effect on machinability.

3.1 Chip formation

To minimize the negative effects of the chip produced while machining on cutting tool and surface of the workpiece, it's important to comprehend the cutting conditions as the chips produced during machining affects temperature of the cutting zone, machining forces, workpiece's surface integrity and tool life. The analyses of chips developed during machining of titanium alloys indicated that adiabatic shear (thermo-plastic instability) formation bands is the most studied feature [20, 21]. In titanium alloys, when the degree of thermal softening goes above the degree of strain hardening, adiabatic shear occurs [22]. While operating at low cutting speeds, the initiation and propagation the crack starts from the tip of the tool and spreads to the workpiece free surface and/or vice versa [23]. There will be noteworthy periodic deviation of machining forces because of localization of the shear, subsequently periodic variation of machining forces enforces fatigue to the tool or might result in chipping or breakage of the cutting tool and hence is not desired [24]. Experiments were carried out to form chips of Ti-6Al-4V at a high cutting speed, ranging from 30 to 6000 m/min and the results indicated that the segmentation structure changes at a cutting speed beyond 2000 m/min and there was no variation in specific cutting energy [25, 26].

In the case of Ti-6Al-4V alloys, segmented chips form at all speeds, but at high speeds it becomes continuous macroscopically and hence can be concluded that the microstructural state of the material strongly influences the chip formation mechanism. This is a major concern during machining of these alloys.

3.2 Surface integrity

It is the nature of the surface of a workpiece after being modified by a manufacturing process that has a noteworthy impact on the product reliability, performance and durability. These modifications include metallurgical, chemical, mechanical and other changes. Though the changes are restricted to a thinner surface layer, it might have a limit on the component quality or render the surface unacceptable. So it's important to improve the product's quality. Surface integrity is a prime requirement as titanium is used for parts requiring the highest reliability. During machining, the surface of these alloys is easily impaired due to its poor machinability. Therefore, it is required to optimize process parameters for improved surface finish and tool life. The damage appears in the form of work hardening, formation of heat-affected zones, micro cracks, built-up edge, and tensile residual stresses [12, 37].

3.3 Cutting fluids

Cutting fluids are used to reduce high temperatures generated in the machining zone during machining. Use of cutting fluid increases the tool life, improves surface conditions and increases process efficiency. M. Venkata Ramanaa et al. performed an experiment at low cutting speeds at different machining conditions such as dry machining, using servocut oil mixed with water and synthetic oil conditions to find out its effect on surface roughness. Experimental results indicated that for dry machining, higher cutting speeds resulted in higher surface roughness compared to servocut oil mixed with water and synthetic oil conditions. Results indicated that, compared to other conditions, with synthetic oil, the surface roughness is less [27, 28]. Researcher Ibrahim Deiab et al. explored the effect of various lubrication parameters on the surface roughness (Ra) [29].

At a higher feed rate, surface roughness is higher. For synthetic oil conditions, the surface roughness is low at lower feed rates, but at higher feed rates, surface roughness is high for servocut oil added with water conditions compared to dry and synthetic oil conditions.

Surface roughness is low for lower depth of cut for synthetic oil conditions compared to dry and servocut oil with added water conditions. Results also indicate that the value of surface roughness is high for a higher depth of cut for synthetic oil conditions compared to dry and servocut oil mixed with water conditions [28]. It is understood that at low feed rates, the surface roughness is less and it increases as the speed increases for the same feed rate. Conventional flood cooling mechanism is preferable when operating at low feed rates and cryogenic machining is to be used when operating at higher feed rates for better results.

Moaz H. Ali et al. modeled a finite element model to forecast the effect of varied feed rates on surface roughness for dry milling conditions. FEM can help us to reduce machining time and manufacturing costs at the same time. Accuracy of the experimented and predicted cutting force values was about 97%. Results also indicated that the cutting forces had an insignificant effect on surface roughness [29].

3.4 Tool wear

The tool wear depends on tool and workpiece material, tool geometry, machining parameters, machine-tool characteristics and application of cutting fluids. The wear land is the cutting tool area near the cutting edge, which gets worn while machining [31]. The basic types of tool wear are flank wear and crater wear. Tool wear characteristics are signified as a relation between material wear and sliding

distance. Tool wear occurs in three different regions. **Region 1 - Initial wear region:** where wear rate is relatively high as it is depending on accelerated wear due to damage of tool layer while manufacturing, **Region 2 - Steady-state region:** where normal operation for the cutting tool occurs, **Region 3 - Severe wear region:** which ends with failure. In this region the cutting forces and temperatures are high accompanied by severe tool vibrations.

Crater wear occurs on the rake face of the tool and forms a crater. Severe pressure and temperature loads acting on the rake face causes diffusive wear of the chip material in cutting tool material on the rake face. Crater wear is temperature sensitive and depends on the tool material's solubility in the chip material. **Flank wear** is wear formed on the cutting tool's flanks. Abrasion of the clearance face against workpiece material causes flank wear. Li, Zhang and Wang investigated tool life and cutting forces in end milling operation of Inconel 718 using dry and MQL cutting conditions [30].

4. Techniques for enhancement of machining of Ti-6Al-4V

Various techniques to enhance machining efficiency of Ti-6Al-4V are summarized here. Most of the techniques make use of especial cooling or lubrication methods for temperature control and friction at the tool-workpiece interface.

- **Dry cutting:** Machining in the absence of lubrication. Cutting speed selection is very critical as absence of cutting fluids causes rise in temperature (cutting), hasty tool wear and subsiding workpiece surface integrity [32].

- **Flood cooling:** The technique uses inoculation of ionized gas and ozone molecules in the cutting zone, which is ecological, low-cost and has proven itself to reduce tool wear and improve tool life [33].

- **Minimum quantity lubrication:** In this technique, a small amount of lubricant is directed to the cutting edge, which reduces the temperature, surface roughness and cost. The usage of vegetable oil is better in terms of safety, health, cost and environment [31].

- **Water vapor:** Usage of water vapor is environmentally compatible, economical, and healthy but it reduces cutting force and tool life. Removal of heat is 2.5 times faster compared to oil [29, 31].

- **Cryogenic cooling:** Liquid nitrogen is used as a lubricant under pressure and at low temperature. The technique improves tool life and it is clean and non-polluting even at higher feed rates [40].

- **Solid lubricants:** Molybdenum disulphide and graphite are the most commonly used solid lubricants. At higher cutting speeds, solid lubricants perform better. These lubricants results in lower environmental pollution and have the capacity to lower the cutting temperature.

- **Hot machining:** In this practice, a pre-heated workpiece is used to minimalize the force requirement and to improve surface finish and tool life. High frequency induction, laser beam, and other techniques are used for pre–heating [34].

- **Rotary tooling:** In this case a round insert keeps revolving about itself and is driven externally by the cutting force effect simultaneously. Due to continuous rotation of the cutting edge, tool wear reduces as the position continuously changes [35].

- **Chip breaker:** Chips are broken into minor pieces by the use of inserts having chip breaking geometries or by adopting other methods like oscillating CNC toolpaths, facilitates its handling and evacuation.

- **Ramping:** In this technique, the tool-workpiece are continuous shifted to change the respective contact length, results in wear distribution on a larger area and, hence prevents notch wear.

5. Summary/Conclusion

Ti-6Al-4V alloy is extensively used in various engineering and biomedical applications. After reviewing the literature, experimental results and predicted models on machining of Ti-6Al-4V, the following conclusions are drawn;

- The low thermal conductivity of Ti-6Al-4V alloys results in an accumulation of heat at the tool-workpiece interface which accelerates tool wear and adversely affect economy of machining. To machine Ti-6Al-4V conventionally, low cutting speeds, high feed rates, a huge quantity of cutting fluids, sharp tools and a rigid set-up are essential.

- Advanced tool materials like PCD or CBN can be used for machining Ti-6Al-4V alloy at high cutting speeds but their life is limited by generation of extremely high temperature and stresses.

- Coated carbide cutting tool, high-pressure spindle lubrication system or ledge tool might be used to improve machinability. Performance of a Ti-Al-N coated carbide-cutting tool for hybrid machining at all cutting speeds is 2–3 times better than an uncoated carbide tool.

- Rigid clamping is necessary to avoid the effect of low elastic modulus of titanium alloy to result in chatter free surfaces.

- Electric discharge machining can be used as a machining process as it is proficient of machining all materials (electrically conductive) regardless of their hardness as in the process the electrode and workpiece do not come into direct contact, which eliminates the mechanical residual stresses and chatter or vibration problems during the machining.

- The material removal rate achieved while using combination of electric discharge machining (EDM) and ultrasonic machining (USM) process is higher than the conventional EDM and hence there is good potential to increase the machining efficiency.

- Economic analysis showed that use of Laser Assisted Machining or hybrid process with a coated tool (TiAlN) could yield a 30–40% saving in overall machining costs [38].

- Future work may be directed towards use of newer blends and methods of application of lubricants, design of new tools, use of non-traditional machining methods like Laser Assisted Machining or Electric Discharge Machining for sustainable machining of titanium alloys.

Author details

Ayanesh Y. Joshi[1*] and Anand Y. Joshi[2]

1 Mechanical Engineering Department, A. D. Patel Institute of Technology, Karamsad, Gujarat, India

2 Mechatronics Engineering Department, G. H. Patel College of Engineering and Technology, Gujarat, India

*Address all correspondence to: ayjoshi@adit.ac.in

References

[1] Machado AR, Wallbank J. Machining of titanium and its alloys–A review. Journal of Engineering Manufacturing. Proceedings of the Institution of Mechanical Engineers. Vol. 204

[2] Ezugwu EO, Wang ZM. Titanium alloys and their machinability–A review. Journal of Materials Processing Technology. August 1997;**68**(3):262-274

[3] Hayes FH, Bomberger HB, Froes FH, Kaufman L, Butte HM. Journal of Materials. Advances in Titanium Extraction Metallurgy. June 1984;**36**(6): 70-76

[4] Lin YC, Yan BH, Ch YS. Machining characteristics of titanium alloy (Ti±6Al±4V) using a combination process of EDM with USM. Journal of Materials Processing Technology. 2000; **104**:171-177

[5] van Kann H. Titanium and Titanium Alloys. Vol. I. New York, USA: Plenum Press; 1982. p. 229 T4

[6] Siekmann HJ. How to machine titanium. Tool Engineering. 1955;**34**: 78-82

[7] Hong H, Riga AT, Cahoon JM, Scott CG. Machinability of steels and titanium alloys under lubrication, Wear of Materials: Proceedings of the 9th International Conference. Vols. 162–164, Part A, 13 April 1993, 34-39

[8] Specifications and Properties of Titanium Alloy, Titanium Alloy Guide. Niles, OH: RMI Titanium Co., 2000

[9] Titanium Machining Guide, Kennametal. Fort Mill: MacMillan Park Drive. A18-A23

[10] Duncan RM, Blenkinsop PA, Goosey RE. Titanium Alloys. In: Meetham GW, editor. The Development of Gas Turbine Materials. Dordrecht: Springer. 1981. pp. 63-87

[11] Eylon D, Fulishiro S, Postans PJ, Froes FH. High-temperature titanium alloys—A review. Journal of Mechanical Engineering and Technology. 1984; **36**(11):55-62

[12] Ginting A, Nouari M. Surface integrity of dry machined titanium alloys. International Journal of Machine Tools and Manufacture. 2009;**68**:262-272

[13] Che-Haron CH. Tool life and surface integrity in turning titanium alloy. Journal of Materials Processing Technology. 2001;**118**:231-237

[14] Donachie JM. A Handbook on Titanium: A Technical Guide. Metals Park, OH: ASM international; 1988. ISBN: 0-87170-686-5

[15] Bridges PJ, Magnus B. Manufacture of Titanium Alloy Components for Aerospace and Military Applications. France: Research and Technology Organization; 2001

[16] Zhanga XP, Shivpurib R, Srivastavac AK. Role of phase transformation in chip segmentation during high speed machining of dual phase titanium alloys. Journal of Materials Processing Technology. 2014;**214**:3048-3066

[17] Rahman M, Wong YS, Zareena AR. Machinability of Titanium Alloys. JSME International Journal. 2003;**469**(1): 107-115

[18] Arrazolaa P-J, Garay A, Iriarte L-M, Armendia M, Maryab S, Le Maître F. Machinability of titanium alloys (Tie6Al4V and Ti555.3). Journal of Materials Processing Technology. 2009; **209**:2223-2230

[19] Veiga C, Davim JP, Loureiro AJR. Review on machinability of titanium alloys: The process perspective. Reviews On Advanced Materials Science. 2013; **34**:148-164

[20] Armendia M, Garay A, Iriarte L-M, Arrazola P-J. Comparison of the machinability of Ti6Al4V and TIMETAL®54M using uncoated WC-Co tools. Journal of Materials Processing Technology. 2010;**210**:197-203

[21] Barry J, Byrne G, Lennon D. A fast tool servo design for precision turning of shaft on conventional CNC laths. International Journal of Machine Tools and Manufacture. 2001;**41**:1055-1070

[22] Vyas A, Shaw M. Mechanics of saw-tooth chip formation in metal cutting. Journal of Manufacturing Science and Engineering;**121**(2):163-172

[23] Komanduri R, Hou Z-B. On thermoplastic shear instability in the machining of titanium alloy (Ti-6Al-4V). Metallurgical and Materials Transactions. 2002;**33**(9):2995-3010

[24] Gente A, Hoffmeister HW. Chip formation in machining Ti6Al4V at extremely high cutting speeds. CIRP Journal of Manufacturing Science and Technology. 2001;**50**:49-52. DOI: 10.1016/S0007-8506(07)62068-X

[25] Rahman M, Wang ZG, Wong YS. A review on high-speed machining of titanium alloys. JSME International Journal Series C. 2006;**49**(1):11-20

[26] Venkata Ramanaa M, Srinivasulub K, Krishna Mohana Rao G. Performance evaluation and selection of optimal parameters in turning of Ti-6Al-4V alloy under different cooling conditions. International Journal of Innovative Technology and Creative Engineering. 2011;**1**(5):10-21. ISSN: 2045-8711

[27] Deiaba I, Razaa SW, Pervaiza S. Analysis of lubrication strategies for sustainable machining during turning of titanium Ti-6Al-4V alloy. Procedia CIRP. 2014;**17**:766-771

[28] Muthukrishnan N, Davim P. Influence of coolant in machinability of titanium alloy (Ti-6Al-4V). Journal of Surface Engineered Materials and Advanced Technology. 2011;**1**(1) Article ID:4271

[29] Odelros S. Tool wear in titanium machining. ISSN: 1650-8297, UPTEC K12006

[30] Zhang S, Li JF, Wang YW. Tool life and cutting forces in end milling Inconel 718 under dry and minimum quantity cooling lubrication cutting conditions. Journal of Cleaner Production. 2012;**32**: 81-87

[31] Ahmad Yasir MS. Machinability of Ti-6Al-4V under dry and near dry condition using carbide tools. The Open Industrial and Manufacturing Engineering Journal. 2009;**2**:1-9

[32] Sharman A, Hughes J, Ridgway K. Surface integrity and tool life when turning Inconel 718 using ultra-high pressure and flood coolant system. Proceedings of the Institution of Mechanical Engineers, Part B: Journal of Engineering Manufacture. 2008;**222**:653

[33] Hossain M. Enhancement of machinability by workpiece preheating in end milling of Ti-6Al-4V. Journal of Achievements of Materials and Manufacturing Engineering. 2008;**31**:320

[34] Kishawy HA, Li L, El-Wahab AI. Prediction of chip flow direction during machining with self-propelled rotary tools. International Journal of Machine Tools and Manufacture. 2006;**46**:1680

[35] Sahu SK. Effect of groove-type chip breakers on twist drill performance. International Journal of Machine Tools and Manufacture. 2003;**43**:617

[36] Pawar M, Patil P, Pai JCS. Review on machining of titanium and alloys used in human implants/biomechanisms + aerospace industries. In: 2nd International Conference on Science, Technology and Management (ICSTM-2015). pp. 2903-2912

[37] Hascalık A, Caydas U. Electrical discharge machining of titanium alloy (Ti-6Al-4V). Applied Surface Science. 2007;**253**:9007-9016

[38] Dandekar CR, Shin YC, Barnes J. Machinability improvement of titanium alloy (Ti-6Al-4V) via LAM and hybrid machining. International Journal of Machine Tools and Manufacture. 2010; **50**:174-182

[39] Yang X, Richard Liu C. Machining titanium and its alloys. Machining Science and Technology. 1999;**3**(1): 107-139

[40] Joshi SS. Machinability of titanium alloys under various machining environments. In: International Conference and Exhibition on "Advances in Light weighting Technology–Design, Materials, Manufacturing Applications" 20-22 November 2012; Pune, India

Chapter

Dual Axis Solar Tracker

Smita B. Joshi and Neha D. Upadhyaya

Abstract

Solar energy, available nearly everywhere on the globe, is a good alternative for our day to day energy requirements. Harnessing solar energy requires techniques as it is a challenging task to move the solar module with the sun. The device that makes the movement of solar module according to sun's movement is known as a solar tracker. Generally, there are two types of solar trackers: (1) single axis solar tracker and (2) dual axis solar tracker. In this paper, we have used the dual axis solar tracker for comparison with stationary solar modules. A total of 20 solar modules, each of capacity 75 W, were tracked with a dual axis tracker system. The current and voltage were measured by varying rheostat. Current vs. voltage and power vs. voltage characteristics were studied with plotting the respective graphs. Nearly 30–35% power enhancement was observed with this dual axis tracking mechanism.

Keywords: efficiency, fill factor, maximum power point tracking, solar tracker

1. Introduction

The conventional energy sources are depleting very fast resulting in a crucial shortage of fuels. The high demand of fuel causes an increase in their price. It's time to switch over from conventional energy sources to nonconventional energy sources such as wind energy, tidal energy, solar energy etc. India is blessed with tremendous solar energy. Gujarat, Rajasthan, Tamil Nadu, Maharashtra states receive remarkable solar energy. Solar energy is clean, unpolluted, environment friendly and its conversion into electrical energy is highly promising. It needs very small maintenance and cleaning of the solar modules for more absorption of solar radiation. The solar cell cost is decreasing due to latest research in different materials and increasing their demand in global markets. Exponential increase of sales in this market with strong growth projection for the coming years is visibly reflected [1]. The conversion efficiency of almost all parts of the solar modules have increased up to 20% due to constant development of the technology but still it is not sufficient. Beltran and Stalter's continuous study in solar energy harnessing technology mentions several solutions to raise the conversion efficiency of solar PV modules. Tracking of solar PV modules on a single axis and dual axis [2, 3], optimizing the geometry of solar cell for increasing its packing density and thereby reducing the area required by the PV module have been tried by Morega et al. [4, 5]. In 1997, Jorgensen et al. [6] tried to enhance the light trapping capacity of the thin crystalline cells by utilization of thin structures on both the sides of wafer and Andreani et al. [7] used thin film silicon cells with photonic pattern. Basor used crystalline silicon on glass (CSG) with polycrystalline silicon technology that requires less than 2 microns thickness and discussed some of the difficulties faced in developing the new techniques [8]. Storage of electrical energy is very difficult but this problem was solved by using

an electrochemical cell. The novel material Cd_4GeSe_6 was tried by Turmezei [9]. The power produced by solar PV modules strongly depends on the incident light radiation which becomes maximum when the radiation is normal to the surface of PV module. This is attained by mounting the solar PV module on a solar tracking device which follows the trajectory of sun. The solar tracking systems, also known as sun tracker, automatically searches for the optimum PV module position by means of intelligent drive unit that receives input signals from dedicated light intensity sensors [10].

2. Assumptions for sizing PV systems

1. Precise estimation of solar radiation data:
   It is assumed that the solar radiation available at the location is 6000 W/m^2 per day. The system should be designed for the month of lowest radiation.

2. Sun-tracking of solar PV modules:
   Solar PV modules are considered fixed. Normally when modules are tracked to follow the sun, more energy can be generated using the same set of PV modules. Power enhancement is about 30% with the help of dual axis solar tracker but extra cost is required to implement the sun-tracking mechanism.

3. Ambient temperature in which modules and batteries are working:
   The ambient temperature affects the performance of the modules and batteries. The performance of the PV modules and batteries degrades as the ambient temperature increases above 25°C. Knowledge of the variation in ambient temperature over the year can be useful in estimating the real output from the PV modules and batteries.

4. Type of PV technology used in the system:
   The performance of the modules of different technologies (but same wattage) varies under the same operating conditions. For instance, a thin film module made up of amorphous Si performs better in cloudy conditions and early morning conditions than the module made up of crystalline Si wafers which is chosen.

5. Type of batteries used:

    1. Primary batteries: The primary batteries are non-rechargeable batteries. These batteries cannot be recharged once they have discharged and must be discarded.

    2. Secondary batteries: Secondary batteries are rechargeable batteries. These batteries can be charged and recharged several times.

3. Solar power plant with solar tracker

3.1 Solar power plant

A solar power plant with dual axis auto tracking system was designed, developed and installed at the terrace of our Department of Physics by technical officers. It can generate a maximum 1.5 kW of electrical power through 20 multi crystalline solar panels of 75 W generation capacity each. To improve the power generation capacity,

an indigenously designed and developed dual axis tracking system was attached to the plant [11].

3.2 Dual axis solar tracker

Figure 1 shows the dual axis tracking system which is uniquely designed on sensor based technology avoiding the need for manual programming from time to time. It can generate a maximum of 1.5 kW of electrical power through 20 multi crystalline solar panels of 75 W generation capacity each. The maximum power generated/day was approximately 6 kW out of which only 5 W was consumed by the tracker for automatic tracking mechanism. It was observed that there were maximum 3400 horizontal rotation and 700 vertical tilting of tracker. As the maximum base capacity of the tracker was of 3 kW, extra 20 panels each of capacity 75 W can be attached to double the power generation. The batteries connected in circuit stores the excess power which can be utilized during non-solar conditions. To study the increase of power generated in tracking mode, the test was repeated in fixed mode and tracking mode.

Initially, the tracker was tested in fixed position at the latitude angle of 22°E at Vallabh Vidyanagar, Gujarat, India. To study the increase of power generated in tracking mode, the test was repeated in tracking mode. **Figure 2** show fixing the angle of solar tracker with angle finder. **Figure 3** shows the junction box which is an essential part connected at the back of the solar module. There were two bypass diodes for 36 series connected cell in PV module. For calculation of efficiency of the PV module, both output power and input power were measured. The output power can be calculated by measuring voltage and current by voltmeter and ammeter respectively. The rated power of the multi crystalline SiN module is 75 W. Module efficiency is 11.6% which is less than the cell

Figure 1.
Dual axis solar tracker.

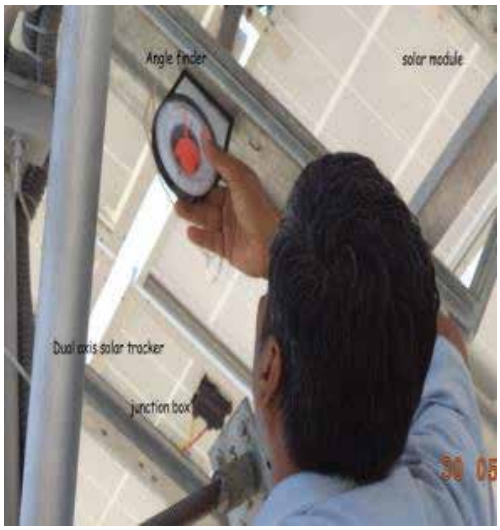

Figure 2.
Fixing the angle of tracker.

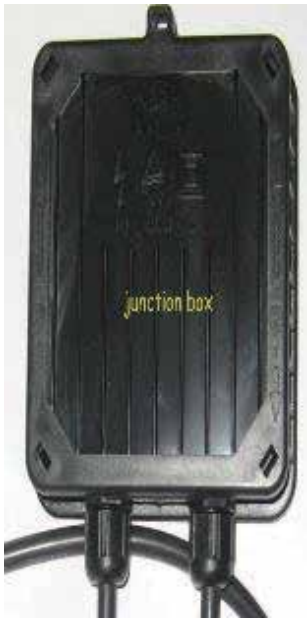

Figure 3.
Junction box.

efficiency 13.2%. This reduction of efficiency is due to deposition of unequal solar cells in module.

4. Results and discussions

4.1 Current voltage characteristics of solar module

To find out various current–voltage points of the PV module, resistances R of different values must be connected with the PV module. For such variable resistance requirement, a rheostat (200R, 2.5 A) was used. Before doing the connections,

the open circuit voltage (V_{OC}) is to be measured by connecting voltmeter across PV module's terminals (without connecting any load or rheostat). In the same manner, the short circuit current (I_{SC}) is to be measured by connecting ammeter in series with PV module (without connecting any load).

Current versus voltage characteristics were studied by connecting the rheostat to a low resistance value. For the lowest resistance value, current and voltage values were recorded. After that, the knob of rheostat was slightly moved and voltage and current were noted down for this new position. This was repeated until the highest value of resistance in rheostat was reached. The tabulated I-V points were plotted. Experimental set up is shown by **Figure 4**.

4.2 Maximum power point tracking (MPPT)

Figures 5 and **6** show the current-voltage and power-voltage characteristics of the solar module in the tracking mode condition respectively. It is observed that the maximum power P_m varies with time. The average power generated is 51.54 W.

Figure 4.
Experimental set up for I-V characteristics of solar module.

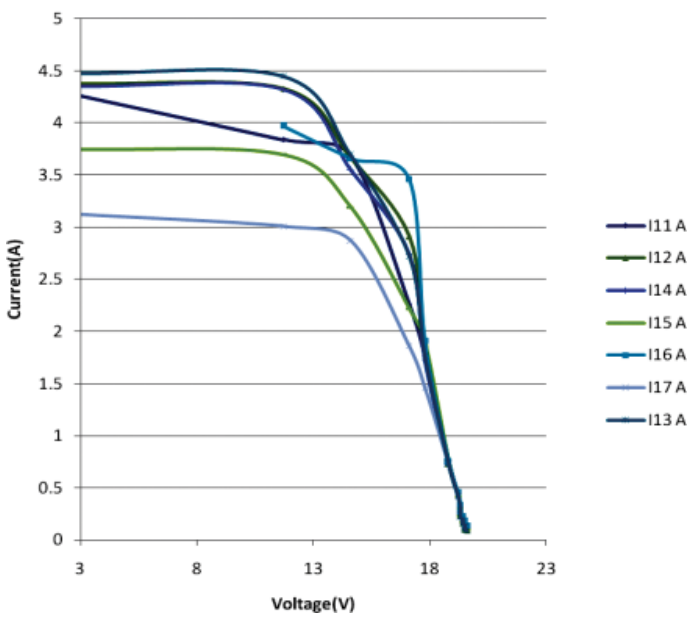

Figure 5.
I-V characteristics of PV module.

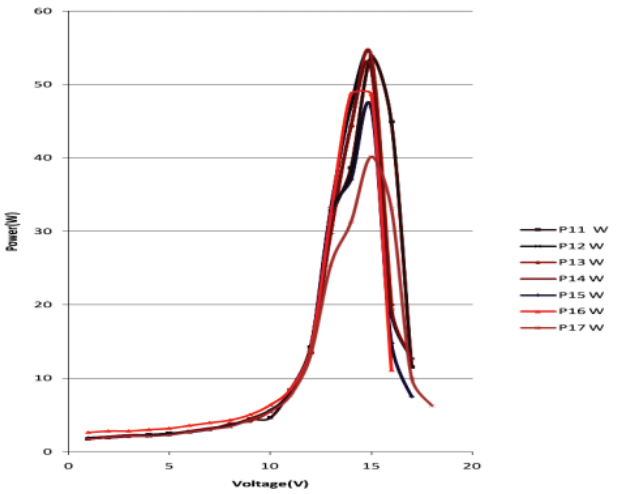

Figure 6.
P-V characteristics of PV module.

The three main parameters derived from the characteristics of current voltage and power voltage graphs are:

1. Open circuit voltage V_{OC}: The maximum voltage when the resistance is maximum (infinity). At this point, current becomes zero and as a result power also becomes zero.

2. Short circuit current I_{SC}: The maximum current when the resistance is minimum (zero). At this point, voltage becomes zero and hence power also becomes zero.

3. Maximum power point tracking (MPPT): When a solar PV module is used in a system, its operating point is decided by the load connected. Solar radiation falling on a PV module varies throughout the day, the operating point of module also changes throughout the day. In order to ensure the operation of PV modules, a special method called Maximum Power Point Tracking (MPPT) is employed in the PV system. It is based on the principle of independence matching between load and PV module.

The factors affecting electricity generated by solar PV module are conversion efficiency (η), amount of incident light, operating temperature, solar cell area and angle (θ) at which light falls.

It is the percentage of radiation input power converted into electrical power:

$$\eta = \frac{P_{\max}}{P_{in} \times A} \times 100 \qquad (1)$$

Where P_{in} = Input Power (W/m^2), η = efficiency (%), P_{max} = Maximum power (W), A = Area (m^2).

The insolation available for the month of January was between 800 and 900 W/m^2 during 10 am–3 pm. The power generated in tracking mode is more than 50 W throughout the day (11 am–5 pm) but for non-tracking mode, the power generated varies from 10 to 55 W. If the panel is kept in tracking mode, there is an increase in its efficiency.

5. Conclusions

When solar cells are mounted in a photovoltaic module, their efficiency decreases as the cells are not perfectly identical. The spacing between the cells is also one of the causes of reduction of efficiency as efficiency is inversely proportional to the area of the PV module. It is observed that the effective input power for tracking mode will be nearly constant with time and as a result of this the generated power also remains constant with time. The maximum power generated was 53.87 W while the minimum power was 46.89 W. Nearly 30–35% power enhancement was observed with this dual axis tracking mechanism.

Acknowledgements

The authors thank Dr. A R Jani for guidance and motivation and Shreelal Jha for technical support.

Author details

Smita B. Joshi[1*] and Neha D. Upadhyaya[2*]

1 Department of Applied Science and Humanities, G. H. Patel College of Engineering and Technology, Vallabh Vidyanagar, India

2 Department of Electronics and Communication, G. H. Patel College of Engineering and Technology, Vallabh Vidyanagar, India

*Address all correspondence to: smitajoshi@gcet.ac.in and nehajoshi@gcet.ac.in

References

[1] Tudorache T, Oancea CD, Kreindler L. Performance evaluation of a solar cooker with tracking PV panel. University "Politehnica" of Bucharest Scientific Bulletin, Series C: Electrical Engineering. 2012;**74**(1):425-430. ISSN 1454-234x

[2] Beltran JA, Gonzalez Rubio JLS, Garcia-Beltran CD. Design, manufacturing and performance test of a solar tracker made by an embedded control. In: CERMA; 2007; Mexico

[3] Stalter O, Burger B, Bacha S, Roye D. Integrated solar tracker positioning unit in distributed grid-feeding inverters for CPV power plants. In: ICIT; 2009; Australia

[4] Morega AM, Ordonez JC, Negoias PA, Hovsapian R. Spherical photovoltaic cells–A constructal approach to their optimization. In: OPTIM; 2006; Romania

[5] Morega AM, Bejan A. A constructal approach to the optimal design of photovoltaic cells. International Journal of Green Energy. 2005;**2**(3):233-242

[6] Jorgensen AM, Clausen T, Leistiko O. Novel light trapping scheme for thin crystalline cells utilizing deep structures on both wafer sides. In: Photovoltaic Specialists Conference; 1997; Anaheim, USA

[7] Andreani LC, Zanotto S, Liscidini M. Light trapping efficiency in thin-film silicon photovoltaic cells with a photonic pattern. In: 12th International Conference on Transparent Optical Networks (ICTON); 2010

[8] Basore PA. Manufacturing a new polycrystalline silicon PV technology. In: IEEE 4th World Conference on Photovoltaic Energy Conversion; 2006. pp. 2089-2093

[9] Turmezei P. Chalcogenide materials for solar energy conversion. Acta Polytechnica Hungarica. 2004;**1**(2):13-16

[10] Tudorache T, Kreindler L. Design of a solar tracker system for PV power plants. Acta Polytechnica Hungarica. 2010;**7**(1):23-39

[11] Joshi SB, Jani AR. Certain analysis of a solar cooker with dual axis sun tracker. In: 2013 Nirma University International Conference on Engineering (NUiCONE); Ahmedabad; 2013. pp. 1-5. DOI: 10.1109/NUiCONE.2013.6780150

Chapter

Prediction of Failure Using Forming Limit Curve in FE Analysis of Aluminium Alloy

Anand Dhruv and Gajjar Nilesh

Abstract

In sheet metal forming, the failure criteria is decided by the forming limit curve (FLC). The FLCs are mainly determined experimentally, but it is time consuming and not cost effective, and there are quite a few problems connected to such procedures. Therefore we need to produce FLCs using other methods. So discussed in this paper are some issues related to the use of the finite element method (FEM) for this purpose. This paper focuses on some procedures of limit strain prediction such as experimental methods, theoretical/analytical methods and FE-simulations. Herein the focus is on the use of the FEA. In the post processor of LS DYNA, the most widely used FEA package for metal forming analysis, the FLC is predicted by means of empirical correlation which depends on material properties such as strain hardening exponent (n) and sheet thickness (t). For verification and accuracy of the correlation, experimental tests were carried out for aluminium alloys for FLC.

Keywords: sheet metal, aluminium alloys, forming limit curve (FLC), finite element analysis (FEA)

1. Introduction

Sheet metal forming is a process in which flat thin blanks are deformed permanently to produce a wide range of products i.e. very simple sheet metal parts to complex three dimensional objects. Common parts made by sheet metal forming processes include automobile body panels, fuel tanks, aircraft parts and kitchen appliances, food and drink cans.

Aluminium alloys are now-a-days replacing the steel in the automobile industry since they have lower weight, comparable strength and high corrosion resistance and they reduce the vehicle weight and hence are able to achieve better fuel consumption [15–18]. Hence the formability of aluminium alloys needs to be studied.

The ability of a sheet metal to be formed in a given process without failure is known as formability. The understanding of formability is essential for successful forming of sheet metals into desired shape without any defects. The formability depends on different factors such as material properties such as ductility, ultimate tensile strength, anisotropy, die and punch design and process variables such as lubrication, blank holding force etc. As the effect

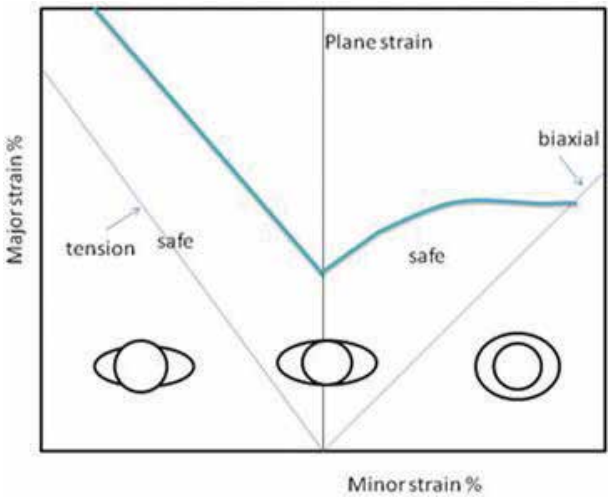

Figure 1.
Forming limit diagram.

of these parameters is complex, no single parameter can adequately measure formability [1–5].

Most of the formability tests give a rough indication of formability only in one single mode of deformation. The forming limit curve (FLC) (Keeler and Goodwin) is important for finding the limit stains where necking occurs in a sheet metal for all modes of deformation. Hecker in the 1960s developed some simplified techniques to evaluate the FLC. A typical FLC is shown in **Figure 1**. It is a pictorial representation of limit strains of a sheet metal which was subjected to different load paths, usually plotted as major principal engineering strain vs. minor principal engineering strain. The combination of major and minor strain points below this curve represents the safe region and this curve puts a limit up to which the forming operations can be done without necking or fracture [6–9].

2. Finite element analysis

In this research work, the finite element simulation has been carried out for the prediction of failure in stretch forming of aluminium alloys. The FE simulation was carried out in Dynaform 5.8, commercially available dedicated software meant for metal forming applications. It contained the preprocessing (auto generated meshing, tool arrangements, draw bead location) and post processing factors (animation, forming limit plot, deformation). The Dynaform uses LS DYNA (it is an explicit time integrating dynamic solver) in conjunction with the preprocessor and the LS-POST post processor.

Die diameter	Hemispherical botto punch diameter	Blank holder diameter	Die corner radius	Drawbead diameter	Blank thickness
104 mm	101.6 mm	255 mm	10 mm	132 mm	1.6 mm

Table 1.
Design parameters for stretch forming.

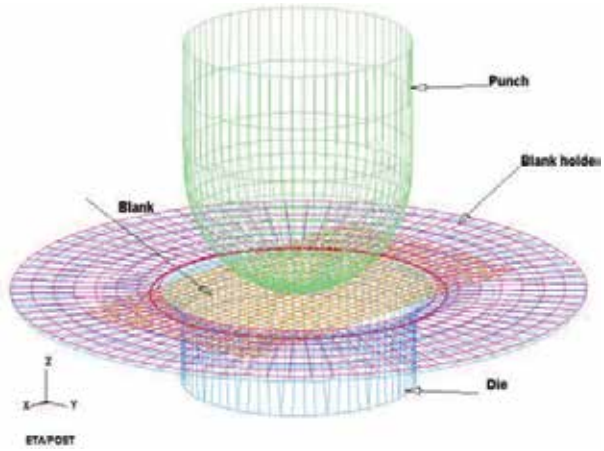

Figure 2.
Tools and blank in FEA.

Grade	Thickness	YS (MPa)	UTS (MPa)	n	K	R
AA-2024	1.6 mm	78	173	0.353	422	0.501

Table 2.
Material properties data.

Punch travel	Punch speed	Coefficient of friction	Blank holding force
40 mm	1000 mm/sec	0.125	15,000 N

Table 3.
Process parameter data.

The stretch forming was carried out using a 101.6 mm hemispherical diameter punch. The design parameters are given in **Table 1**. The blanks used are 175 mm × 175 mm, 175 mm × 100 mm and a modified blank design of 25 mm width which ensures all modes of deformations, such as biaxial stretching, plain strain and compression-tension region.

All tools were considered to be rigid bodies and the blank was taken as a deformable body and it has been meshed as quadrilateral shell elements. The default shell element formulation is BELYTSCHKO-TSAY, it is generally used in similar simulations. Draw bead is defined as line bead and was locked at the die. The 'forming-one-way' type contact interface is used for defining the contact. The arrangement of meshed tools and blank is shown in **Figure 2**.

The details of material properties and process parameters required for simulation were experimentally carried out and are shown in **Tables 2** and **3** respectively.

3. Simulation results

As shown in **Figure 3**, the simulation results of the stretch forming for different blank sizes width varied from 175 to 25 mm. The forming limit diagram and the failure is predicted based on the correlation already presented in the post processor of LS DYNA.

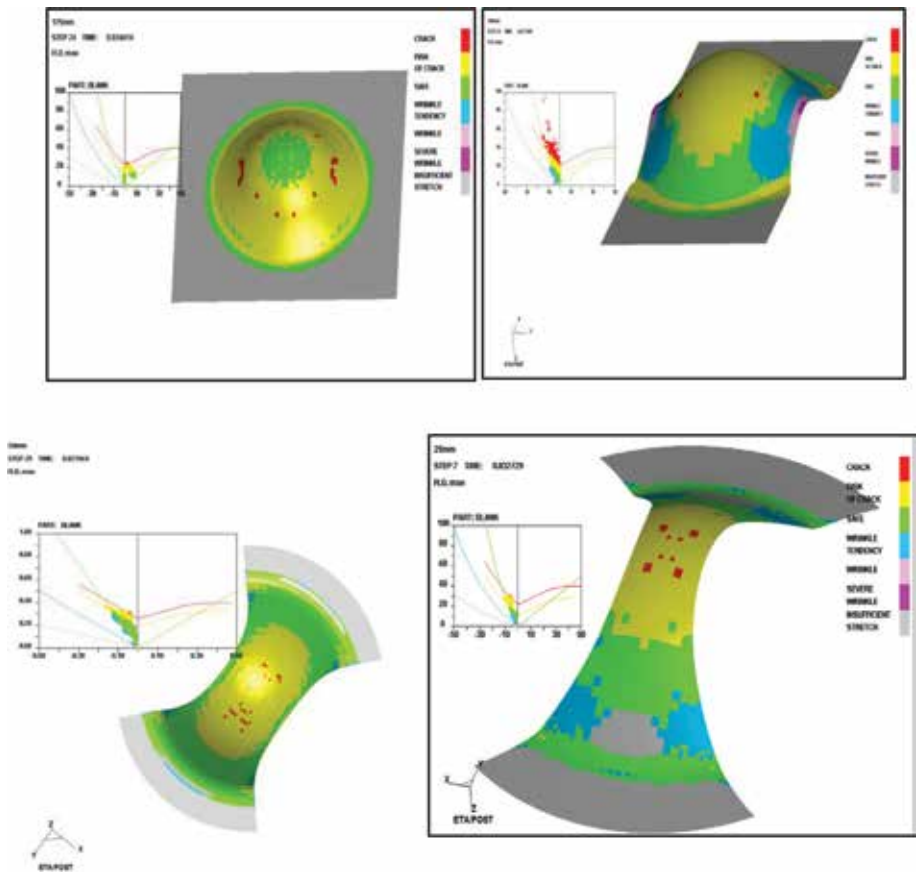

Figure 3.
Simulation results of stretch forming from different blank widths.

4. Experimental determination of forming limit diagrams

As suggested by Hecker [6], samples of varying width were deformed using a 101.6 mm hemispherical punch. The width was varied to obtain all possible deformation modes i.e. biaxial, plane strain condition and compression-tension. The schematic diagram of the arrangements of tools used in experiments is shown in **Figure 4**.

Samples of different width varying from 100 to 175 mm with constant length (175 mm) and a hourglass shaped specimen with widths having 25, 50 and 75 mm were prepared for punch stretching experiments (**Figure 5**). These blanks were cut with length perpendicular to the rolling direction. These metal blanks were laser marked with 5 mm diameter circles. These grid-marked specimens were deformed with a hydraulic press of 100-tonne capacity having double action. The LDH tests on samples of different widths were done on the hydraulic press using the experimental setup. The experiment was not continued when a visible necking or fracture was obtained on the samples, deformed specimen are shown in **Figure 5**.

Major strain and minor strains have been calculated by calculating major and minor length of ellipses on the deformed samples. A travelling microscope having at least a count of 0.001 mm was used to calculate major and minor length of ellipses for strain calculations. The major strain and minor strains in the necking region were measured and FLCs were drawn such that strains at necking/fracture lie above

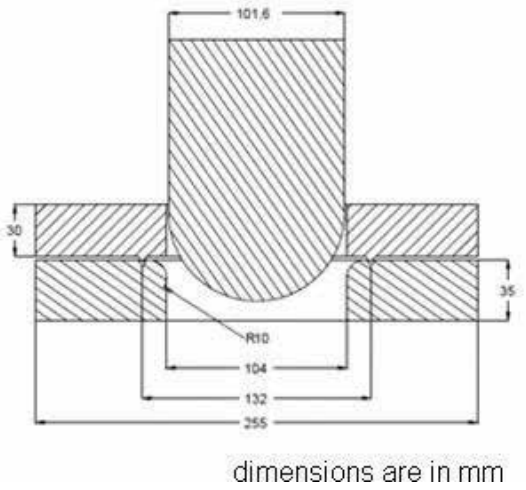

Figure 4.
Setup for LDH test.

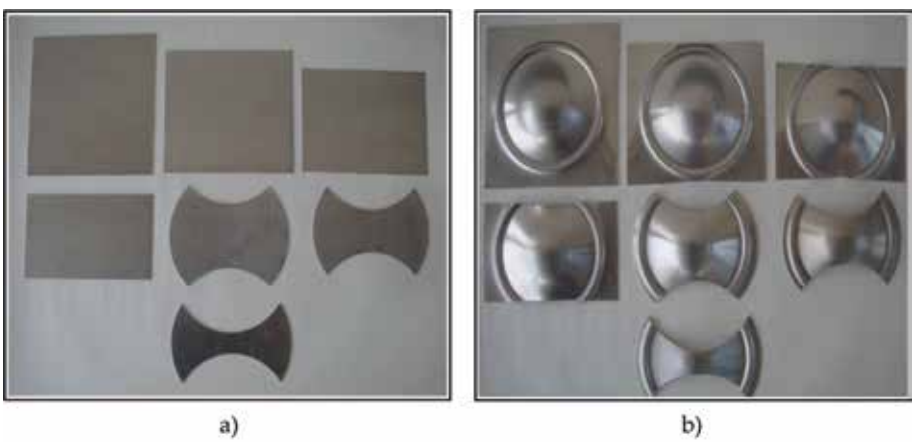

Figure 5.
Specimens before and after experiment. (a) Specimen before deformation and (b) specimen after deformation.

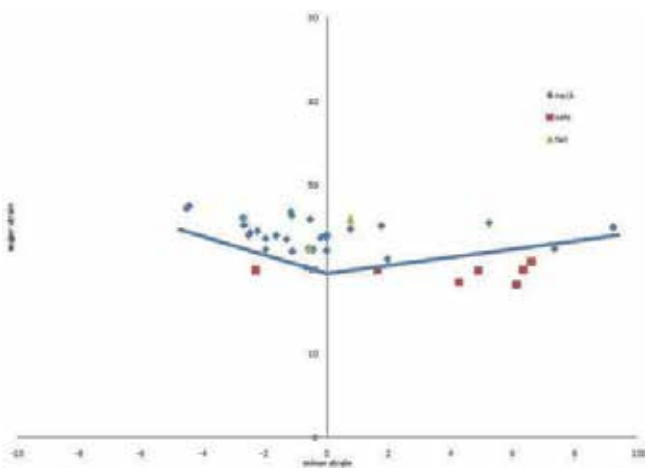

Figure 6.
Experimental forming limit diagram.

the line as shown in **Figure 6** [11–14]. The limited dome height (LDH) of all the samples at the point of necking was measured using a vernier height gauge.

5. Theoretical method for predicting the FLC using Sing and Rao's method

Sing and Rao [13] have proposed another method for predicting the FLC by means of tensile testing results. This method uses the material properties determined by simple tension.

The Sing and Rao method for developing the FLC was programmed in MATLAB. This method uses tensile properties like UTS, n, K and R for predicting the FLC.

Using the n value, the critical strain for localised neck was calculated by the equation:

$$\varepsilon_{1L} = 2n, \varepsilon_{2L} = 0 \tag{1}$$

The equivalent strain at this localised strain can be calculated using the equation:

$$\bar{\varepsilon} = \left[\left(\frac{1+R}{(1+2^{M-1}R)}\right)^{\frac{1}{(M-1)}}\left(|\varepsilon_1|^{\frac{M}{M-1}} + |\varepsilon_2|^{\frac{M}{M-1}}\right) + \left(\frac{1+R}{2}\right)^{\frac{1}{(M-1)}}\left(1-\left(\frac{1}{1+2^{m-1}R}\right)^{\frac{1}{m-1}}\right)\left(|\varepsilon_1+\varepsilon_2|^{\frac{M}{M-1}}\right)\right]^{\frac{M-1}{M}} \tag{2}$$

From the equivalent localised necking strain, the localised neck stress was determined with this equation:

$$\overline{\sigma L} = K(\bar{\varepsilon} L)^n \tag{3}$$

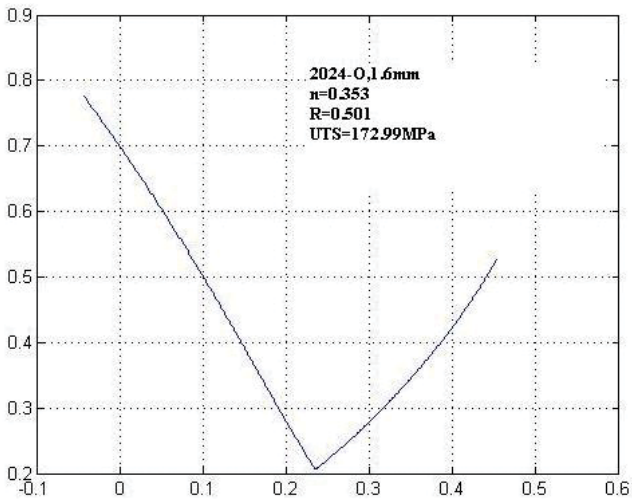

Figure 7.
FLC using Sing and Rao method.

The mechanical properties and the localised neck stress of the aluminium alloys were used for the Sing and Rao method.

From this, a limit yield stress curve was plotted using Hill's yield criterion.

$$\left(|\sigma_1^M| + |\sigma_2|^M\right) + \mathbf{R}|\sigma_1 - \sigma_2|^M = (\mathbf{1} + \mathbf{R})\,\bar{\sigma}^M \quad (4)$$

Using a linear regression method, this FLC was converted into a straight line (linear FLC). Depending on the material properties, the limit yield stress curve will change accordingly. The value of stress corresponding to each point on the linear FLC can be calculated by the equation. FLC is shown in **Figure 7**.

6. Comparison of different methods for predicting FLCs

A comparison of the FLCs of simulation, experimental and Sing and Rao method is shown in **Figure 8**. It is clear that the FLC generated from the post processor using the existing correlations predicts the FLC much higher as compared to the actual experimental FLC.

The FLCs predicted by Sing and Rao's method are compared with the FLCs predicted with the developed correlation and with the experimentally determined FLC. The minimum value of major strain did not appear exactly at the plain strain condition i.e. at FLC_0. Using this method, limit strains with higher negative minor strains could not be predicted due to nature of the yield locus and the material properties. **Figure 7**, it is seen that the Sing and Rao method also overestimates the limit strains compared to the experimental curve and in most cases, the FLCs generated by the developed correlation are closer to the experimental curves.

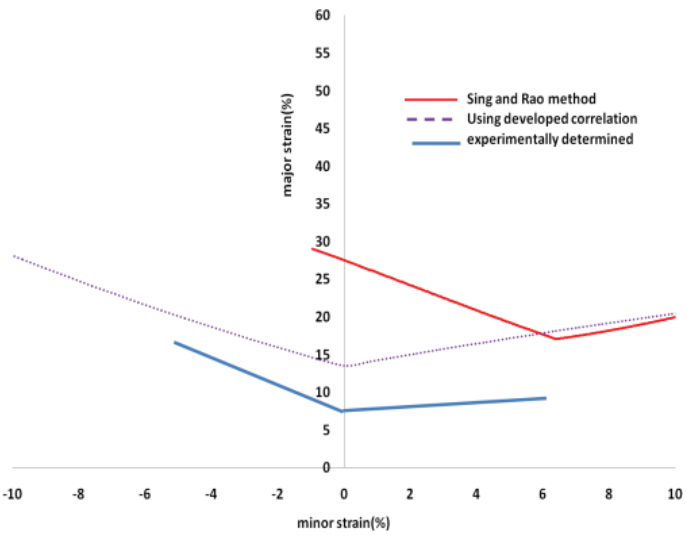

Figure 8.
Comparision FLC different methods.

7. Conclusions

The following conclusions are drawn:

1. FLCs generated from the post processor using the existing correlations predict much higher limit strains when compared to the actual experimental FLC.

2. The theoretical model proposed by Sing and Rao's method with tensile properties as the input has also been used to predict FLC and it has been found that this method also overestimates the limit strains.

3. The FLCs generated in the post processor with the above developed correlation are much closer to the experimental curves. So, FEA tool can be used for predicting the failure.

Author details

Anand Dhruv[1*] and Gajjar Nilesh[2]

1 Department of Mechanical Engineering, Vishwakarma Government Engineering College, Ahmedabad, India

2 Department of Mechanical Engineering, L&T Baroda, India

*Address all correspondence to: dhruv_30@rediffmail.com

References

[1] Barlat F, Lian J. Plastic behavior and stretchability of sheet metals. Part I: A yield function for orthotropic sheets under plane stress conditions. International Journal of Plasticity. 1989;**5**:51-56

[2] Charca Ramos G, Stout M, Bolmaro RE, Signorelli JW, Serenelli M, Bertinetti MA, et al. Study of a drawing-quality sheet steel. II: Forming-limit curves by experiments and micromechanical simulations. International Journal of Solids and Structures. 2010;**47**:5-10

[3] Stachowicz F. Formability of aluminium alloy sheets. Journal of Mechanical Working Technology. 1986;**13**:229-235

[4] Budinski KG, Bidinski MK. Engineering materials properties and selection. New Delhi: Prentice-Hall of India; 2002

[5] Dieter GE. Mechanical Metallurgy. Singapore: McGraw Hill; 1998

[6] Hecker SS. A cup test for assessing stretchability. Metals Engineering Quart. 1974;**14**:30-36

[7] Keeler SP. Understanding sheet-metal formability, Sheet Metal Industries. 1971;**48**:5-10

[8] Mahmudi R. Post- uniform deformation in uni-axial and equi-biaxial stretching of aluminium alloy sheets. Journal of Material Processing Technology. 1997;**70**:93-98

[9] Marciniak Z, Duncan JL, Hu SJ. Mechanics of Sheet Metal Forming. 2nd ed. London: Butterworth-Heinemann; 2002

[10] Narasimhan K, Miles MP, Wagoner RH. A better sheet-formability test. Journal of Materials Processing Technology. 1995;**50**:385-394

[11] Narayanasamy R, Satheesh J, Sathiya Narayanan C. Effect of annealing on combined forming, fracture and wrinkling limit diagram of aluminium 5086 alloy sheets. International Journal of Mechanics and Materials in Design. 2008;**4**:31-43

[12] Ravi Kumar D. Formability analysis of extra-deep drawing steel. Journal of Materials Processing Technology. 2002;**130-131**:31-41

[13] Sing WM, Rao KP. Prediction of sheet metal formability by tensile test results. Journal of Materials Processing Technology. 1993;**37**:37-51

[14] Smith PE, Lee D. Proc. International Body Engineering Conference. Detroit, MI: SAE; 1998. pp. 121-128

[15] Srivatsan TS, Kolar D, Magnusen P. The cyclic fatigue and final fracture behavior of aluminum alloy 2524. Materials & Design. 2002;**23**(2):129-139

[16] Staley JT, Lege DJ. Advances in aluminium alloys products for structural applications in transportation. Colloque C7, Supplement au Journal de Physique III. 1993;**3**:12-18

[17] Holmberg S, Enquist B, Thilderkvist P. Evaluation of sheet metal formability by tensile tests. Journal of Materials Processing Technology. 2004;**145**:72-83

[18] Yu Z, Lin Z, Zhao Y. Evaluation of fracture limit in automotive aluminium alloy sheet forming. Materials and Design. 2007;**28**:203-207

Chapter

Triple-Walled Carbon Nanotube for Strain Sensing

Minesh Patel, Anand Joshi and Ajay Patel

Abstract

This manuscript deals with the triple-walled carbon nanotube used for strain sensing at the nanolevel. The strain sensing occurs because of the shift of resonant frequency due to external loading on the pre-strained resonator. In the present work, the strain effect on triple-walled carbon nanotubes of different lengths and diameters are investigated under various conditions. The sensitivity of these sensors are improved with the decrease of tube length, while the key recurrence is upgraded with the expansion of tube distance across, in the case of axial strain sensing. The effect on the frequency is not significant with variation in the middle and outer wall length. The triple-walled carbon nanotube of the same length has higher frequency for bridge boundary condition when compared to the cantilevered boundary condition, so bridge boundary condition triple-walled carbon nanotube is more favorable for strain sensing.

Keywords: triple-walled carbon nanotubes, finite element method, strain, vibration, frequency

1. Introduction

Strain sensors have a broad range of applications in engineering, manufacturing and for measuring various quantities, such as stress, pressure, torque and vibration. Regardless of its exceptional characteristics, it has many limitations that consider traditional stress sensors like semiconductor and metallic stress gauge, measurement limits, low sensitivity, difficulties embedded in material structures, reduced fatigue life and sensitivity to environmental conditions. These limits have increased the demands for using innovative smart materials, e.g. silicon [1], nanoparticles [2–4], nanowires [5, 6], graphene [7–9] and carbon nanotubes (CNTs) [10–15].

Carbon nanotubes offer limitless opportunities as high frequency mechanical resonators for a number of applications. Nanotubes are ultralight, which is ideal for ultralow mass detection and ultrasensitive force detection [16, 17]. CNTs are potential contenders for a nanobeam-based strain sensor because of their optimal surface and vast viewpoint proportion. What's more, inferable from their high solidness-to-weight proportion, the ultra-affectability of CNTs additionally prompts an express data about strain by estimating the recurrence movement [18]. Li and Chou [19] have figured the key recurrence movement of CNTs with connected strain and weight in view of a continuum auxiliary mechanics demonstration. Their outcomes demonstrate that the vibrational recurrence diminishes with expanding pivotal strain in a SWCNT, which contradicts the experiments of Sazonova et al.

[20]. Truly, as indicated by the hypothesis of continuum vibration [21], when a strain is connected in a beam or string, one ought to expect a significant increase of vibrational recurrence. Patel and Joshi [22–27] have investigated the influence of resonant frequency of double-walled carbon nanotubes with mass sensing, surface deviation, atomic vacancy defect and pinhole defect. Patel et al. [28] have analyzed variation of mass attached on external walled of TWCNT.

2. Modeling of triple-walled carbon nanotubes

In this study, the continuum mechanics method is employed. For a TWCNT, a shell model is assumed such that each of the nested tubes is a specific shell and coupled with adjacent tubes through Van der Waals interaction. Strain analysis of TWCNTs is carried out using spring elements which are modeled as an interlayer interaction of the nanotube to designate the Van der Waals potential. The current model is simulated by taking into account the effective wall thickness of tubes and Van der Waals interaction between various carbon nanotubes to find the results. A cantilever boundary condition is considered for the simulation purpose.

3. Finite element procedure

Initial strain i.e. strain which is independent of stress, may be due to several causes, shrinkage, crystal growth, or most frequently temperature changes will result in an initial strain vector. All the effects of initial strains or stresses are incorporated in the nodal force vectors or nodal load vectors and it does not change the stiffness matrix.

The total potential energy is sum of energy due to bond expanse interaction, energy due to bending, the energy due to dihedral angle torsion, energy due to out-of-plane torsion and energy due to non-bonded Van der Waals interaction. It is shown in Eq. (1).

$$U_{Total} = \sum U_r + \sum U_\theta + \sum U_\varnothing + \sum U_\omega + \sum U_{vdw} \tag{1}$$

For bond systems, the key contributions to the whole static energy come from the first four expressions of Eq. (1). Under the statement of small deformation, the harmonic approximation is adequate for describing the energy [29]. The terminologies for each form of energy is defined by,

$$U_r = \frac{1}{2}k_r(r - r_0)^2 = \frac{1}{2}k_r(\Delta r)^2 \tag{2}$$

$$U_\theta = \frac{1}{2}k_\theta(\theta - \theta_0)^2 = \frac{1}{2}k_\theta(\Delta\theta)^2 \tag{3}$$

$$U_\tau = U_\varnothing + U_\omega = \frac{1}{2}k_\tau(\Delta\varnothing)^2 \tag{4}$$

where, k_r, k_θ, and k_τ are the bond enlarging, bond twisting and torsional resistance force constants, respectively, while Δr, $\Delta\theta$ and $\Delta\varnothing$ represent bond enlarging or stretching increment, bond angle variant and angle deviation of bond twisting respectively.

The VdW potential is described the interlayer interaction. In the present paper, a number of concentric elastic cylindrical layers of SWCNTs are treated as TWCNTs.

$$U(R) = 4\varepsilon\left[\left(\frac{\rho}{R}\right)^{12} - \left(\frac{\rho}{R}\right)^{6}\right] \tag{5}$$

where R = atomic distance and $\varepsilon = 3.8655 \times 10^{-13}$ N nm and $\rho = 0.34$ nm, respectively. In order to calculate the vibration explanation of TWCNTs, equations are developed that describe the dynamics equilibrium of the finite element model. The group or element equation created by the global stiffness and mass matrices can be gathered. The equation becomes,

$$c_1(d_2 - d_1) = K_1 d_1 + M_1 \ddot{d}_1 \tag{6}$$

$$-c_1(d_2 - d_1) + c_2(d_3 - d_2) = K_2 d_2 + M_2 \ddot{d}_2 \tag{7}$$

$$c_3(d_3 - d_2) = K_3 d_3 + M_3 \ddot{d}_3 \tag{8}$$

where M_i are mass matrices and k_i are stiffness matrices. $d_1 = Y_1 e^{iwt}$, $d_2 = Y_2 e^{iwt}$, $d_3 = Y_3 e^{iwt}$.

Further, the same can be represented as:

$$\begin{pmatrix} c_1 + K_1 & -c_1 & 0 \\ -c_1 & c_1 + c_2 + K_2 & -c_2 \\ 0 & -c_2 & c_2 + K_3 \end{pmatrix} \begin{pmatrix} Y1 \\ Y2 \\ Y3 \end{pmatrix} - \omega_n{}^2 \begin{pmatrix} M_1 & 0 & 0 \\ 0 & M_2 & 0 \\ 0 & 0 & M_3 \end{pmatrix} = 0 \tag{9}$$

Figures 1 and **2** show schematic diagrams of cantilever and bridged TWCNTs, which represent a finite element model of TWCNT with the spring element.

To model the layer to layer interactions and describe the Van der Waals (VdW) potentials between carbon atoms on different layers using ANSYS, a spring element COMBIN40 is utilized. COMBIN40 is an assemblage of a spring-slider and damper in parallel, joined to a gap in series. The spring stiffness coefficient of Eqs. (2)–(4) are taken to be equal to $k_r = 6.52 \times 10^{-7}$ N nm^{-1}, $k_\theta = 8.76 \times 10^{-10}$ N nm rad^{-2} and $k_s = 2.78 \times 10^{-10}$ N nm rad^{-2} [30].

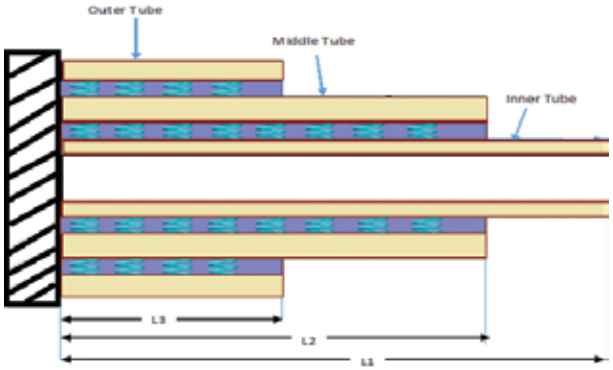

Figure 1.
Cantilevered TWCNTs.

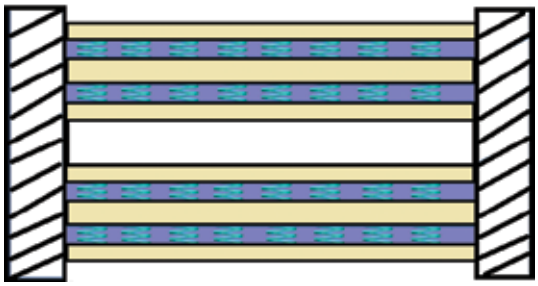

Figure 2.
Bridged TWCNTs.

4. Results

The models developed for the analysis has fixed free and bridged boundary conditions along with variation in initial strain and tube lengths (L3/L2/L1 = 1, L = 15,10,5). The inner tube radius R_1 = 0.65 nm, middle tube radius R_2 = 1.0 nm and outer tube radius R_3 = 1.35 nm. In **Figure 4**, the fundamental frequencies of TWCNTs as function of connected strain at nano level are shown. The fundamental frequencies as reported in **Table 1** are in gigahertz for the nanotube lengths. The shorter nanotubes often ascend to higher crucial frequencies. The principal frequency increases when the TWCNTs are subjected to a connected strain.

Strain (%)	**$L_3 = L_2 = L_1 = 15$ nm**	**$L_3 = L_2 = L_1 = 10$ nm**	**$L_3 = L_2 = L_1 = 5$ nm**
0.1	1.60E + 08	2.46E + 08	5.20E + 08
0.15	1.86E + 08	2.84E + 08	5.86E + 08
0.2	2.07E + 08	3.14E + 08	6.39E + 08
0.25	2.25E + 08	3.38E + 08	6.83E + 08
0.3	2.38E + 08	3.58E + 08	7.18E + 08

Table 1.
Frequency variation for cantilever CNTs with length ratio $L_3/L_2/L_1$ = 1.

Strain (%)	**Fundamental Frequency for cantilever TWCNT with different length ratio**			
	L_3/L_1 = 1/4, L_2/L_1 = 1/2	**L_3/L_1 = 1/3, L_2/L_1 = 2/3**	**L_3/L_1 = 1/2, L_2/L_1 = 3/4**	**L_3/L_1 = 1, L_2/L_1 = 1**
	Frequency (Hz)	**Frequency (Hz)**	**Frequency (Hz)**	**Frequency (Hz)**
0.1	2.11E + 08	2.13E + 08	2.12E + 08	1.60E + 08
0.15	2.47E + 08	2.49E + 08	2.46E + 08	1.86E + 08
0.2	2.75E + 08	2.77E + 08	2.74E + 08	2.07E + 08
0.25	2.97E + 08	2.99E + 08	2.96E + 08	2.25E + 08
0.3	3.15E + 08	3.17E + 08	3.13E + 08	2.38E + 08

Table 2.
Fundamental frequency for fixed-free and fixed-fixed TWCNTs with variable strain for dissimilar length ratio (outer, middle and inner tube radius respectively R_3 = 1.35, R_2 = 1.0, R_1 = 0.65).

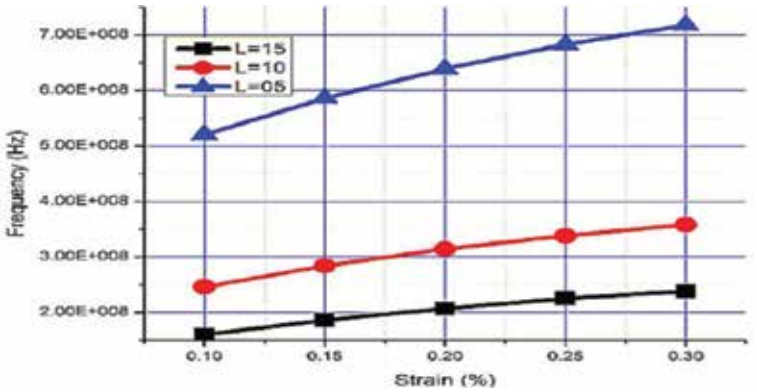

Figure 3.
Effect of applied initial axial strains.

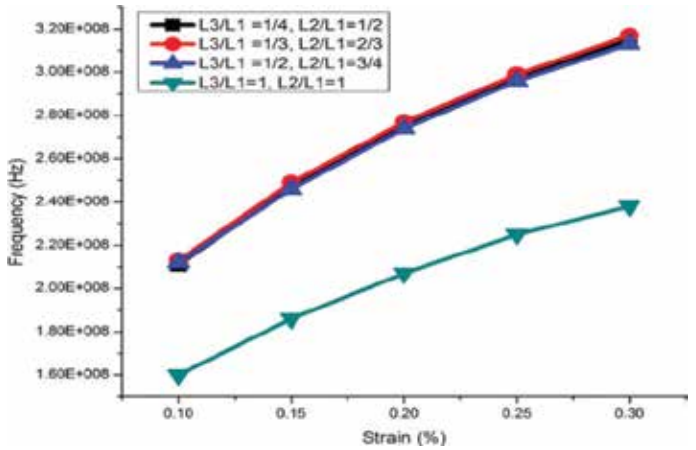

Figure 4.
Variation of fundamental frequency of TWCNT for various length ratio.

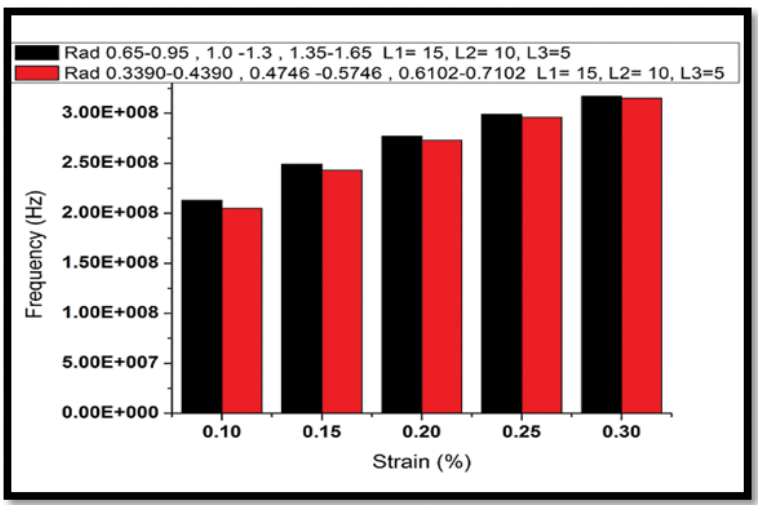

Figure 5.
Change in the frequency with different strains.

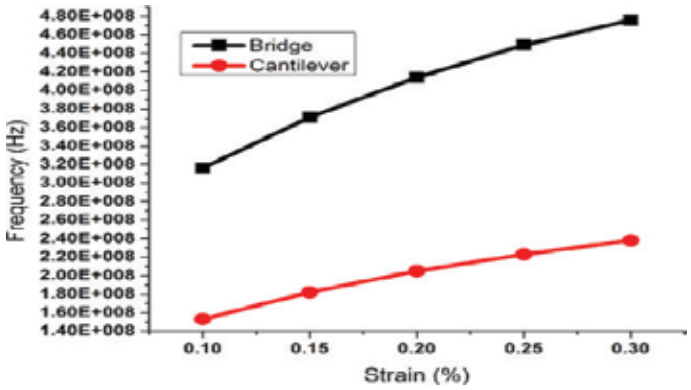

Figure 6.
Variation of fundamental frequency of Fixed-fixed & Fixed free TWCNTs for same length of tube.

Strain (%)	Frequency fixed-free TWCNT	Frequency fixed-fixed TWCNT
	L3/L2/L1 = 1	L3/L2/L1 = 1
	Frequency (Hz)	Frequency (Hz)
0.1	1.53E + 08	3.16E + 08
0.15	1.82E + 08	3.71E + 08
0.2	2.05E + 08	4.14E + 08
0.25	2.23E + 08	4.49E + 08
0.3	2.38E + 08	4.76E + 08

Table 3.
Frequency for fixed-free and fixed-fixed TWCNTs with dissimilar pre strain for L3/L2/L1 = 1 (Outer, Middle and Inner tube radius respectively R3 = 0.6102, R2 = 0.4746, R1 = 0.3390 nm).

A function of initial strain versus fundamental frequency with the variation in length ratio is shown in **Table 2**. For equal length of all tubes of TWCNTs, the impact of the length of nanotube in terms of change in strain is greater in shorter TWCNTs. The same has been depicted in **Figure 3**. The frequency of variable length TWCNT is higher compared to the equal length TWCNT. However, the variation in length ratio does not show any significant changes in frequency as shown in **Figure 4**.

Figure 5 shows the fundamental frequency versus strain. **Figure 6** depicts the variations in frequencies for different configurations with the same length of nanotube.

The model developed was analyzed for fixed free TWCNTs and bridged TWCNTs with the variation in initial strain and lengths L3/L2/L1 = 1, L = 15. The inner radius R_1 = 0.3390 nm of inner tube, middle tube radius R_2 = 0.4746 nm and outer tube radius R_3 = 0.6102 nm where R_1, R_2 and R_3 are the inner, middle and outer tube radius of the center line. In **Table 3** cantilever and bridge TWCNTs frequency variation versus initial strain is shown.

5. Conclusion

1. Strain sensitivity of TWCNT is enhanced with reduction in tube length for strain applied along the length.

2. With variation in length of the outer tube and middle tube, the fundamental frequency variation is less. So, it is less sensitive to outer and middle wall lengths changes on strain sensing, but when compared to equal length of all tubes, it gives higher fundamental frequency.

3. It clearly shows that the impact of nanotube length on the strain affectability is more prominent than that of tube diameter.

4. Resonant frequency of a TWCNT with bridge and fixed free boundary condition shows that bridge boundary condition is more favorable for strain sensing.

Author details

Minesh Patel[1], Anand Joshi[2] and Ajay Patel[2]

1 Mechanical Engineering Department, ITM Universe, Vadodara, Gujarat, India

2 Mechatronics Engineering Department, G. H. Patel College of Engineering and Technology, Gujarat, India

IntechOpen

References

[1] Kulha P, Boura A, Husak M. Design and fabrication of piezoresistive strain-gauges for harsh environment applications. In: Proceedings of the International Conference on Renewable Energies and Power Quality (ICREPQ), Granada, Spain; 2010 Mar. pp. 23-25

[2] Tanner JL, Mousadakos D, Giannakopoulos K, Skotadis E, Tsoukalas D. High strain sensitivity controlled by the surface density of platinum nanoparticles. Nanotechnology. 2012;**23**(28):285501

[3] Sangeetha NM, Decorde N, Viallet B, Viau G, Ressier L. Nanoparticle-based strain gauges fabricated by convective self assembly: Strain sensitivity and hysteresis with respect to nanoparticle sizes. The Journal of Physical Chemistry C. 2013;**117**(4):1935-1940

[4] Tanner JL, Mousadakos D, Broutas P, Chatzandroulis S, Raptis YS, Tsoukalas D. Nanoparticle strain sensor. Procedia Engineering. 2011;**25**:635-638

[5] Zhang W, Zhu R, Nguyen V, Yang R. Highly sensitive and flexible strain sensors based on vertical zinc oxide nanowire arrays. Sensors and Actuators A: Physical. 2014;**205**:164-169

[6] Wu JM, Chen CY, Zhang Y, Chen KH, Yang Y, Hu Y, et al. Ultrahigh sensitive piezotronic strain sensors based on a $ZnSnO_3$ nanowire/microwire. ACS Nano. 2012;**6**(5):4369-4374

[7] Wang B, Lee BK, Kwak MJ, Lee DW. Graphene/polydimethylsiloxane nanocomposite strain sensor. Review of Scientific Instruments. 2013;**84**(10):105005

[8] Tian H, Shu Y, Cui YL, Mi WT, Yang Y, Xie D, et al. Scalable fabrication of high-performance and flexible graphene strain sensors. Nanoscale. 2014;**6**(2):699-705

[9] Kuang J, Liu L, Gao Y, Zhou D, Chen Z, Han B, et al. A hierarchically structured graphene foam and its potential as a large-scale strain-gauge sensor. Nanoscale. 2013;**5**(24):12171-12177

[10] Kang I, Schulz MJ, Kim JH, Shanov V, Shi D. A carbon nanotube strain sensor for structural health monitoring. Smart Materials and Structures. 2006;**15**(3):737

[11] Yamada T, Hayamizu Y, Yamamoto Y, Yomogida Y, Izadi-Najafabadi A, Futaba DN, et al. A stretchable carbon nanotube strain sensor for human-motion detection. Nature Nanotechnology. 2011;**6**(5):296-301

[12] Zhang W, Suhr J, Koratkar N. Carbon nanotube/polycarbonate composites as multifunctional strain sensors. Journal of Nanoscience and Nanotechnology. 2006;**6**(4):960-964

[13] Müller C, Leonhardt A, Kutz MC, Büchner B, Reuther H. Growth aspects of iron-filled carbon nanotubes obtained by catalytic chemical vapor deposition of ferrocene. The Journal of Physical Chemistry C. 2009;**113**(7):2736-2740

[14] Stampfer C, Helbling T, Obergfell D, Schöberle B, Tripp MK, Jungen A, et al. Fabrication of single-walled carbon-nanotube-based pressure sensors. Nano Letters. 2006;**6**(2):233-237

[15] Iijima S. Helical microtubules of graphitic carbon. Nature. 1991; **354**(6348):56

[16] Poncharal P, Wang ZL, Ugarte D, De Heer WA. Electrostatic deflections and electromechanical resonances of carbon nanotubes. Science. 1999;**283**(5407):1513-1516

[17] Reulet B, Kasumov AY, Kociak M, Deblock R, Khodos II, Gorbatov YB,

et al. Acoustoelectric effects in carbon nanotubes. Physical Review Letters. 2000;**85**(13):2829

[18] Cao G, Chen X, Kysar JW. Strain sensing of carbon nanotubes: Numerical analysis of the vibrational frequency of deformed single-wall carbon nanotubes. Physical Review B. 2005;**72**(19):195412

[19] Li CY, Chou TW. Strain and pressure sensing using single-walled carbon nanotubes. Nanotechnology. 2004;**15**(11):1493

[20] Sazonova V, Yaish Y, Üstünel H, Roundy D, Arias TA, McEuen PL. A tunable carbon nanotube electromechanical oscillator. Nature. 2004;**431**(7006):284-287

[21] Rao Singiresu S. Mechanical Vibrations. Englewood Cliffs, NJ: Prentice-Hall; 2002

[22] Patel AM, Joshi AY. Influence of atomic vacancies on the dynamic characteristics of nanoresonators based on double walled carbon nanotube. Physica E. 2015;**70**:90-100

[23] Patel AM, Joshi AY. Evaluating the vibrational characteristics of double walled carbon nanotubes with pinhole defects. Current Nanoscience. 2015;**11**(3):371-378

[24] Patel AM, Joshi AY. A review on defects in carbon nanotubes. Applied Mechanics and Materials. 2015;**813-814**:145-150

[25] Patel AM, Joshi AY. Vibration analysis of double wall carbon nanotube based resonators for Zeptogram level mass recognition. Computational Materials Science. 2013;**79**:230-238

[26] Patel AM, Joshi AY. Investigating the influence of surface deviations in double walled carbon nanotube based nanomechanical sensors. Computational Materials Science. 2014;**89**:157-164

[27] Patel AM, Joshi AY. Investigation of double walled carbon nanotubes for mass sensing. Procedia Technology. 2014;**14**:290-294

[28] Patel MT, Patel AM, Joshi AY. Zeptogram mass detection using triple walled carbon nanotubes. Current Nanoscience. 2017;**13**:281-291

[29] Li C, Chou TW. Elastic moduli of multi-walled carbon nanotubes and the effect of van der Waals forces. Composites Science and Technology. 2003;**63**(11):1517-1524

[30] Cornell WD, Cieplak P, Bayly CI, Gould IR, Merz KM, Ferguson DM, et al. A second generation force field for the simulation of proteins, nucleic acids, and organic molecules. Journal of the American Chemical Society. 1995;**117**(19):5179-5197

Chapter

Analyzing Tactics and Reduction of Core Shift and Sand Drop for Crank Case 3000 Casting with Help of Quality Improvement Methods

R.S. Barot, M. Iyer, S. Pampaniya, J. Mori, H. Panchal, B. Sharma and J. Shah

Abstract

Quality is a standard requirement needed by foundries to survive in the market and rejection due to defects is the prime setback for such industries as it decreases the credibility of that specific industry. Depending on the type of foundry and other factors such as type of sand, casting material, molding methods, etc. there are specific defects that are more prominent than the others. It is observed in the industry that core shift and sand drop defects are the major reasons for most of the rejections of casted parts. Considering these facts, it is proposed that the generation of defects may involve single or multiple causes, hence it is studied through a systematic procedure using cause effect, Pareto analysis and Why-Why analysis of each and every defect existing in the product, which in turn helps to point out the root cause of the major defects. A study of sand parameters in relation to the defects gives the means of correction in the molding sand. Sand parameters include moisture, permeability, compactibility and green compressive strength. Analysis for core shift and sand drop was undertaken on the product Crank Case 3000 with the help of quality improvement methods.

Keywords: casting defect reduction, core shift, sand drop, DOE & ANOVA

1. Introduction

Sand drop and core shift are defects based on molding sand properties. Sand drops are inappropriately shaped crests that occur when the loose sand breaks away from the mold and falls into the cavity. Core shift occurs when the position of the core changes from the required place due to misalignment of cope and drag. These defects occur when the required strength of sand is inadequate. Dirty casting surfaces and inaccurate measurements of hollow parts in castings are causes of sand drop and core shift respectively.

2. Methodology

Solutions were obtained with the help of systematic execution of steps required for any problem-solving scenario. To obtain the remedies for core shift and sand drop using analysis tools, the following steps were carried out.

- Data collection of defects
- Data analysis by Pareto charts
- Cause effect diagram
- Why-Why analysis
- DOE
- ANOVA
- Process sigma calculation

3. Analysis for the product Crank Case 3000

Collection of the rejection data is essential for defect analysis. This helps us to understand which defect caused the most rejection. As stated earlier, the majority of the defects observed were core shift and sand drop by visual observation. To better understand these results, a bar chart needs to be prepared for the product that has significant rejections due to defects. In this case, from the entire range of products, Crank Case 3000 was used due to its high rejection rate (**Table 1**).

Furthermore, most of the rejection causes for the product were due to only two defects: sand drop and core shift as shown in the bar chart. Sand drop occurs due to misaligned cope and drag, which in turn also creates core shift. Weak green

Product: Crank Case 3000 casting			
	Defect types		
Month	**Core shift**	**Sand drop**	**Other defects**
April-16	5	2	3
May-16	0	7	2
Jun-16	0	22	10
Jul-16	7	23	1
Aug-16	0	7	7
Sep-16	35	2	1
Oct-16	8	10	6
Nov-16	4	8	5
Dec-16	6	3	6
Jan-16	24	17	10
Feb-16	0	5	6
Mar-16	8	8	0

Table 1.
Defect analysis table for product Crank Case 3000.

DOI: http://dx.doi.org/10.5772/intechopen.81083

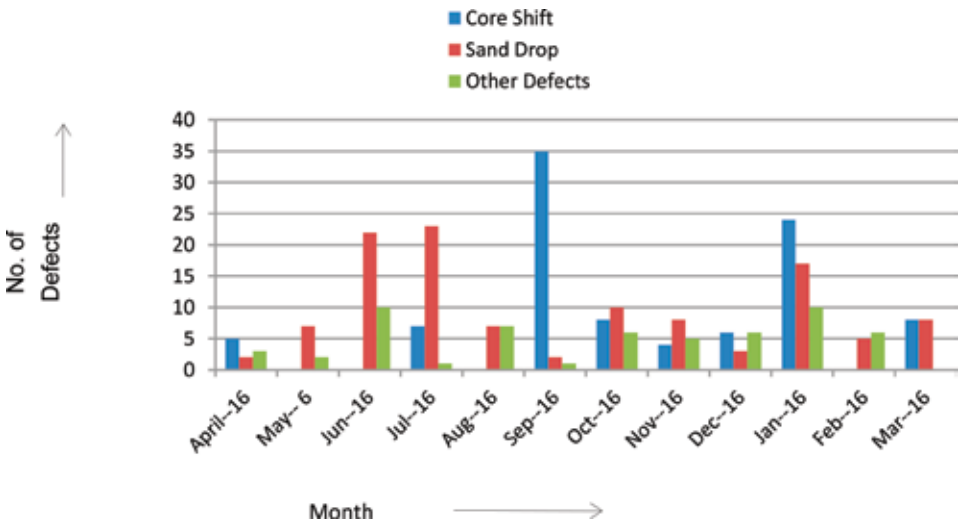

Figure 1.
Bar chart of defect analysis for product Crank Case 3000.

compressive strength and incorrect moisture levels also play a huge role in causing these defects (**Figure 1**).

4. Pareto analysis to find critical defects and their causes in product Crank Case 3000

From the preliminary analysis, it was decided that the two defects (core shift and sand drop) were to be studied further with the help of Pareto charts and cause

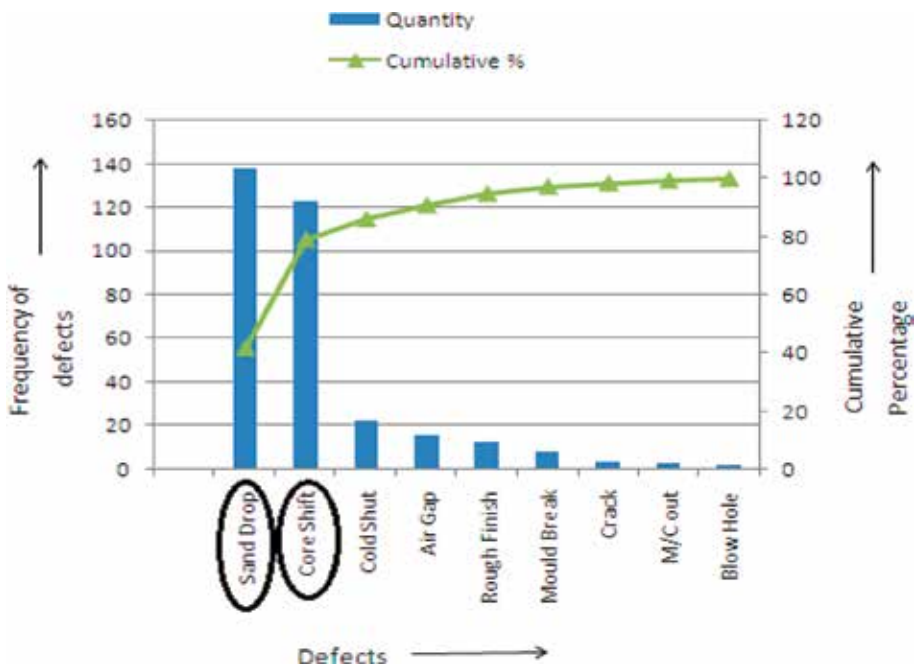

Figure 2.
Pareto chart for product Crank Case 3000 rejection.

effect diagrams to better understand the percentage of rejection and the root cause of the defects.

For this to occur, Pareto analysis was carried out. **Table 2** was created in preparation of the Pareto chart. A cumulative percentage of the defects was taken in descending order.

Pareto charts display the 80–20 rule, which means that 80% of the rejections are due to 20% of the causes. Here the causes are confirmed as core shift and sand drop. In **Figure 2**, it is clear that both core shift and sand drop are above the 80% limit. This shows that according to the 80–20 rule, these two defects are critically affecting the yield and efficiency of the product and foundry.

5. Cause effect diagram to find critical defects and their causes in product Crank Case 3000

Construction of the cause effect diagram was undertaken by considering the significant factors that affect both core shift and sand drop. All these factors are summarized under five basic categories namely Machine, Sand, Mold, Metal and Core. The critical control factors were chosen based on weighted scores obtained from observation of the defect analysis and their causes as shown in **Table 2**. The level of importance of the factor and the co-relation of the output with input is specified to calculate the weighted score.

After calculating the scores, the factors with maximum scores are highlighted in **Table 3**.

The score for correlation of the output with input is based on the following scale: 9 = very strong, 7 = strong, 5 = moderate, 3 = poor, 1 = very poor.

Comparing the above causes, one can observe that compactibility, green compressive strength (GCS), moisture and permeability directly affect the defect as they are related to the molding sand. The other causes are non-measurable and need to be solved by brainstorming (**Figure 3**).

When the GCS is low, the sand cannot be held together, which causes loose sand. Loose sand is a major reason for the sand drop defect. High permeability shows that the sand has many intermediate spaces that allow the gases to escape. Thus high permeability shows that the GCS is comparatively low.

Category	Quantity	Cumulative	Cumulative %
Sand drop	138	138	41.81
Core shift	123	261	79.09
Cold shut	23	284	86.06
Air gap	16	300	90.90
Rough finish	13	313	94.84
Mold break	8	321	97.27
Crack	4	325	98.48
M/C out	3	328	99.39
Blow hole	2	330	100
Total	330	—	—

Table 2.
Cumulative rejection analysis of product Crank Case 3000.

	Output parameters (Y)		
Process variables (X)	**Product quality (7)**	**Controlling of parameter (3)**	**Weightage score**
Improper sand	5	5	50
Misalignment	7	5	**64**
Bent clamping pins	7	5	**64**
Sand composition	7	5	**70**
Size distribution	3	5	36
Compactibility	9	7	**84**
GCS	9	7	**84**
Moisture	7	9	**70**
Permeability	9	7	**84**
Fluidity	3	1	24
Pouring time	1	5	21
Metal composition	1	1	10
Core composition	1	5	16
Cooling time	3	1	24
Pouring temperature	1	3	16
Core hardness	5	5	50

Table 3.
XY cause effect matrix for identifying control factors.

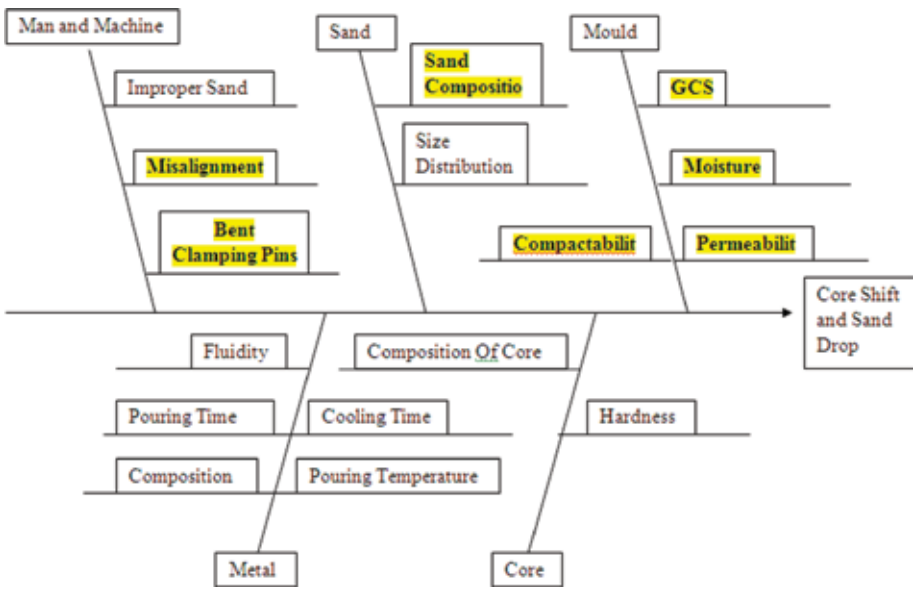

Figure 3.
Cause effect diagram for core shift and sand drop.

Also high compactibility shows low permeability, which can cause gas related defects. High moisture content can decrease the GCS beyond a certain range. Thus to completely prevent core shift and sand drop, a balance in values of these parameters is necessary.

6. Why-Why analysis

Any problem always has a cause that points out the core of the problem. The Why-Why analysis is a powerful statistical tool that helps us to find out the root cause of any non-measurable problem. With observation and asking the question "why" five times in a row, the root cause of the problem comes to light. With the help of this tool, the root cause analysis of core shift and sand drop was carried out and the outcome is as shown in **Figure 4**.

Observing the Why Why analysis, we can confirm that sand composition can be controlled by altering the values of the sand parameters. The change in GCS, moisture, permeability and compactibility is proposed to acquire various data for defects related to these sand parameters.

7. DOE and ANOVA

Core shift and sand drop are primarily molding sand-based defects. Changing the sand properties to optimum properties is one of the main requirements to reduce core shift and sand drop defects (**Table 4**).

DOE was carried out on compactibility, permeability, moisture content and green compressive strength. By application of DOE, an analysis can be made of how the factors vary with respect to each other.

$$\begin{aligned}\%\,\text{Reject} = {} & 1,522,604\text{–}1474\,\text{GCS} - 39,782\,\text{permeability} + 14,071\,\text{Compactibility} \\ & + 120,902\,\text{Moisture} - 0.00372\,\text{GCS}^2 - 1.796\,\text{Permeability}^2 \\ & - 34.1\,\text{Compactibility}^2 + 2995\,\text{Moisture}^2 + 38.19\,\text{GCS} \times \text{Permeability} \\ & - 10.8\,\text{GCS} \times \text{Compactibility} - 136\,\text{GCS} \times \text{Moisture} + 527\,\text{Permeability} \\ & \times \text{Compactibility} + 5320\,\text{Permeability} \times \text{Moisture} \\ & + 17,587\,\text{Compactibility} \times \text{Moisture} - 0.501\,\text{GCS} \times \text{Permeability} \\ & \times \text{Compactibility} - 5.06\,\text{GCS} \times \text{Permeability} \times \text{Moisture} \\ & + 16.70\,\text{GCS} \times \text{Compactibility} \times \text{Moisture}\end{aligned} \tag{1}$$

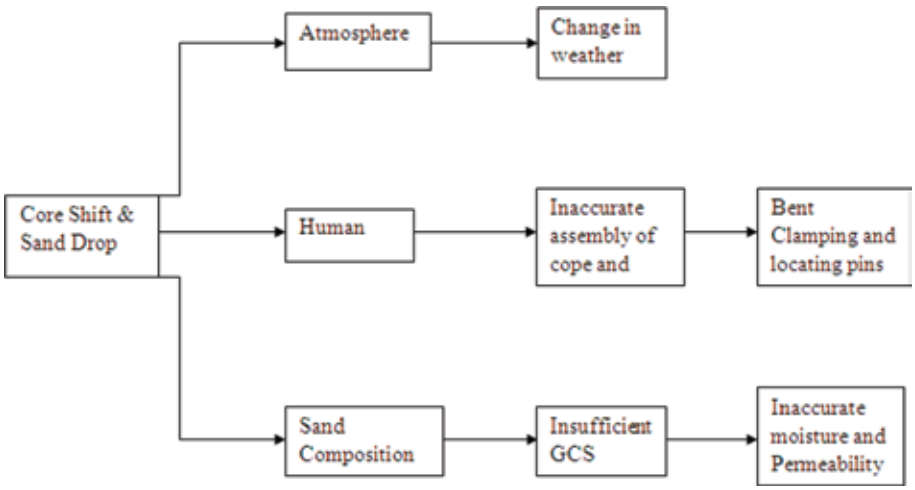

Figure 4.
Why-Why analysis for core shift and sand drop.

The above equation provides an equation that co-relates GCS, permeability, compactibility and moisture with % Rejection. The above equation has an R square value of 0.949, which means 94.9% of the data fits the model. After carrying out DOE, an analysis of variance is required that shows us which factor is the most critical according to the data.

From **Table 5**, it is seen that the P value of permeability is the least as it is less than 0.05. This shows that moisture plays a critical role in the properties of sand and the defects caused by it.

GCS	Permeability	Compactibility	Moisture	% reject
1050	102	38	3.8	15.38
1100	102	38	3.7	9.09
1080	99	39	3.7	10
1020	102	39	3.8	12.82
1050	102	38	3.7	22.22
1020	100	38	3.7	33.33
1050	101	39	3.8	11.76
1060	104	38	3.9	22.72
1020	102	39	3.8	16.66
1050	102	39	3.7	25
1050	99	39	3.7	8.57
1070	99	39	3.7	11.11
1050	105	39	3.8	3.7
1070	105	39	3.7	4.34
1050	99	38	3.7	2.7
1080	102	39	3.7	20
1070	100	39	3.8	28.57
1100	105	42	4	10.34
1100	102	39	3.8	6.89
1020	102	39	3.8	21.42
1020	102	38	3.7	12.5
1050	102	37	3.9	6.66
1020	102	38	3.7	13.33

Table 4.
DOE table for sand parameters vs. % rejection.

	DF	Adj SS	Adj MS	F-value	P-value
GCS	5	4.79	0.96	0.67	0.653
Permeability	5	11.06	221.29	8.68	0.001
Compactibility	3	0.77	0.26	0.18	0.907
Moisture	3	128	42.77	1.68	0.217

Table 5.
ANOVA table.

8. Process sigma calculation

When a process is being improved, we calculate the process standard deviation and sigma value. These are considered to be short-term values because the data only contains common cause and thus are only reliable as long as there is no deviation from the current data. For our industry, the process sigma has been calculated in **Table 6**.

9. Calculation of yield

Yield of existing component:

$$\begin{aligned}\text{volume of part} &= \text{mass/density}\\ &= 58.5\ \text{kg}/7800\ \text{kg/m}^3\\ &= 8.4\times10^{-3}\ \text{m}^3\\ \text{volume of riser} &= \prod \text{D}^2/4\times\text{H}\\ &= 0.644\times10^{-3}\\ \text{volume of gating system} &= \text{volume of basin} + \text{volume of sprue}\\ &\quad + \text{volume of runner} + \text{volume of gates}\\ &= 2.008\times10^{-3}\\ \text{yield} &= \text{volume of part}/(\text{volume of part} + \text{volume of runner}\\ &\quad + \text{volume of gating system})\\ &= 8.4\times10^{-3}/\left(8.4\times10^{-3}+0.644\times10^{-3}+2.008\times10^{-3}\right) = 76.1\%\end{aligned}$$

Castings produced	Rejected castings	Defects %	Yield (part)	Process Sigma	DPMO
222	10	4.5	95.5	3.19	450,454
109	9	8.26	91.74	2.89	82,569
275	32	11.64	88.36	2.69	116,364
225	31	13.78	86.22	2.59	137,778
134	14	10.45	89.55	2.76	104,478
104	38	36.54	63.46	1.84	265,385
121	17	14.05	85.95	2.58	140,496
79	13	16.46	83.54	2.48	164,557
198	15	7.58	92.42	2.93	75,758
152	51	33.55	66.45	1.92	335,526
66	11	16.67	83.33	2.47	166,667
199	16	8.04	91.96	2.9	80,402
58	8	13.79	86.21	2.59	137,931
179	26	14.53	85.47	2.56	145,251
165	34	20.61	79.39	2.32	206,061
Average					
152.4	21.67	15.36	84.63	2.58	173978.5

Table 6.
Sigma process table for 1 year.

Yield of modified component:

$$\text{volume of part} = \text{mass/density}$$
$$= 58.5\ \text{kg}/7800\ \text{kg/m}^3$$
$$= 8.4 \times 10^{-3}\ \ \text{m}^3$$
$$\text{volume of riser} = \prod \text{D}^2/4 \times \text{H}$$
$$= 1.45 \times 10^{-3}$$
$$\text{volume of gating system} = \text{volume of basin} + \text{volume of sprue} + \text{volume of runner} + \text{volume of gates}$$
$$= 1.98 \times 10^{-3}$$
$$\text{yield} = \text{volume of part}/(\text{volume of part} + \text{volume of runner} + \text{volume of gating system})$$
$$= 8.4 \times 10^{-3}/\left(8.4 \times 10^{-3} + 1.45 \times 10^{-3} + 1.98 \times 10^{-3}\right) = 71.4\%$$

Here, yield is decreased by 4.7%.

10. Conclusion

Preliminary defect analysis shows that, compared to other products, Crank Case 3000 has the highest rejection rate of 15.4%. A bar chart shows that, compared to the other defects, core shift and sand drop were observed to be most common. This fact is proved by the Pareto analysis that shows that core shift and sand drop are the cause of more than 80% of the rejections. Many factors affect core shift and sand drop. To find out which of the factors was contributing the most, a cause effect diagram and Why Why analysis was performed. From the cause effect diagram, a weighted average table was created to find out the key causes of the defects, where the causes with the highest weighted average were taken into consideration, which includes sand parameters like GCS, permeability, moisture and compactibility. From the Why Why analysis, it was observed that out of all the root causes available, the controllable factors were the sand parameters of molding sand while the rest of the factors are not controllable. So these factors were selected for further analysis. After carrying out experiments (DOE) on sand parameters (GCS, permeability, compactibility and moisture) and the rejection rates, it was found that a 3% change in permeability results in a 20–25% change in the rejection rate. Thus optimum changes in permeability are required to control rejection rate. Application of new sand parameters and design gives sound casting but a compromise in yield of 4.7% is acquired.

Author details

R.S. Barot[1*], M. Iyer[1], S. Pampaniya[1], J. Mori[1], H. Panchal[1], B. Sharma[2] and J. Shah[2]

1 Birla Vishwakarma Mahavidyalaya, Vallabh Vidyanagar, India

2 Finecast (Gujarat) Pvt. Ltd, V U Nagar, India

*Address all correspondence to: rsbarot@bvmengineering.ac.in

IntechOpen

References

[1] Kamble BS. Analysis of different sand casting defects in a medium scale foundry industry—A review. International Journal of Innovative Research in Science, Engineering and Technology. 2016;**5**:1281-1288

[2] Malhotra V, Kumar Y. Casting defects: An literature review. International Journal of Design and Manufacturing Technology. 2016;**7**(1): 60-62

[3] Rajkolhe R, Khan JG. Defects, causes and their remedies in casting process: A review. International Journal of Research in Advent Technology. 2014; **2**(3):375-383

[4] Rai A, Ganguly SK. Web-based expert system for some defect in sand castings. International Journal of Advanced Engineering Research and Studies. 2015;**2**(Jan.-March):171-174

[5] Blair M, Monroe R, Beckermann C, Hardin R, Carlson K, Monroe C. Predicting the occurrence and effects of defects in castings. JOM. 2005;**57**(5): 29-34

[6] Malhotra V, Kumar Y. Casting defects: A literature review. International Journal of Design and Manufacturing Technology (IJDMT). 2016;**7**:60-62

[7] Ingle V, Sorte M. Defects, root causes in casting process and their remedies. Journal of Engineering Research and Application (JERA). 2017;**7**:47-54

[8] Kassie AA, Assfaw SB. Minimization of casting defects. IOSR Journal of Engineering. 2013;**3**(5):31-38

[9] Nawi I, Siswanto WA, Ismail AE. A study of auto pour in sand casting process. Applied Mechanics and Materials. 2014;**660**:74-78

[10] Choudhari CM, Narkhede BE, Mahajan SK. Casting design and simulation of cover plate using AutoCAST-X software for defect minimization with experimental validation. Procedia Materials Science. 2014;**6**:786-797

[11] Heavey C, Murphy E. Integrating the balanced scorecard with six sigma. The TQM Journal. 2012;**24**(2):108-122

[12] Reddy GP, Reddy VV. Process improvement using Six Sigma–A case study in small scale industry. International Journal of Six Sigma and Competitive Advantage. 2010;**6**(1-2): 1-11

[13] Gijo EV, Scaria J. Reducing rejection and rework by application of six sigma methodology in manufacturing process. International Journal of Six Sigma and Competitive Advantage. 2010;**6**(1-2): 77-90

[14] Kumaravadivel A, Natarajan U. Application of six-sigma DMAIC methodology to sand-casting process with response surface methodology. The International Journal of Advanced Manufacturing Technology. 2013;**69** (5-8):1403-1420

Chapter

An Integrated Hybrid Renewable Energy System Based on Doubly Fed Induction Generator for Disperse Generation

Neeraj Kumar Mishra and Zakir Husain

Abstract

An isolated new hybrid scheme employing a doubly fed induction generator (DFIG) fed by solar power and grid integrated with a simple three-phase square-wave neutral point clamped (NPC) inverter has been proposed. This works as an uninterruptable power source that can feed a DFIG in all cases. The primary source of power is SPV and shortage power can be provided by the grid. The distinctive "integrated" strategy removes the complexity of designing a boost converter, battery controller, rectifier and natural point clamped (NPC) inverter and reduces the number of sensors and electronic components. In this approach, the simplest way of modeling is introduced. The presence of a grid-connected rectifier in parallel (with the SPV source) ameliorates the quality of power fed into the DFIG by curtailing the voltage dip in the SPV output. Also, the other benefits of the proposed system are high-reliability, compact size and low cost, which makes the system suitable for real-time simulation. All the analytical, simulation results of the present research are presented.

Keywords: solar PV, MPPT, converters, NPC inverter, doubly fed induction generator

1. Introduction

It will be very painful for you to spend slightly more on your electricity bill if you knew it was sourced from the solar photovoltaic panel of your neighbor's roof. Since the quantity of energy presented from non-renewable sources is finite, renewable sources can be an alternative option for power generation [1]. Solar photovoltaic cells and Doubly Fed Induction Generators are green energy efficient sources with minimal environmental impact [2]. The wound rotor is usually fed by the stator or rotor, which is why it is frequently named a doubly fed induction generator (DFIG) in the literature [3, 4]. The different aspects of the hybrid system are that power conversion efficiency can be improved, overall cost of the system can be reduced, the power quality is improved and more reliable and utilization of power is optimized. Variation in grid injection power can be optimized. The rating of the SPV cell is taken higher so that the variation of grid injected power and reverse power flow can be minimized at the point of common coupling (PCC). Since this system does not allow for reverse

power flow at the PCC, because the boost converter is situated at the output of the PV and the rectifier is situated at the output of grid, the boost converter will not allow current in the reverse direction [2].

2. Power conversion system

The schematic diagram in **Figure 1** shows the complete technique. The MPPT can enhance up to 30% of energy compared to the standard photovoltaic panel and it is externally connected to the circuit. The main purpose of an MPPT is to change its input voltage, which is also the PV panel input voltage, so that it corresponds to the voltage at which the panel delivers maximum power. At its output, the MPPT always provides the voltage required by the battery or machine pump load [2]. The perturb and observe based MPPT has the following limitations.

1. In case voltage is far away from maximum power point, the perturb and observe based MPPT is slightly slow.

2. In case of silhouette on any SPV panel, voltage curve of the SPV will have several peaks, hence finding the real peak is very difficult.

3. The main difficulties related to the MPPT's used previously are the cost, efficiency and reliability of the separate high-power converter.

The proposed system planned to use the software Typhoon HIL [4]. Depending on application and requirement many types of induction generator are available in the Market. The designing of the induction generator is not a tedious task but controlling of Wound rotor induction generator, for wind energy conversion system, is a challenging task for electrical engineering fraternity [5].

2.1 Design aspect in proposed wind energy conversion system configuration (WECS)

The unpredictable nature of wind energy has forced us to design a hybrid system so that the stored energy from the solar power or grid can be fed to the rotor of doubly fed induction generator at the time of sub-synchronous mode. The relationship between wind velocity and output power of turbine is nonlinear. The output power can be represented as follows [3].

$$P_m = 0.5 * C_p(\lambda, \beta) * \rho * A * v^3 \quad (1)$$

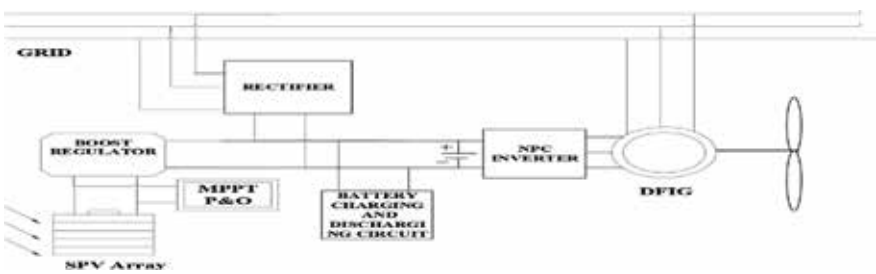

Figure 1.
Complete representation of proposed technique.

where P_m is the output power of the turbine, ϸ *is air density*, C_p is the power coefficient, ν is the velocity of wind, β is the pitch angle, λ *is the tip speed*.

2.2 Doubly fed induction generator

Since wind is an unpredictable source of energy, the slip s and rotor voltage amplitude can be defined as:

$$S = \frac{(N_s - N_r)}{N_s} \tag{2}$$

$$V_r = S * T_{sr} * V_s \tag{3}$$

where T_{sr} is voltage transformation ratio between stator and rotor, S is a slip, V_s is the stator voltage, V_r is the rotor voltage, N_s is the synchronous speed, N_r is the rotor speed.

The active power delivered to the rotor and the mechanical power delivered to the shaft of the generator can be calculated as:

$$P_r = -S * P_s \tag{4}$$

$$P_m = (1 - s) * P_s. \tag{5}$$

where P_r is the rotor power, P_s *is the stator power and* P_m *is the mechanical power*.

The universally accepted method of driving a mathematical model of DFIG is to convert the synchronously rotating stator flux vector in terms of quadrature axes and direct axes. A simplified mathematical model would help with behavior analysis.

Figure 2 represent an equivalent circuit for the DFIG in the synchronous reference frame [3].

$$v_{qds} = r_s\, i_{qds} + \frac{d\left(\psi_{qds}\right)}{dt} + j\,\omega_e\,\psi_{qds} \tag{6}$$

$$v_{qdr} = r_r\, i_{qdr} + \frac{d\left(\psi_{qdr}\right)}{dt} + j\,\omega_e\,\psi_{qdr} \tag{7}$$

$$\psi_{qds} = L_m\, i_{qdr} + L_m\, i_{qds} \tag{8}$$

$$\psi_{qdr} = L_m\, i_{qds} + L_m\, i_{qdr} \tag{9}$$

$$\begin{aligned} Te &= \frac{3p}{22}\, Re\left[j\,\psi_{qds}.\,\overline{i_{qds}}\right] \\ &= \frac{3p}{22}\, Re\left[j\,\psi_{qdr}.\,\overline{i_{qdr}}\right] \end{aligned} \tag{10}$$

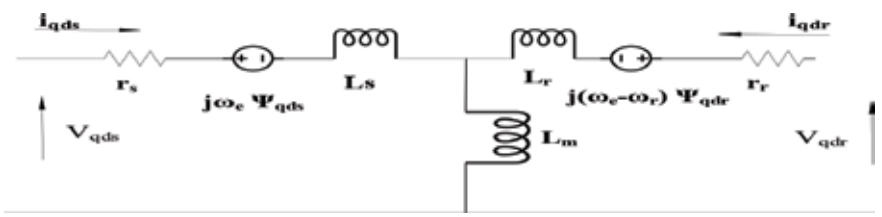

Figure 2.
Complex synchronous equivalent DFIG.

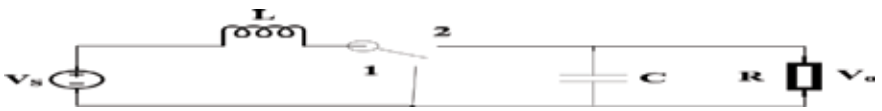

Figure 3.
Basic schematic boost converter with ideal switch.

The stator side active and reactive powers are given as:

$$P_s = \frac{3}{2}\,\mathrm{Re}\left[\mathrm{V_{qds}}.\,\overline{i_{qds}}\right] = \frac{3}{2}\left(\mathrm{v_{qs}\,i_{qs}} + \mathrm{v_{ds}\,i_{ds}}\right) \tag{11}$$

$$Q_s = \frac{3}{2}\,\mathrm{Im}\left[\mathrm{V_{qds}}.\,\overline{i_{qds}}\right] = \frac{3}{2}\left(\mathrm{v_{qs}\,i_{qs}} - \mathrm{v_{ds}\,i_{ds}}\right) \tag{12}$$

where. $\overline{i_{qdr}}$ and $\overline{i_{qds}}$ are the complex conjugates of the rotor-current and stator-current space vectors. $r_{s,}$ r_r are stator, rotor resistances (ohms), ψ_{qds}, ψ_{qdr} are d and q axes stator and rotor flux (wb), v_{qds}, v_{qdr}, are d and q axes stator and rotor voltages (Volt), i_{qds}, $i_{qdr,}$ are d and q axes stator and rotor current (Amp), torque is denoted by T_e, L_s, L_m is self and magnetizing inductance (henry), p is the number of poles per phase. P_s is the stator side active power, Q_s is the rotor side reactive power.

2.3 Power electronics converters

The rectifier and NPC inverter can be used to convert DC in to AC and AC in to DC and the boost regulator can boost the output of the photo voltaic cell. The boost converter is shown in **Figure 3**.

The output of the boost can be given by V_o.

$$V_o = \frac{V_s}{(1-\alpha)} \tag{13}$$

α is duty cycle, and V_s is input voltage, here it is solar panel voltage.

3. Simulation results and discussion

The model of **Figure 1** was developed and the results are presented in **Figure 4** as a real time output of the complete model. The simulation ran for time interval t = 1 s and the sample rate was 1MSPS sample per second. The various observations were recorded, such as the wave form of stator voltage V_s (abc), stator current I_s (abc), rotor side converter current I_r (abc), output voltage of solar photo voltaic cell

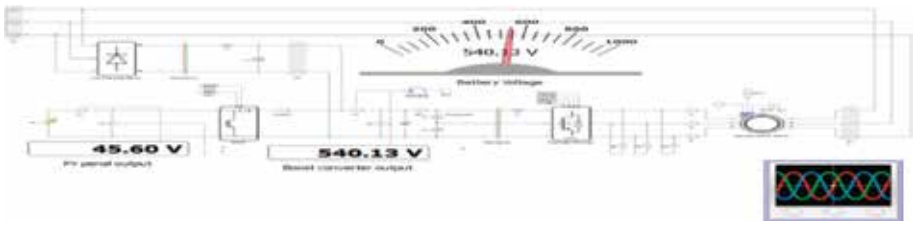

Figure 4.
Simulation result real time complete output.

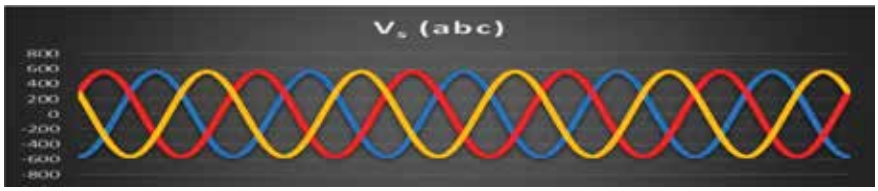

Figure 5.
Simulation result stator side output voltage.

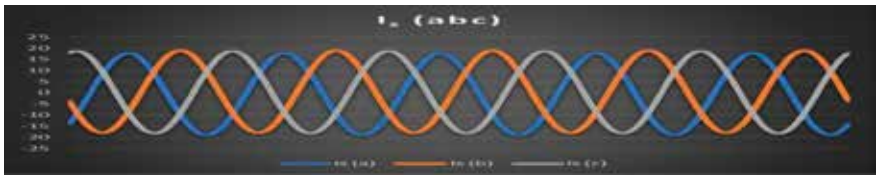

Figure 6.
Simulation result stator side output current.

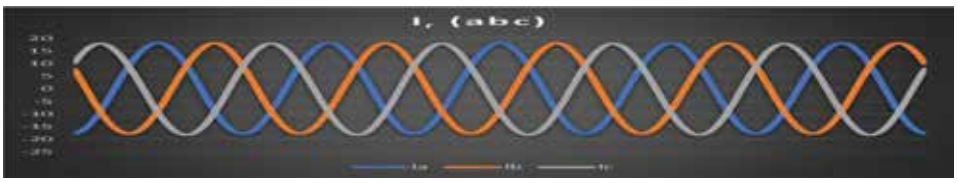

Figure 7.
Simulation result rotor side converter current.

Figure 8.
Output voltage of NPC Inverter.

boost converter output voltage and EMF of battery. The wave form of the stator side voltage also showed that the output voltage MPPT was 45.60 Volt. The output voltage of the battery was 540 Volt and the battery current was 2.37 amp and the power provided by the battery was 1.3 kW (**Figures 5–8**).

4. Conclusion

A simple, compact and cheap power converter system has been designed to deliver power from wind farms either to an isolated load or to the grid application. Its modeling analysis and design procedure have been presented. The SPV panel was used for the main source of rotor injunction and it reduced the power drawn by the rotor from the grid. For future use, the excess power from the SPV panel can be stored in the battery. The harmonics of stator voltage can also be reduced using an NPC inverter. The DFIG controller inverter and boost regulator have been designed

for low settling time with a very low overshoot and a good dynamic response. The complete system is simulated using Typhoon HIL® software. As stated earlier, both of the two energy sources were exactly modeled in Typhoon HIL® to forecast their real characteristics. Future work includes a low cost true MPPT controller and optimization of the integration of this MPPT into a standard PV panel.

A. Data for PV PANEL and DFIG

Number of cell = 72, standard light intensity = 1000 w/m^2, reference temperature = 25°C, short circuit current = 5.8 A, open circuit voltage = 45.6, temperature coefficient of short circuit current = 0.0004, stator resistance = 0.59 Ω, stator inductance = 35.81 mH, rotor resistance = 3.39 Ω, rotor inductance = 19.894 mH, mutual inductance = 1.104 H, no. of poles = 4, moment of inertia = 0.05 kg/m^2.

Conflict of interest

There is no conflict of interest.

Author details

Neeraj Kumar Mishra and Zakir Husain*
Department of Electrical Engineering, National Institute of Technology, Hamirpur, India

*Address all correspondence to: zahusain2@gmail.com

References

[1] Daniel SA, AmmasaiGounden N. A novel hybrid isolated generating system based on PV fed inverter-assisted wind-driven induction generators. IEEE Transactions on Energy Conversion. 2004;**19**(2):416-422

[2] Hansen AD, Sørensen PE, Hansen LH, Binder HW. Models for a Stand-alone PV System. Denmark: Forskningscenter Risoe. Risoe-R; No. 1219(EN). 2000

[3] Muller S, Deicke M, De Doncker RW. Doubly fed induction generator systems for wind turbines. IEEE Industry Applications Magazine. 2002;**8**(3):26-33

[4] Typhoon HIL. Real-Time Hardware-in-Loop (HIL) Platform. Typhoon HIL Control Centre Release 2015.1. Massachusetts, United States: Typhoon HIL, Inc., Somerville Professional, 2015

[5] Naidu NKS, Singh B. Grid-interfaced DFIG-based variable speed wind energy conversion system with power smoothening. 2017;**8**(1):51-58

Chapter

Experimental Study of a Conventional and Hybrid Solar Still

Hemin Thakkar, Sanjay Patel, Hitesh Panchal and P.V. Ramana

Abstract

The simple solar still has a limited output of pure water but its basic concept is very important for understanding desalination using solar energy. The yield of the solar still can be improved by using different energy storing materials in the basin and attaching different types of solar collectors. In this research, the flat plate collector and photovoltaic collector were used together to improve the output and performance. The output of the hybrid device was compared to an active solar still and conventional solar still. This research also included the effects of different energy storing materials in the output of a conventional solar still.

Keywords: solar still, hybrid still, desalination, FPC, PVC

1. Introduction

The solar still is a simple device used for desalination. It works on the hydrological cycle found in nature. It consists of a solar radiation absorbing basin, in which a constant amount of seawater is enclosed in a V-shaped glass cover as shown in **Figure 1**. The sun's rays pass through the glass cover and are absorbed by the blackened absorbing bottom of the basin. As the water is heated, its vapor pressure is increased. The resultant water vapor is condensed on the underside of the glass cover and runs down into the troughs, which conduct the distilled water to the reservoir.

The basic concept of passive solar still with its output was discussed by Murugavel et al. [1]. In this research, passive solar output was tested at the Government Polytechnic Ahmadabad and compared with the above research.

An active solar still with FPC also played a very important role in increasing the output of still as more heat was supplied through the FPC. Srithar et al. [2] demonstrated the effect of FPC on the output of a still. A hybrid solar still with FPC and PVC gave the best results in producing clean water from saline water as heat was added to the water by direct heating as in the conventional still and heating with FPC and PVC. The electricity produced by the PVC was used for heating the saline water and running the electric motors needed for supplying water to the still. In this preparative research, an experiment was carried out with three different configuration of stills and interesting results were obtained.

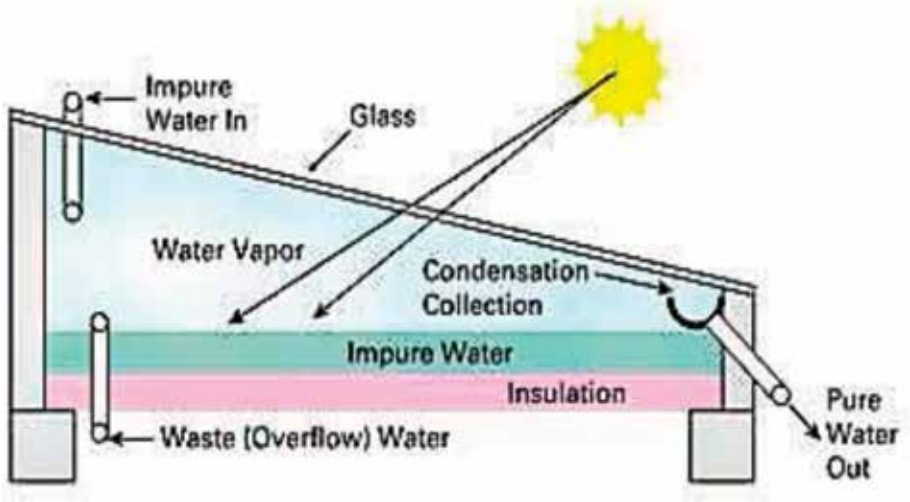

Figure 1.
Conventional solar still.

2. Experimental set-up of conventional solar still

The conventional still is the basic device used for desalination known as the CSS (conventional solar still). It converts the saline water into pure drinking water by heating the water as solar radiation passes through the glass cover and heats the blackened absorbing bottom of the still and evaporated vapor condenses on the underside of the cold glass. The glass is opaque material for solar radiation. It also works as a condensing surface for vapor produced in the still. Heating, evaporation and condensation take place in the same piece of equipment.

In this preparative project, conventional still output was tested and recorded at the Government Polytechnic, Ahmadabad. The experimental set-up is shown in **Figure 2**. The different temperatures, humidity, solar radiation and wind velocity were recorded and compared with the other still configurations.

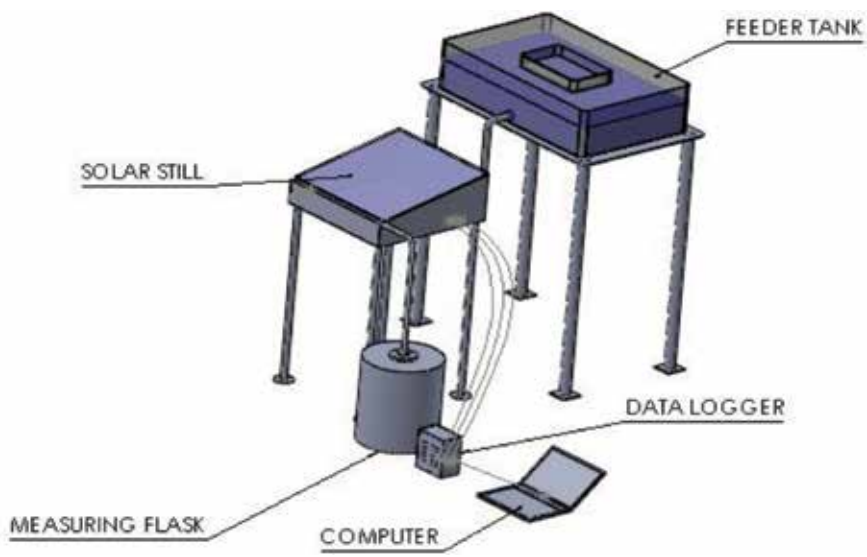

Figure 2.
Experimental set-up of CSS.

This is the simplest device used for solar desalination fabricated from fiber reinforced plastic (FRP) known as the passive still. The glass inclination was 45°. The basin area was 0.5 × 0.5 m^2.

3. Experimental set-up of the active solar still with FPC

In this active still, a flat plate collector (FPC) was added to a conventional still as an additional heat source for heating the saline water.

As more heat was added to the saline water, the output of the still increased during the experiment at Ahmedabad. The experiment set-up of the active still is shown in **Figure 3**. The data was recorded with the help of a data logger and stored in a laptop.

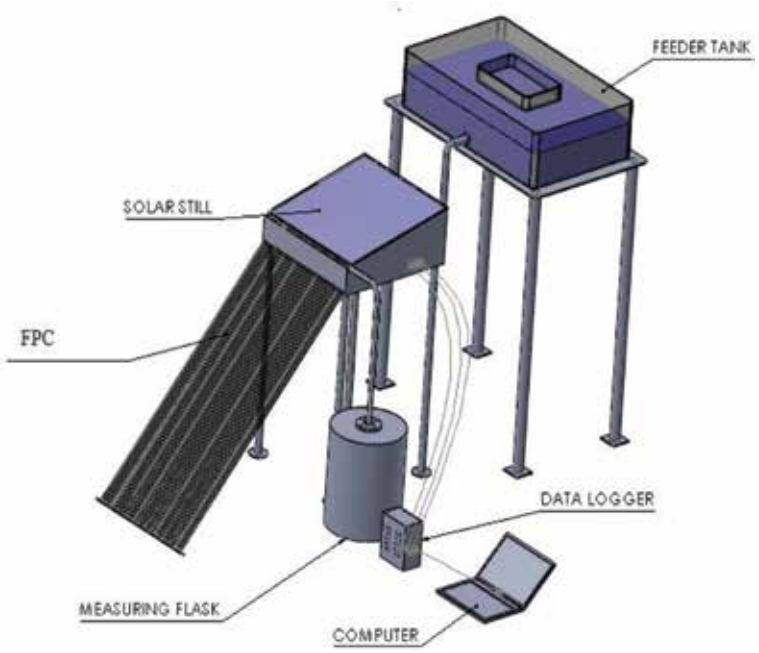

Figure 3.
Experimental set-up of the active solar still with FPC.

4. Experimental set-up of hybrid solar still with FPC and PVC

The hybrid solar still had different types of heat sources such as a flat plate collector, photovoltaic collector and evacuated tube collector. The output of the solar still with ETC was investigated by Panchal et al. [3]. In this experiment set-up we used FPC and PVC as additional solar heat sources as shown in **Figure 4**.

In this still, output was improved as two more solar heat sources added heat to the basin water. The readings of the still were recorded and pure water was collected in a measuring flask. This hybrid still also produced electricity at night, which was stored in battery to heat the water at night. The output of the PV battery was 30 W and this was converted into AC using an inverter. The AC powered heater was used to heat the saline water. A similar AC heater running with PVC was used by Riahi et al. [4].

A solar still with a PVC panel can be used as a roof-top system designed by Gujarat government. The PVC panel can play the role of electric energy generation and water heating for the purification of water. This hybrid still technique can play an important role in the smart city project of the Gujarat government.

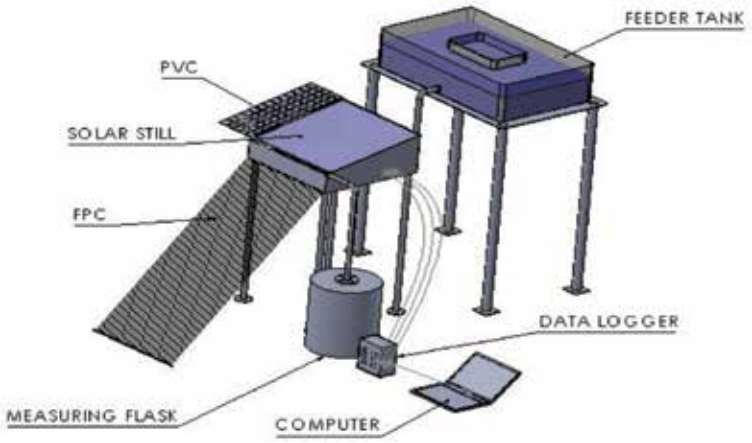

Figure 4.
Experimental set-up of hybrid solar still with PVC and FPC.

5. Effect of energy storing materials on the output of solar still

In this experiment, sand and concrete were used as energy storing materials. The solar energy was stored in these materials and released at night so the output could be improved. In this experiment, it was found that energy storing materials improved the output by up to 0.5 ml/day. Other energy storing materials found to be very effective in the literature are rubber, dye, jute clot, semi-conductors, high temperature super-conductor and nano materials.

Tabrizi et al. [5] conducted experiments in a still using sand as a heat reservoir at the bottom and found productivity was 75% higher than in a conventional still.

Sakthivel et al. and Panchal [6, 7] explained that black granite gravel as an energy storing material improved the efficiency by up to 20%.

Rubber and charcoal have also been used in basins. Akash et al. [8] tested different materials in the basin and found excellent outputs. Naim et al. [9] stated that a still basin lined with coal enhanced the absorption capacity of the basin. It gave better results.

Patel et al. [10] tried to enhance the output of a solar still by using different semi-conducting oxides (Photo-catalysts) like CuO, PbO_2 and MnO_2. Elango et al. [11] conducted experiments with nano-fluids of aluminum oxide (Al_2O_3), zinc oxide (ZnO) and tin oxide (SnO_2) and got better outputs. It is possible to use a high temperature superconductor as an energy storing material. The effect of high temperature super conductor (HTSC) as an energy storing material will be tested in future work.

This research tested the effect of sand and concrete on still output. It shows an improvement. It is possible to test other energy storing materials as stated in above review.

6. Result and discussion

The experiment was performed on 14–19 April 2017 and the following results were obtained for the conventional still. The average output of the test was 2 liters per day as shown in **Table 1**.

In the same way, the results were recorded for the other configurations of stills. The average outputs for the different configuration of solar still were recorded as shown in **Table 2**.

TIME	WATER TMEP (°C)	INNER GLASS TEMP. (°C)	AMBIENT TEMP. (°C)	RH (%)	WIND VELOCITY km/hr	OUTPUT ml
10:00 AM	37	39	29	10	8	0
11:00 AM	39	44	36	13	11	30
12:00 AM	42	47	38	12	12	70
01:00 PM	47	54	39	16	14	155
02:00 PM	50	57	39	11	12	270
03:00 PM	51	56	38	14	16	390
04:00 PM	49	53	37	12	18	510
05:00 PM	47	50	37	9	10	570
			Total output			1995

Table 1.
Yield of conventional solar still.

Device used	Out put liter	Duration
Conventional solar still	2	Day
CSS with sand and concrate	2.4 to 2.7	Day and night
Active soalar still with FPC	4 to 5	Day
Hybrid solar still with FPC and PVC	upto 7 to 8	Day and night

Table 2.
Average output of different configurations of still.

The active still and HSS gave better performance as shown in the above table. Energy storing material also affected the performance of the stills. The solar still with PVC can be used as a desalination device in the house whereas the PVC panels can be placed on the roof top of a house and electric energy generated by the PVC can be stored in a battery which can be used for heating the saline water in the still. This type of hybrid device can be developed to work with roof top system.

This hybrid system can be standardized and synchronized with the roof top system for the smart city project.

7. Conclusion

It has been found that the hybrid still gave the best results compared to other simple configurations of still. This research also suggests the use of other desalination techniques such as HDH and flash evaporation techniques with the solar still.

The conventional still is the simplest method of desalination and is useful for small family needs. But the HDH and flash techniques of desalination will be designed, fabricated and tested for the arid region of Gujarat for the output of 40–70 liters/day. It is also found in review of different techniques of desalination that HDH, flash evaporation and solar still together can be tested for better output in future work. The nano materials discussed above as energy storage materials will also be tested in future work with the solar still and HDH desalination device.

Author details

Hemin Thakkar[1*], Sanjay Patel[2], Hitesh Panchal[3] and P.V. Ramana[4]

1 Mechanical Department, Gujarat Technological University, Ahmedabad, Gujarat, India

2 Mechanical Department, Government Polytechnic, Ahmedabad, Gujarat, India

3 Mechanical Engineering Department, GEC, Patan, Gujarat, India

4 Mechanical Engineering Department, SVIT, Vasad, Gujarat, India

*Address all correspondence to: heminkumar@gmail.com

References

[1] Murugavel KK, Chockalingam KK, Srithar K. Progresses in improving the effectiveness of the single basin passive solar still. Desalination. 2008;**220**(1-3):677-686

[2] Srithar K, Mani A. Analysis of a single cover FRP flat plate collector for treating tannery effluent. Applied Thermal Engineering. 2004;**24**(5-6):873-883

[3] Panchal HN, Shah PK. Performance analysis of double basin solar still with evacuated tubes. Applied Solar Energy. 2013;**49**(3):174-179

[4] Riahi A, Wan Yusof K, Mahinder Singh BS, Isa MH, Olisa E, Zahari NAM. Sustainable potable water production using a solar still with photovoltaic modules-AC heater. Desalination and Water Treatment. 2016;**57**(32):14929-14944

[5] Tabrizi FF, Sharak AZ. Experimental study of an integrated basin solar still with a sandy heat reservoir. Desalination. 2010;**253**(1-3):195-199

[6] Sakthivel M, Shanmugasundaram S. Effect of energy storage medium (black granite gravel) on the performance of a solar still. International Journal of Energy Research. 2008;**32**(1):68-82

[7] Panchal HN. Use of thermal energy storage materials for enhancement in distillate output of solar still: A review. Renewable and Sustainable Energy Reviews. 2016;**61**:86-96

[8] Akash BA, Mohsen MS, Osta O, Elayan Y. Experimental evaluation of a single-basin solar still using different absorbing materials. Renewable Energy. 1998;**14**(1-4):307-310

[9] Naim MM, El Kawi MAA. Non-conventional solar stills part 1. Non-conventional solar stills with charcoal particles as absorber medium. Desalination. 2003;**153**(1-3):55-64

[10] Patel SG, Bhatnagar S, Vardia J, Ameta SC. Use of photocatalysts in solar desalination. Desalination. 2006;**189**(1-3):287-291

[11] Elango T, Kannan A, Murugavel KK. Performance study on single basin single slope solar still with different water nanofluids. Desalination. 2015;**360**:45-51

Chapter

Modeling of Material Removal Rate in Electrical Discharge Machining by a Novel Approach and Comparison of Prediction Accuracy with Other Models

C.R. Sanghani, G.D. Acharya and K.D. Kothari

Abstract

For any machining process, prediction of performance measures such as material removal rate (MRR), tool wear rate (TWR), surface roughness, etc. is important as it helps in the selection of input parameters for better performance. Different models have been proposed by researchers for the prediction of material removal rate in the electrical discharge machining (EDM) process. Due to several assumptions in the development of models, each model has the limitation of prediction accuracy. In this article, a new modeling approach for MRR is presented using experimental data from the well-known literature as a reference. The values of MRR predicted from this model were compared with that of different models. The results of the comparative analysis showed that the tendency of prediction is similar for all the models and the prediction accuracy of the newly developed model was higher compared to other models. Hence, this approach can be used to model MRR for a different combination of workpieces and tools.

Keywords: electrical discharge machining, modeling, MRR, prediction accuracy, comparison

1. Introduction

Electrical discharge machining (EDM) is a non-traditional machining process in which material removal takes place by thermal energy generated from sparking between the workpiece and tool [1]. To predict EDM performance measures, researchers have developed various models such as the mathematical model, numerical model, regression model, etc. based on this material removal theory. Each model has a different level of prediction accuracy due to their assumptions related to flushing efficiency, material properties of the workpiece and tool, the shape of the heat source, crater shape, etc. [2]. A mathematical model for MRR was developed by DiBitonto et al. [3] considering a point heat source and constant fraction of energy (F_c = 0.183) transferred to the cathode. Singh and Ghosh [4] estimated the electrostatic force responsible for material removal in a short pulse interval (<5 μs) using a thermo-electric model and calculated crater depth. For the estimation of the

geometrical dimensions of a micro-crater, Yeo et al. [5] proposed analytical models of the anode and cathode based on electro-thermal theory. Salonitis et al. [6] also developed models of the MRR and the average surface roughness by introducing the new concept of erosion front velocity. Madhu et al. [7] used the finite element method to predict MRR and the depth of damaged layer during EDM. The result showed that the spark-radius and the power intensity affect the geometrical dimensions of the crater. During thermal analysis of EDM in FlexPDE software, Lasagni et al. [8] observed that the material removal can be controlled by the melting enthalpy and the melting point. A 2D axisymmetric model of single spark EDM was developed by Joshi and Pande [9] considering realistic boundary conditions like Gaussian heat distribution, variable spark radius, latent heat of melting, etc. for prediction of the crater shape and MRR. Tao et al. [10] used FLUENT software to present a numerical model considering the plasma heating phase and the bubble collapsing phase for the material removal process. To simulate the crater formation due to a single discharge, Assarzadeh and Ghoreishi [11] developed an electro-thermal based model using ABAQUS software. The DFLUX subroutine was used to program the non-uniform heat flux. The maximum errors in predicting the crater radius and depth were 18.1% and 14.1%, respectively. Ming et al. [12] developed a hybrid model for EDM based on the finite-element method (FEM) and Gaussian process regression (GPR) to predict MRR and surface roughness. Puertas et al. [13] used response surface methodology to develop multiple regression equations for material removal rate, electrode wear and surface roughness. Using the nonlinear regression method with logarithmic data transformation, Chattopadhyay et al. [14] developed the empirical models for prediction of output responses. To investigate the effect of input parameters on material removal rate, electrode wear rate and surface roughness, Sanchez et al. [15] developed an inversion model based on the least squares theory. In the present work, a mathematical model for MRR is developed based on the new approach of using basic material removal theory and the regression method.

2. Experimentation

The experimental results presented in DiBitonto et al. [3] are used in this modeling approach, as it is one of the founding research works in the field of EDM quite often cited in EDM literature. Those data were obtained by electrical discharge machining of steel (iron) as the cathodic workpiece with copper as the anode. The average thermophysical properties of the workpiece are shown in **Table 1**.

Property	**Steel (iron)**
Density (kg/m^3)	7545
Thermal conductivity (W/m K)	56.1
Specific heat (J/kg K)	575
Melting temperature (K)	1808
Boiling temperature (K)	3134
Reference temperature (K)	298
Latent heat of melting (kJ/kg)	247
Latent heat of vaporization (kJ/kg)	6090

Table 1.
Thermophysical properties of workpiece.

3. Different models for prediction of MRR

3.1 Novel approach

In this work, a mathematical model for MRR is developed using the theory of melting and vaporization of material from the workpiece as well as experimental data shown in **Table 1**. The experimental results of MRR are used to calculate the volumetric rate of material removal from the workpiece.

The energy responsible for material removal from workpiece [16] is

$$E_{MRR} = \rho V_W \left[C_p (T_v - T_o) + L_m + L_v \right] \tag{1}$$

where ϱ - Density (kg/m^3), V_W - Volumetric material removal rate from workpiece (m^3/s), C_p - Specific heat (J/kg K), T_v - Vaporization temperature (K), T_o - Room temperature (K), L_m - Latent heat of melting (J/kg), L_v - Latent heat of vaporization (J/kg).

Energy released during single discharge per unit time [17] is

$$E = VI\left(\frac{T_{on}}{T_{on} + T_{off}}\right) \tag{2}$$

where V - Voltage (V), I - Discharge current (A), T_{on} - Pulse on time (μs), T_{off} - Pulse off time (μs).

Fraction of energy (%) responsible for material removal

$$F_{MRR} = \frac{E_{MRR}}{E} \times 100 \tag{3}$$

The regression equation for fraction of energy (%) responsible for material removal is developed using statistical software MINITAB 16 and is given by

$$F_{MRR} = 2.49 \times I^{0.9472} \times T_{on}{}^{-0.1855} \tag{4}$$

Energy responsible for material removal from workpiece

$$\begin{aligned} E_{MRR} &= F_{MRR} \times E \\ &= 0.0249 \times I^{0.9472} \times T_{on}{}^{-0.1855} \times VI\left(\frac{T_{on}}{T_{on} + T_{off}}\right) \\ &= \frac{0.0249 \times V \times I^{1.9472} \times T_{on}{}^{0.8145}}{T_{on} + T_{off}} \end{aligned}$$

$$\text{But, } E_{MRR} = \rho V_W \left[C_p (T_v - T_o) + L_m + L_v \right]$$

$$\frac{0.0249 \times V \times I^{1.9472} \times T_{on}{}^{0.8145}}{T_{on} + T_{off}} = \rho V_W \left[C_p (T_v - T_o) + L_m + L_v \right]$$

By putting the value of material properties of workpiece from **Table 1**,

$$V_W = \frac{4.1419 \times 10^{-4} \times V \times I^{1.9472} \times T_{on}{}^{0.8145}}{T_{on} + T_{off}} mm^3/sec$$

$$MRR = \frac{0.0248 \times V \times I^{1.9472} \times T_{on}{}^{0.8145}}{T_{on} + T_{off}} mm^3/min \quad (5)$$

The material removal rate can be obtained using Eq. (5) at any set of process parameters for a given workpiece and tool combination.

3.2 Other models

3.2.1 DiBitonto's model

DiBitonto et al. [3] developed a simple mathematical model of material removal from steel (iron) in EDM. An analytical solution of the model is presented using a point heat source and power as the boundary condition at the interface of plasma and workpiece. They assumed the plasma radius to be negligibly small and a constant fraction of energy transfer to the workpiece as 0.183 for a large range of discharge current. The maximum erosion rate is determined from

$$(V_w)_{max} = \frac{16\pi X^3 \tau_0{}^{3/2} F_c UI}{3(\tau_0 + \delta^*)(T_m - T_0)\rho C_p} \quad (6)$$

where X is given by

$$X^2 = \ln\left(\frac{1 + 3\delta^*/\tau_0}{4\pi^{3/2}\sqrt{\tau_0}}\right) \quad (7)$$

τ_0 - dimensionless optimum pulse time (μs), F_c - Fraction of power transfer, U - voltage (V), I - current (A), δ^* - dimensionless pause time, T_m - melting temperature (K), T_0 - room temperature (K), ϱ - density (kg/m^3), C_p - specific heat (W/m K).

3.2.2 Joshi's model

A thermophysical model for the EDM process has been developed by Joshi and Pande [9] using finite element analysis. It has been carried out to predict the material removal rate by considering more realistic boundary conditions like Gaussian distribution of heat flux, spark radius based on discharge current and pulse on time, latent heat of melting, energy distribution factor for workpiece as 0.183, and neglecting convection heat loss from workpiece.

3.2.3 Assarzadeh's model

A comprehensive electro-thermal based single spark EDM model has been developed by Assarzadeh and Ghoreishi [11]. This model has been developed based on temperature dependent materials properties, Gaussian distribution of heat flux, convection, latent heat of fusion and expanding plasma channel with current and pulse on time. They have also assumed constant energy dispersing into the workpiece as 18% of total energy for all of the process parameters.

3.2.4 Ming's model

Ming et al. [12] constructed a thermal model of single-spark EDM process based on the finite element method, considering the variable heat distribution factor for the workpiece, latent heat and plasma flushing efficiency (PFE), to predict material removal rate. They derived an equation of heat distribution factor for the workpiece from experimental data presented by Singh [17] considering the dissimilarity of machining conditions, work-tool materials and mainly the thermal conductivity of the workpiece by assuming the proportionality coefficient.

4. Results and discussion

4.1 Validation of model

For investigation of the validity of the mathematical model of MRR, the predicted results are compared with the experimental results from DiBitonto et al. [3] as shown in **Table 2**. It can be seen that the results predicted by the proposed model of MRR have a close agreement with the experimental results.

4.2 Comparison of different models

To obtain the prediction accuracy and to explore the generalization capabilities of this model to the real state EDM process, a comparative analysis of different models (Our model, DiBitonto et al. [3], Joshi and Pande [9], Assarzadeh and Ghoreishi [11], Ming et al. [12]) has been made here. The machining conditions used for development of our model were exactly the same as adopted by the reported models. The results of the experiments, predicted by other models as well as our model, are shown in **Table 2**. **Figure 1** shows the comparison of MRR predicted by different analytical and numerical models as well as the experimental data. It is observed that our model exhibits the same tendency of variation as that offered by either experiments or other models. It can also be seen that the values of MRR predicted by our model are much closer to the experimental results when compared to those by reported models. The fraction

Exp. No.	I (A)	T_{on} (µs)	T_{off} (µs)	MRR (mm^3/min)					
				Experiment	Our model	DiBitonto's model	Joshi's model	Assarzadeh's model	Ming's model
1	2.3	5.6	1	0.30	2.00	13.82	12.13	8.00	1.07
2	2.9	7.5	1.3	1.60	2.79	17.26	16.36	9.08	2.61
3	3.7	13	2.4	3.10	4.09	21.78	20.37	11.99	5.78
4	5.3	18	2.4	8.40	8.23	35.58	34.49	23.02	17.52
5	8.5	24	2.4	23.20	20.17	63.79	62.86	41.22	27.73
6	10	32	2.4	32.00	26.85	77.18	76.37	53.84	43.38
7	13	42	3.2	50.50	41.24	100.33	96.68	65.05	59.64
8	20	56	3.2	89.70	94.91	164.65	152.81	110.26	129.24
9	25	100	4.2	125.00	133.53	207.2	197.92	139.82	148.29

Table 2.
Comparison of the experimental and predicted results.

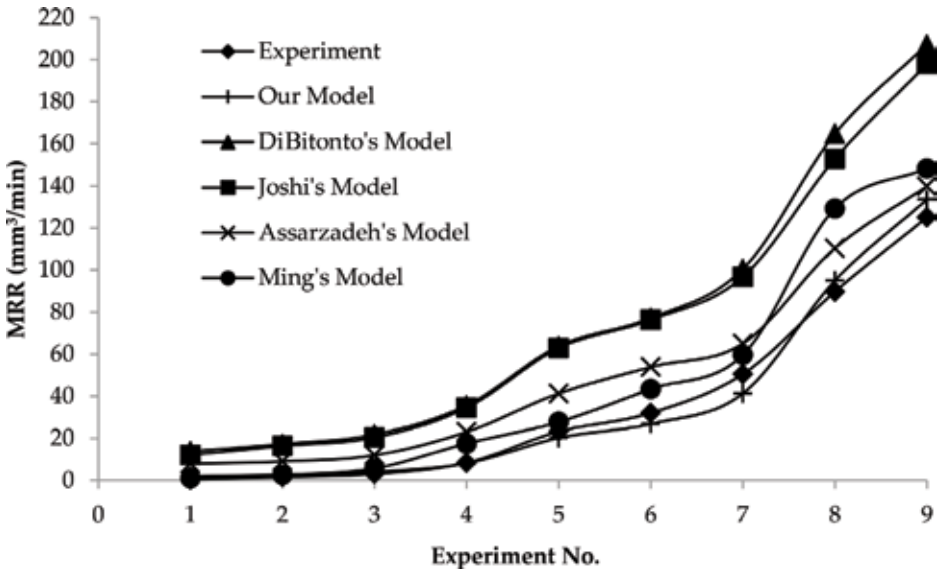

Figure 1.
Comparison of the theoretical and experimental results on MRR.

of energy transfer is a critical parameter to obtain material removal rate and the models of DiBitonto, Joshi and Assarzadeh have assumed constant fraction of energy transfer to workpiece, which is likely to depend on the discharge current and the pulse duration. Ming et al. [12] used a fraction of energy transfer equation based on discharge current and pulse on time but it was derived considering proportionality coefficient due to different work material. All these numerical and analytical models deviate remarkably from the experimental results exhibited by DiBitonto et al. [3]. This reveals that the assumption of a constant fraction of energy transfer to the workpiece is most likely to be incorrect. In our model, the fraction of energy transfer equation based on discharge current and pulse on time is derived from experimental data incorporating real state conditions. Thus, it could be concluded that our model is more suitable and accurate in predicting the MRR when compared to the reported models.

5. Conclusion

Modeling is important for any machining process as it helps in the prediction of performance measures. Researchers have used various techniques such as mathematical modeling, dimensional analysis, numerical modeling, regression modeling, etc. for modeling the EDM process. In this paper, a novel technique for modeling of the MRR is introduced based on the material removal mechanism and regression method. For the development of the MRR model, experimental data were used from literature (DiBitonto et al. [3]). To investigate the prediction accuracy, values of MRR obtained from our model were compared with the results of earlier analytical and numerical models and the published experimental data. It was found that the MRRs predicted by our model had much closer proximity to experimental results than those reported by other models. This model can further be used to conduct comprehensive studies on the EDM process to acquire optimal performance.

Author details

C.R. Sanghani[1*], G.D. Acharya[2] and K.D. Kothari[3]

1 School of Engineering, R. K. University, Rajkot, Gujarat, India

2 Atmiya Institute of Technology and Science, Rajkot, Gujarat, India

3 Mechanical Engineering Department, School of Engineering, R. K. University, Rajkot, Gujarat, India

*Address all correspondence to: scr1385@yahoo.com

References

[1] Ho KH, Newman ST. State of the art electrical discharge machining (EDM). International Journal of Machine Tools and Manufacture. 2003;**43**(13):1287-1300

[2] Escobar AM, de Lange DF, Medellin Castillo HI. Mint: Comparative analysis and evaluation of thermal models of electro discharge machining. International Journal of Advanced Manufacturing Technology. 2017;**89**(1-4):743-754. DOI: 10.1007/s00170-016-9125-z

[3] DiBitonto DD, Eubank PT, Patel MR, Barrufet MA. Theoretical models of the electrical discharge machining process. I. A simple cathode erosion model. Journal of Applied Physics. 1989;**66**(9):4095-4103

[4] Singh A, Ghosh A. A thermo-electric model of material removal during electric discharge machining. International Journal of Machine Tools and Manufacture. 1999;**39**(4):669-682

[5] Yeo SH, Kurnia W, Tan PC. Electro-thermal modelling of anode and cathode in micro-EDM. Journal of Physics D: Applied Physics. 2007;**40**(8):2513

[6] Salonitis K, Stournaras A, Stavropoulos P, et al. Thermal modeling of the material removal rate and surface roughness for die-sinking EDM. International Journal of Advanced Manufacturing Technology. 2009;**40**:316-323. DOI: 10.1007/s00170-007-1327-y

[7] Madhu P, Jain VK, Sundararajan T. Analysis of EDM process: A finite element approach. Computer Engineering. 1991;**2**:121

[8] Lasagni A, Soldera F, Mücklich F. FEM simulation of local heating and melting during electrical discharge plasma impact. Modelling and Simulation in Materials Science and Engineering. 2004;**12**(5):835

[9] Joshi SN, Pande SS. Thermo-physical modeling of die-sinking EDM process. Journal of Manufacturing Processes. 2010;**12**(1):45-56

[10] Tao J, Ni J, Shih AJ. Modeling of the anode crater formation in electrical discharge machining. Journal of Manufacturing Science and Engineering. 2012;**134**(1):011002

[11] Assarzadeh S, Ghoreishi M. Electro-thermal-based finite element simulation and experimental validation of material removal in static gap single-spark die-sinking electro-discharge machining process. Proceedings of the Institution of Mechanical Engineers, Part B: Journal of Engineering Manufacture. 2017;**231**(1):28-47

[12] Ming W, Zhang G, Li H, et al. A hybrid process model for EDM based on finite-element method and Gaussian process regression. International Journal of Advanced Manufacturing Technology. 2014;**74**:1197-1211. DOI: 10.1007/s00170-014-5989-y

[13] Puertas I, Luis CJ, Alvarez L. Analysis of the influence of EDM parameters on surface quality, MRR and EW of WC–Co. Journal of Materials Processing Technology. 2004;**153**:1026-1032

[14] Chattopadhyay KD, Verma S, Satsangi PS, Sharma PC. Development of empirical model for different process parameters during rotary electrical discharge machining of copper–steel (EN-8) system. Journal of Materials Processing Technology. 2009;**209**(3):1454-1465

[15] Sánchez HT, Estrems M, Faura F. Development of an inversion model for establishing EDM input parameters to satisfy material removal rate,

electrode wear ratio and surface roughness. The International Journal of Advanced Manufacturing Technology. 2011;**57**(1-4):189-201

[16] Shen Y, Liu Y, Zhang Y, Tan B, Ji R, Cai B, et al. Determining the energy distribution during electric discharge machining of Ti–6Al–4V. The International Journal of Advanced Manufacturing Technology. 2014;**70**(1-4):11-17

[17] Singh H. Experimental study of distribution of energy during EDM process for utilization in thermal models. International Journal of Heat and Mass Transfer. 2012;**55**(19-20):5053-5064

Chapter

Experimental Investigation of Effect of Tool Nose Radius and Cutting Parameters on Surface Roughness of Ti-6Al-4 V (ELI)

Darshit R. Shah and Sanket N. Bhavsar

Abstract

Titanium alloys have superior mechanical properties such as high strength to weight ratio, low elastic modulus and high corrosion resistance. The importance of surface finish has increased in specific applications such as aerospace components, biomedical instruments and cryogenic equipment. The lower amount of oxygen, carbon and iron content has made Ti-6Al-4 V Extra Low Interstitial (ELI) perfect for such applications. In this paper, a second order model is developed to correlate the effect of four parameters namely cutting speed, feed, depth of cut and tool nose radius on surface roughness of Ti-6Al-4 V ELI. Three levels were chosen for all four parameters. Three coated cutting tool inserts with three different nose radii of 0.4, 0.8 and 1.2 mm were used. The Box–Behnken method of response surface methodology was adopted to minimize the number of experiments. Data of 27 experiments were used to build the model and predict the surface roughness using the response surface methodology. The model was tested by ANOVA. The predicted value of surface roughness varies only 1.5% with the experimental result, which confirms acceptability of the developed model.

Keywords: titanium alloy, RSM, ANOVA, tool nose radius, surface roughness

1. Introduction

Surface roughness is a key feature for selection of material required to make any component, especially when it is used in applications such as biomedical implants [1], orthopedic implants, cryogenic and marine equipment. Ti-6Al-4 V Extra Low Interstitials (ELI) has a low oxygen, carbon and iron content. It exhibits properties such as a high strength to weight ratio, relatively low elastic modulus and remarkable corrosion resistance, which makes it perfectly suitable for application in aerospace components [2]. With many superior qualities, the material also has disadvantages such as difficult to machine, high chemical reactivity and low thermal conductivity. Titanium alloys are suitable for components having high reliability and hence the surface roughness must be maintained to a desired level [3]. Investigation of cutting parameters on finished products has been undertaken by many researchers. Parameters such as cutting speed, feed, depth of cut [3–6], cutting tool inserts [5] and cutting time [6] are investigated by many researchers. The effect of cutting parameters on

power consumption and surface roughness while turning EN-31 was investigated by [7]. The effect of cutting speed, feed and depth of cut on cutting temperature while turning EN-36 was also investigated by [8]. A larger nose radius created a finer surface finish [3, 8]. Chou and Song [9] investigated the effect of tool nose radius on finish hard turning and reported that a large nose radius gave a better surface finish but at the same time induces higher tool wear. In the present paper, the effect of four input parameters namely cutting speed, feed, depth of cut and tool nose radius on surface roughness are investigated. Experiments were randomized using the Box–Behnken method, which is an effective method of response surface methodology. Using these experimental data, a second order model was developed to predict the response. The model was tested by the popular method of Analysis of Variance (ANOVA). Confirmation of the experiment was carried out in order to check the acceptability of the developed model.

2. Experimental procedure

2.1 Workpiece and cutting tool

The material used for the experiment was Ti-6Al-4 V ELI and this was available in the form of a round bar with a 70 mm diameter and 250 mm length. The properties of the material is shown in **Table 1**.

The cutting insert used was coated cemented carbide inserts with ISO designation as TNMG 160404, TNMG 160408 and TNMG 160412 with nose radius 0.4, 0.8 and 1.2 mm respectively.

2.2 Machining tests

All experiments were performed in a dry environment using CNC turning center STC-200. The surface roughness was measured at three different positions and then the average was noted. The measurement was done using a Mitutoyo SJ-210 surface roughness tester. Four different cutting parameters were chosen. Cutting speed, feed and depth of cut are process parameters and nose radius is the parameter of the cutting tool geometry. **Table 2** indicates cutting parameters and their levels.

Density	Hardness, Rockwell C	Ultimate tensile strength	Yield tensile strength	Elongation of break	Modulus of elasticity	Poisson's ratio
4.43 g/cc	35	860 MPa	790 MPa	15%	133.5 GPa	0.342

Table 1.
Properties of Ti-6Al-4 V ELI.

Parameters	Levels		
Feed (mm/rev)	0.05	0.1	0.15
Cutting Speed (m/min)	60	110	160
Depth of Cut (mm)	0.5	1	1.5
Tool Nose Radius (mm)	0.4	0.8	1.2

Table 2.
Cutting parameters and levels.

Figure 1.
CNC turning centre STC-200.

In this study, the Box–Behnken method of response surface methodology was adopted. It is a highly suitable method for minimizing the number of experiments required for investigation. As in this case, four different parameters with three levels were chosen, a total of 27 experiments were performed in an order sequence determined by the Box–Behnken method. Experimental set up is shown in **Figure 1** and the corresponding cutting parameters with measured responses are listed in **Table 3**.

Run order	Cutting speed (cs)	Feed (f)	Depth of cut (doc)	Nose radius (nr)	Surface roughness (Ra)
	m/min	mm/rev	mm	mm	μm
1	60	0.05	1	0.8	6.573
2	160	0.05	1	0.8	6.076
3	60	0.15	1	0.8	5.977
4	160	0.15	1	0.8	5.864
5	110	0.1	0.5	0.4	8.961
6	110	0.1	1.5	0.4	8.675
7	110	0.1	0.5	1.2	3.519
8	110	0.1	1.5	1.2	2.872
9	60	0.1	1	0.4	8
10	160	0.1	1	0.4	7.954
11	60	0.1	1	1.2	2.851
12	160	0.1	1	1.2	2.348
13	110	0.05	0.5	0.8	5.672
14	110	0.15	0.5	0.8	5.652
15	110	0.05	1.5	0.8	5.162
16	110	0.15	1.5	0.8	5.011
17	60	0.1	0.5	0.8	4.886
18	160	0.1	0.5	0.8	4.786
19	60	0.1	1.5	0.8	4.485
20	160	0.1	1.5	0.8	4.318

Run order	Cutting speed (cs)	Feed (f)	Depth of cut (doc)	Nose radius (nr)	Surface roughness (Ra)
	m/min	mm/rev	mm	mm	µm
21	110	0.05	1	0.4	7.89
22	110	0.15	1	0.4	7.672
23	110	0.05	1	1.2	2.293
24	110	0.15	1	1.2	2.035
25	110	0.1	1	0.8	4.235
26	110	0.1	1	0.8	4.019
27	110	0.1	1	0.8	3.972

Table 3.
Design of experiments and measured responses.

3. Result and discussion

A total of 27 experiments were performed and results were used to investigate the effect of parameters on surface roughness. It was found that the range of surface roughness varied from 2.035 to 8.961 µm. The relationship between the cutting parameters and surface roughness was developed using Minitab-17, which can be expressed as

$$\begin{aligned} Ra = {} & 20.73 - 0.0482\,cs - 66.4\,f - 4.58\,doc - 12.83\,nr \\ & + 0.000232\,cs{*}cs + 320\,f{*}f + 2.26\,doc{*}doc + 4.37\,nr{*}nr \\ & - 0.0007\,cs{*}doc - 0.0057\,cs{*}nr - 0.45\,doc{*}nr \end{aligned}$$

In order to check the adequacy of the model, an Analysis of variance test was performed. It consists of three tests i.e. significance of regression model, significance of coefficients and lack of fit. It showed that the model has a 93.62% of coefficient of correlation (R^2). **Table 4** shows the ANOVA for the current model for Ra, from which it can be said that the nose radius has the maximum effect in

Source	DF	Adj SS	Adj MS	F-value	P-value	% contribution
cs	1	0.974	0.9736	100	0.043	7.27
f	1	1.682	1.6815	137.2	<0.001	9.98
doc	1	1.063	1.0627	241	<0.001	17.52
nr	1	63.42	63.4202	652	<0.001	47.41
cs*doc	1	0.857	0.8566	8.8	0.52	0.64
cs*nr	1	0.65	0.6496	6.6	0.574	0.48
doc*nr	1	1.727	1.7266	17.8	0.365	1.29
Error	12	23.348	1.9457			3.48
Lack-of-Fit	10	17.697	1.7697	0.63	0.75	
Pure Error	2	5.651	2.8257			
Total	26	104.843				100

Table 4.
ANOVA table for Ra.

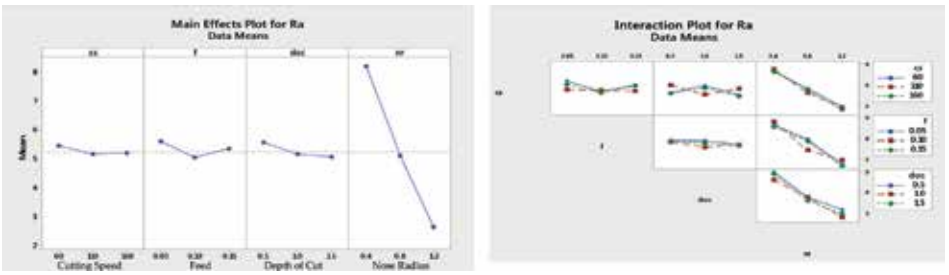

Figure 2.
Main and interaction effects.

reduction of surface roughness followed by depth of cut and feed rate. And among the interactions, the depth of cut and nose radius have greatest effect on Ra.

The effects of the main factors and interaction of the factors on surface roughness are shown in **Figure 2**. It can be observed from the main effect graph that surface roughness improves with higher cutting speed. This is due to less dissipation of heat from the workpiece at higher cutting speeds and a reduction in cutting force. The increase in surface roughness at a higher feed rate is the result of less available time to carry out the heat from the cutting zone as more material is removed, which causes accumulation of chips between the tool and workpiece. The increase in cutting force at a higher feed rate is also responsible for an increase in surface roughness.

3.1 Optimization plot

The basic aim of this study was to investigate the relationship between the desired surface roughness and optimized cutting parameters. And to achieve it, RSM is a helpful technique. Here the goal is to minimize surface roughness. After the optimization process, the optimum values of the process parameters were obtained as shown in **Table 5**. The predicted and experimental value of response are shown in **Table 5**. **Figure 3** shows the optimization plots. In order to check the acceptability of the model, a confirmation test was also carried out. It can be clearly observed that the predicted value of surface roughness varies only 1.5% with the experimental result and hence the model seems to be acceptable.

Response	Optimized values of parameters				Predicted value (μm)	Experimental value (μm)
	Cs (m/min)	F (mm/rev)	Doc (mm)	Nr (mm)		
Ra	119.60	0.1035	1.1465	1.2	1.9257	1.895

Table 5.
Optimization result.

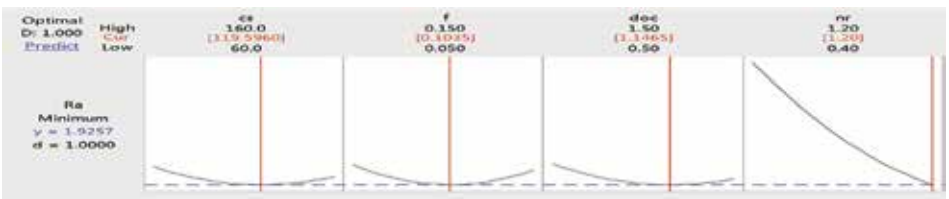

Figure 3.
Optimization plot.

4. Conclusion

In this study, a second order model was developed to investigate the effect of input parameters such as cutting speed, feed, depth of cut and tool nose radius on surface roughness of Ti-6Al-4 V ELI. The model was tested by ANOVA. The developed model was used to predict the values of the optimum process parameters in order to have minimum surface roughness. The optimum values were as follows: for cutting speed 119.59 m/min, feed rate 0.1035 mm/rev, depth of cut 1.1465 mm and nose radius 12 mm. This resulted in a predicted surface roughness of 1.9257 μm. The confirmation test was also conducted, which varies only by 15% that confirms the acceptability of the model. By the experimental investigation, it can be concluded that an increase in tool nose radius reduces the surface roughness, which corresponds with work done by previous researchers. The developed model can be used to formulate an optimization model to predict the optimum input parameters for a desired response. The integration of modern evolutionary optimization methods with the developed model can be the focus of future research.

Author details

Darshit R. Shah[1] and Sanket N. Bhavsar[2*]

1 L.D. College of Engineering, Ahmedabad, Gujarat, India

2 G.H. Patel College of Engineering and Technology, Vallabh Vidyanagar, Gujarat, India

*Address all correspondence to: sanketbhavsar@gcet.ac.in

References

[1] Niinomi M. Mechanical properties of biomedical titanium alloys. Materials Science and Engineering: A [Internet]. 1998;**243**(1-2):231-236. Available from: http://linkinghub.elsevier.com/retrieve/pii/S092150939700806X

[2] Venkatesh BD, Chen DL, Bhole SD. Effect of heat treatment on mechanical properties of Ti-6Al-4V ELI alloy. Materials Science and Engineering A. 2009;**506**(1-2):117-124

[3] Che-Haron CH, Jawaid A. The effect of machining on surface integrity of titanium alloy Ti-6% Al-4% v. Journal of Materials Processing Technology. 2005; **166**(2):188-192

[4] Sulaiman MA, Che Haron CH, Ghani JA, Kasim MS. Optimization of turning parameters for titanium alloy Ti-6Al-4V ELI using the response surface method (RSM). Journal of Advanced Manufacturing Technology. 2013;7(2): 11-28

[5] Çelik YH, Kilickap E, Güney M. Investigation of cutting parameters affecting on tool wear and surface roughness in dry turning of Ti-6Al-4V using CVD and PVD coated tools. Journal of the Brazilian Society of Mechanical Sciences and Engineering. 2016;**39**(6):2085-2093

[6] Berkani S, Bouzid L, Bensouilah H, Yallese MA, Girardin F, Mabrouki T. Modeling and optimization of tool wear and surface roughness in turning of austenitic stainless steel using response surface methodology [Abstract]. S09d Procédés d'usinage. 2015. pp. 1-16

[7] Valera HY, Bhavsar SN. Experimental investigation of surface roughness and power consumption in turning operation of EN 31 alloy steel. Procedia Technology [Internet]. 2014; **14**:528-534. Available from: http://www.sciencedirect.com/science/article/pii/S2212017314001030

[8] Gosai M, Bhavsar SN. Experimental study on temperature measurement in turning operation of hardened steel (EN36). Procedia Technology [Internet]. 2016;**23**:311-318. Available from: http://linkinghub.elsevier.com/retrieve/pii/S2212017316300330

[9] Chou YK, Song H. Tool nose radius effects on finish hard turning. Journal of Materials Processing Technology. 2004; **148**(2):259-268

Chapter

Characterization of Mold Material for Small Castings

Dixit V Patel and Piyushkumar B Tailor

Abstract

The casting process has a wide scope for manufacturing small parts with sizes in the millimeter range. The commonly used mold materials are not suitable to prepare the mold, which has been used for small castings due to various reasons. The effort has been made here to identify the appropriate ingredients for mold materials for small castings from literature and investigation has been done on their effects on compressive strength and thermal stability, which is most important for small castings. From the experiments, it has been found that a mixture of three ingredients satisfies requirements better when compared to two ingredients for mold material. The combination of 30% α-hemihydrate, 30% water and 40% colloidal silica gives better thermal stability with an appropriate compressive strength.

Keywords: small casting, mold materials, compressive strength, thermal stability

1. Introduction

The casting process has a wide scope for manufacturing small parts such as; gears for watches, small size turbine or wind blade used to produce 5-10 W electricity, various MEMS components and nozzle plates for precision jetting of various liquids and gases [1–3]. Normally in the casting process, the molds are made from sand, plaster of Paris (POP) or gypsum bond investment (GBI) as these materials have a higher surface roughness and mechanical strength [4]. Hence, the castings of millimeter to submillimeter sizes are difficult to remove after solidification from such molds. The preferable casting process for small castings is a centrifugal casting in which compressive force acts on the mold [5]. It means that the mold required for casting a small part should not break during the process under compressive force and should be easily breakable so the small casting can be removed without damage from the mold. Apart from this, obviously it is expected that mold must withstand an elevated process temperature, which means a higher thermal stability [5, 6]. Hence, it is understood that the required characteristics of a mold for small casting are different to a mold for the normal casting process. To explore this domain with scientific background, the initial literature survey has been conducted as follows.

Scheu et al. [7] used POP for making the mold. They have found that POP material has low thermal stability and negligible permeability. However, it is not a favorable condition to cast small parts. Luk and Darvell [8] found that the thermal stability of the mold can be increased by mixing α-hemihydrates powder with a different binder material such as cristobalite, beauty cast, nova cast, and deguvest

california. Earnshaw [9] shows that the ecompressive strength of heated GBI depends mainly on added ingredients and the use of sodium chloride reduces the compressive strength of investments after heating. Ohno et al. [10] show that compressive strength GBI change at higher temperatures due to phase transformation of calcium sulfate and silica. They have also found that α to β transformation of silica does not have considerable effect on compressive strength of GBI. Brien and Nielseen [11] have observed that calcium sulfate did not decompose until 1200°C. They have suggested that GBI material should not be heated above 700°C because it reacts with carbon sulfate that contaminates or makes the casting brittle. Jones [12] has reported that thermal decomposition of GBI starts from 650°C but it is very fast in a temperature range of 900–1000°C. Matsuya and Yamane [13] reported that decomposition began at about 900°C and forms $CaSiO_3$ and Ca_2SiO_4. Rath et al. [14] have demonstrated that 0.5 μm surface finish can be achieved using the molding mixture of 20% fine stone, 80% quartz with 19–30 ml of water, which is lower than the surface roughness of 1.1 μm in the commercial investment cast specimen.

It is understood from the above literature that the mold made from α-hemihydrates, silica and water is more appropriate to cast small parts. The work has been done on a temperature of mold but there is scope in a composition of mold for small castings. Hence, attempt has been made in the present work to investigate the role of ingredients on the compressive strength of the mold as it is important for the success of small castings through the centrifugal casting process. For the better filling and castings, it is preferable to use preheated molds and hence the effect of temperature was also studied.

2. Experiment

2.1 Materials used

The α-hemihydrate fine powder was used as a binder material to achieve a coherent solid mass received from M/S Olympic chemical industry, India. The colloidal silica was received from M/S Lodhika, India and was employed as a filler material as well as to achieve better thermal stability of the mold. Apart from this, the distilled water was used as a chemical modifier. For small castings, it is favorable to use minimal ingredients.

2.2 Measurements and equipment used

The universal testing machine (M/S Fine Spacy Associates and Engineering Pvt. Ltd., India) has a loading capacity of up to 600 kN within +1% accuracy with IS:1828/BS:1010 standard. The compressive strength was measured as per ASTM D395 standards and the specimen had a 1:2 diameter to height ratio. For the small casting, the preheated mold was used to minimize the temperature difference between the molten metal and mold to improve the filling rate of the molten metal into the mold cavity or minimize the shrinkage effect of the cast material. For this reason, the specimen was tested at an elevated temperature by preheating in a muffle furnace (M/S B.S. Pyromatic India Pvt. Ltd., India) with a maximum heating capacity of 1200°C with an accuracy of ±3.0°C temperature.

2.3 Experimental procedure

The best selected binder material, filler material and chemical modifier cannot produce a good casting until they are efficiently and properly mixed and prepared.

Ingredients	Levels (by weight %)
α-hemihydrate	30, 40, 50, 60, 70, 75
Water	25, 30, 40, 50
Colloidal silica	10, 20, 30, 40, 50, 60, 70

Table 1.
Used percentage of ingredient to prepare mixture.

The quality of the mold depends upon the manner in which it is prepared. The specimen as a representative of mold material is prepared from α- hemihydrate, water and colloidal silica of different composition as mentioned in **Table 1**. The ingredients are mixed with a mixture machine for 10 minutes and after that, it was casted in a cylindrical specimen as per ASTM D395 for test. The first combination was made of a binary mixture of α-hemihydrate and water, the second binary was made from α-hemihydrate and colloidal silica, and the third mixture was made from three ingredients i.e. α-hemihydrate, water and colloidal silica and was called the specimen of a tertiary mixture.

3. Result and discussion

The effects of individual ingredients on compressive strength are discussed below.

3.1 Effect of water

As shown in **Figure 1**, it has been found that a reduction in water content from 50 to 30% increased the compressive strength by 22.4% because low water content slurry produced a homogeneous mixture but further reduction of water content reduces the compressive strength by 9.9% because low water content does not encourage the chemical reaction or embedding of the α-hemihydrate powder.

3.2 Effect of colloidal silica

Figure 2 shows that adding colloidal silica to α-hemihydrate decreases the compressive strength of the mold material. The 30% reduction of colloidal silica in a mixture contributed to a 11.6% increase in compressive strength because of the effective chemical reaction with α-hemihydrate powder by the fine quartz particles of colloidal silica.

3.3 Combined effect of water and colloidal silica

It was found that when the mixture contained three ingredients (**Figure 3**) i.e. water, colloidal silica and α-hemihydrate, the compressive strength of the mold material decreased. The compressive strength was found to increase with a higher amount of water content than colloidal silica. When a large amount of colloidal silica was added, the compressive strength of the mold decreased. These factors allowed for the removal of the small castings from the mold without any damage.

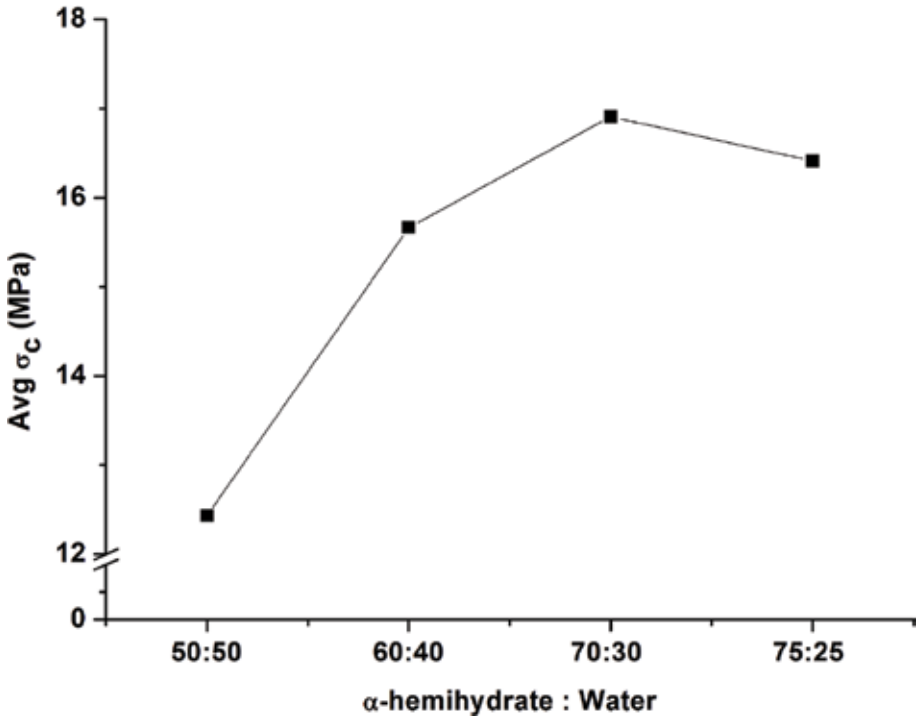

Figure 1.
Effect of water on compressive strength in a binary mixture.

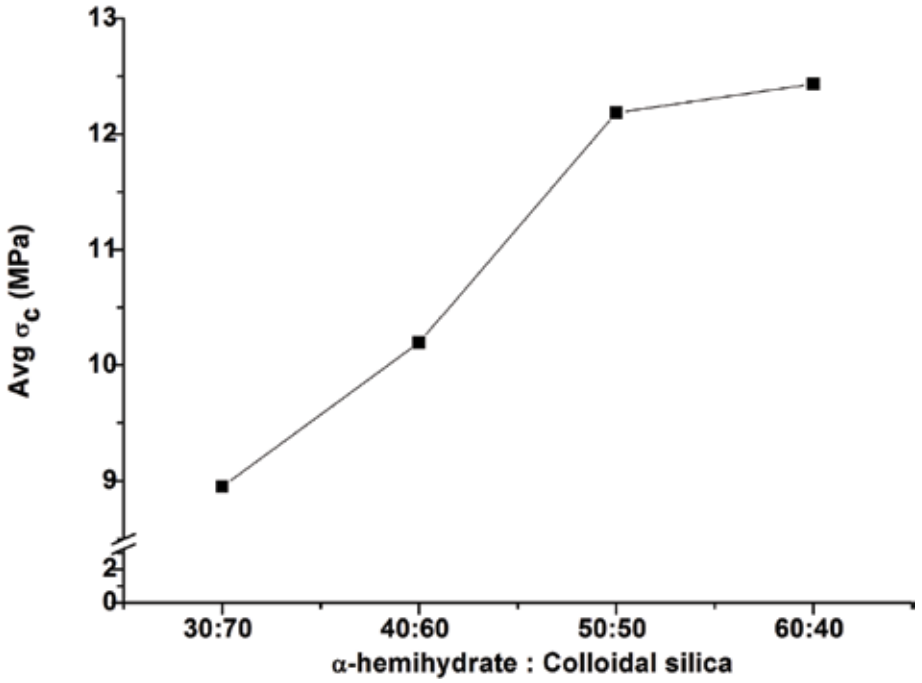

Figure 2.
Effect of colloidal silica on compressive strength in a binary mixture.

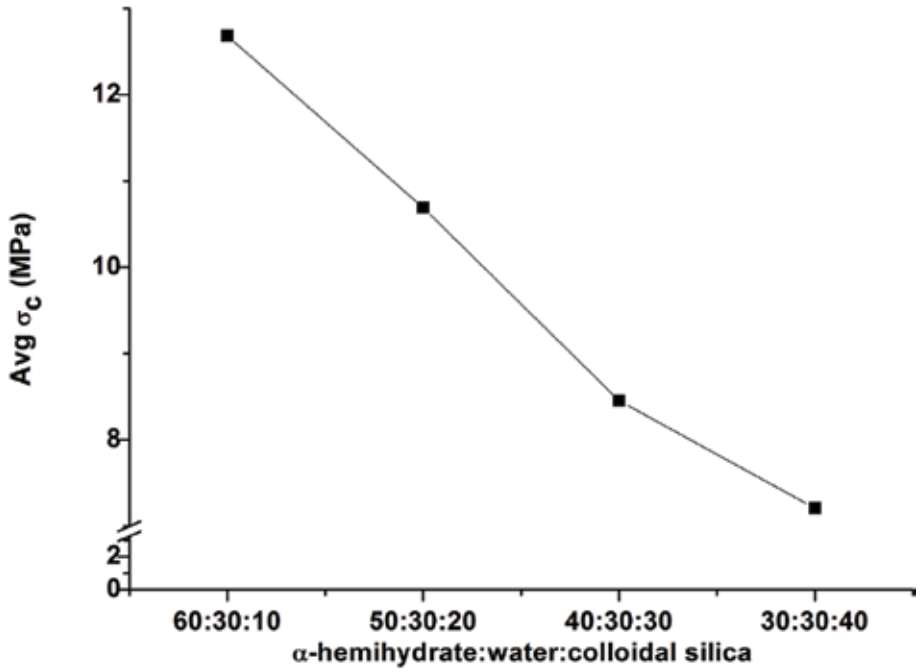

Figure 3.
Combined effect on compressive strength in a tertiary mixture.

3.4 Effect of temperature

During the casting process, the mold has to sustain a high temperature and there should be a small temperature difference between the mold and molten metal as discussed in the introduction section. Hence the effect of temperature on mold material as well as on its compressive strength was investigated.

Through the experiment, it was found that cracks were initiated in a specimen having 60% α-hemihydrate and 40% water from 750°C temperature because of thermal expansion as shown in **Figure 4**. Whereas, as shown in **Figure 5**, the added colloidal silica up to 40% in the mixture increased the heat resistance of the

Figure 4.
60% α-hemihydrate and 40% water content up to 750°C temperature. (a) Before preheating. (b) After preheating.

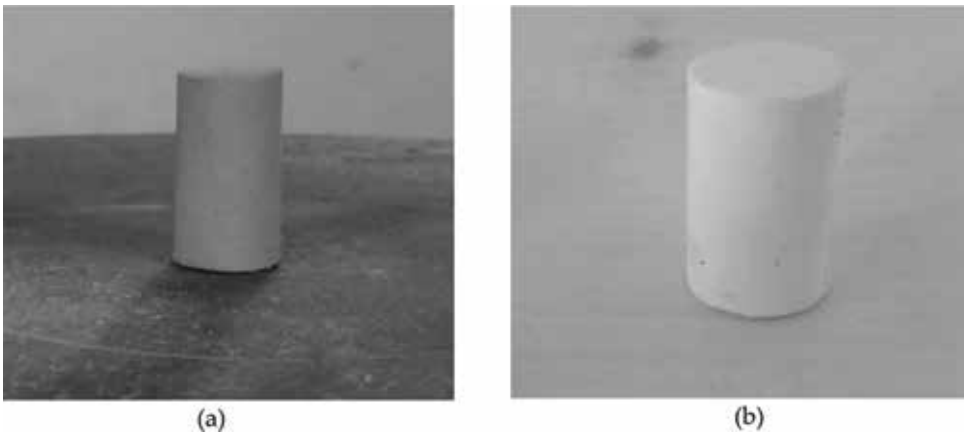

Figure 5.
30% α-hemihydrate, 30% water and 40% colloidal silica up to 900°C temperature. (a) Before preheating. (b) After preheating.

mold material and it could withstand up to 900°C without any cracking. Apart from this, its compressive strength was also comparatively less i.e 7.21 MPa which shows that the percentage ingredients can appropriate for small casting. Hence that has been taken into consideration for further future investigation.

4. Conclusions

The composition of mold material for small castings requires the ability to withstand an appropriate compressive strength and thermal stability particularly when they are made by the centrifugal casting process. The literature also infers that under this circumstance, the composition of mold material should be α-hemihydrate, colloidal silica and water. Based on current work, the following specific conclusions can be derived.

- In case of a binary mixture of mold material, the water or colloidal silica content individually reduces the compressive strength. The 20% water reduces the compressive strength by 22.4%. However, 30% colloidal silica gives a 11.6% reduction.

- The water content promotes homogeneous mixture and colloidal silica collectively gives better thermal stability at the cost of inferior compressive strength in the case of tertiary mixture as compared to binary mixture of mold material.

- It has been found that a combination of 30% α-hemihydrate, 30% water and 40% colloidal silica gives better thermal stability with an appropriate compressive strength.

Author details

Dixit V Patel and Piyushkumar B Tailor*
Sardar Vallabhbhai Patel Institute of Technology, Vasad, India

*Address all correspondence to: piyushkumartailor.mech@svitvasad.ac.in

References

[1] Baumeister G, Rath S, Hausselt J. Microcasting of Al bronze and a gold base alloy improved by plaster-bonded investment. Microsystem Technologies. 2006;**12**:773-777. DOI: 10.1007/s00542-006-0105-3

[2] Ruprecht R, Benzler T, Hanemann T, Müller K, Konys J, Piotter V, et al. Various replication techniques for manufacturing three-dimensional metal microstructures. Microsystem Technologies. 1997;**4**:28-31

[3] Baumeister G, Buqezi-Ahmeti D, Glaser J, Ritzhaupt-Kleissl H-J. New approaches in microcasting: Permanent mold casting and composite casting. Microsystem Technologies. 2011;**17**: 289-300. DOI: 10.1007/s00542-011-1237-7

[4] Baumeister G, Ruprecht R, Hausselt J. Microcasting of parts made of metal alloys. Micro System Technologies. 2004;**10**:261-264. DOI: 10.1007/s00542-003-0363-2

[5] Baumeister G, Ruprecht R, Hausselt J. Replication of LIGA structures using microcasting. Microsystem Technologies. 2004;**10**:484-488. DOI: 10.1007/s00542-004-0377-4

[6] Chuang Y, Li B-S, Ming-xing R, Heng-zhi FU. Micro precision casting based on investment casting for microstructure with high aspect ratio. Transactions of Nonferrous Metals Society of China. 2009;**19**:521-525

[7] Scheu CH. Precision casting utilizing the hygroscopic action of plaster in investment in making expanded molds. The Journal of the American Dental Association. 1933;**20**:1205-1215

[8] Luk WK, Darvell BW. Effect of burnout temperature on strength of gypsum-bonded investments. Dental Materials. 2003;**19**:552-557. DOI: 10.1016/s0109-5641(02)00104-5

[9] Earnshaw R. The compressive strength of gypsum-bonded investments at high temperatures. Australian Dental Journal. 1969;**14**:264-268

[10] Ohno H, Nakano S, Miyakawa O, Watanabe K, shiokawa N. Effects of phase transformations of silicas and calcium sulfates on the compressive strength of gypsum-bonded investments at high temperatures. Journal of Dental Research. 1982;**61**:1077-1082

[11] O'Brien WJ, John P. Decomposition of gypsum investment in the presence of carbon. Journal of Dental Research. 1959;**38**:541-547

[12] Jones DW. Thermal analysis and stability of refractory investments. The Journal of Prosthetic Dentistry. 1967;**18**:234-241

[13] Matsuya S, Yamane M. Decomposition of gypsum bonded investments. Journal of Dental Research. 1981;**60**:1418-1423. DOI: 10.1177/00220345810600080501

[14] Rath S, Baumeister G, Hausselt J. Investments for casting micro parts with base alloys. Micro System Technologies. 2006;**12**:258-266. DOI: 10.1007/s00542-005-0047-1

Chapter

A Review for Feed Rate Optimization of Spiral Tool Path Using Cutter Engagement Angle and Step Over

Shriprakash V. Dwivedi and Divyangkumar D. Patel

Abstract

2.5D pocket machining is extensively used in aerospace, shipyard, automobile, dies and mold industries. In machining of 2.5D pockets, conventional toolpath strategies, such as directional parallel tool path and contour parallel tool path, are generally used. However, these tool paths greatly limit the machining performance in terms of machining time, surface finish and tool wear because of repeated machining direction alteration, stop-and-go motion, sharp velocity discontinuity, and frequent repositioning, retraction, acceleration and deceleration of the tool. To overcome the above-mentioned problems of conventional tool path strategies, many tool path strategies are proposed of which spiral tool path is most widely used. The spiral tool path provides an efficient way to produce a pocket, but it suffers from some problem such as bottleneck in a narrow region, variation in step over and cutter engagement angle (hence, change in cutting load), etc. This change in cutting load affects surface roughness. Hence, a review for feed rate optimization of spiral tool path using cutter engagement angle and step over is discussed.

Keywords: pocket machining, cutter engagement angle, step over, feed rate optimization, spiral tool path, high speed machining (HSM)

1. Introduction

Generally, the material inside a closed region on a flat surface of a workpiece is removed up to a fixed depth using flat bottom end mills in pocket machining. Roughing operation is done to cut the volume of material at the initial stage and after that the pocket is finished by a finish end mill. Most of the industrial milling operations (up to 80%) can be machined by 2.5D CNC milling [1]. Pocket machining (**Figure 1**) refers to making an inner empty volume starting from a workpiece face. The created empty volume is known as a pocket. A cutter refers to a milling cutter that is used to create a pocket on the workpiece. It also can be seen that the material is removed from stock, layer by layer until pockets are formed and a manufactured part emerges [2].

Feed or feed rate is the "relative velocity at which the cutter advances into the workpiece and in a given direction", which is measured in millimeters per minute (mm/min), or inches per minute (in/min). Step over as shown in **Figure 2** is a

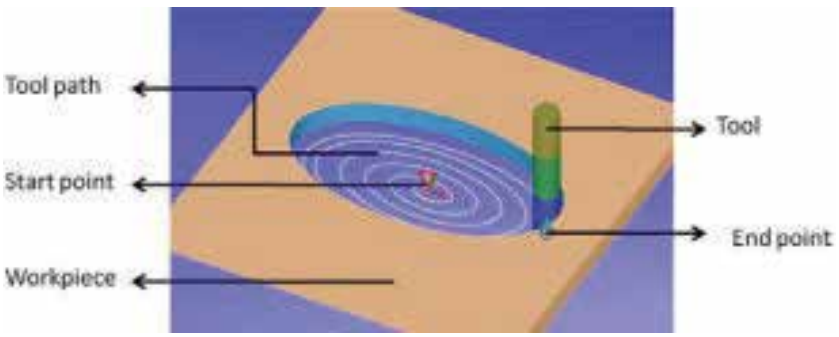

Figure 1.
Representation of pocket machining [3].

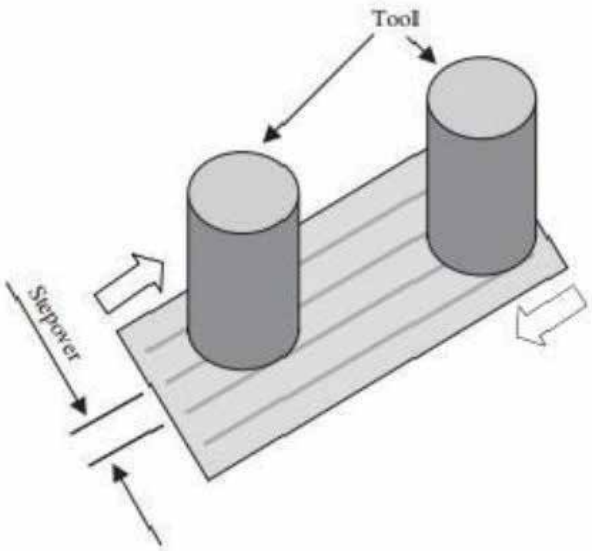

Figure 2.
The term step over [4].

milling parameter that is defined as "the distance between two neighboring passes over the workpiece". Step over is also used to calculate the number of tools being passed and cut again on a finished surface [4]. Cutter engagement angle (α) is defined as the "angle which spans the part of the tool surface that performs cutting" as shown in **Figures 3** and **4** [5]. **Figure 4** shows that the cutter engagement angle varies depending on the availability of tool path and shape of pocket required.

The spiral tool path starts as a spiral from the center of pocket geometry and takes the shape of the pocket boundary. The spiral tool path strategy is expected to machine pocket with lower tool path length, lower machining time, less tool wear, capacity to extract the material at corners, the capability of a tool path to reduce variation in step over, etc. The machining parameters such as feed, speed, depth of cut, tool path strategy, step over, engagement angle, etc., affect machining time, surface roughness, tool wear, accuracy and efficiency of the tool path so the selection of these parameters is important and it should be precisely selected and controlled.

High speed pocket machining (HSM) is described as end milling with small diameter tools (less than 10 mm) at a high rotational speed (greater than 10,000 rpm) and power is greater than 10 HP compared to conventional techniques.

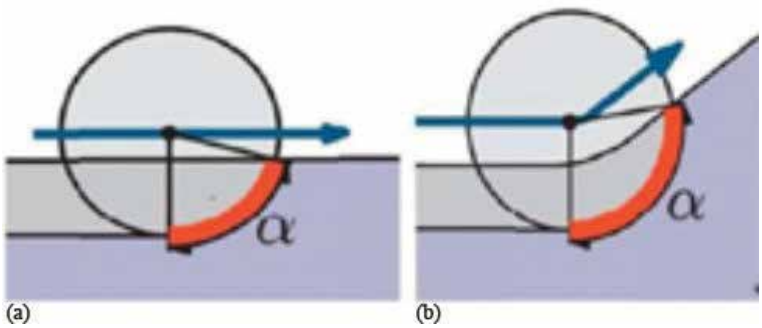

Figure 3.
(a) Straight segment of the tool path (b) Curved segment of the tool path with cutter engagement angle (α) [5].

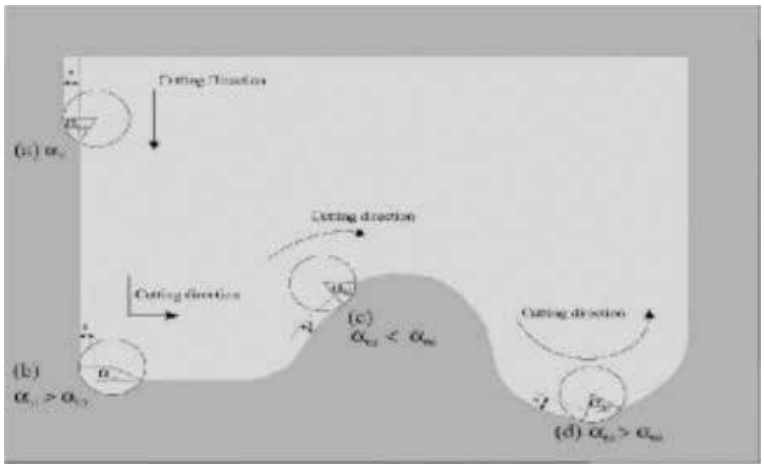

Figure 4.
Changes of cutter engagement angle (α) at different tool motions [6].

1.1 Advantages of high speed pocket machining

- Higher material removal rate.
- Less machining time required compared to conventional machining.
- It can be used to machine any complex shape.
- The accuracy of pockets can be increased by selecting appropriate tool path strategies.
- Less tool wear leads to longer tool life.

1.2 Limitations of high speed pocket machining

- Appropriate selection of tool path strategies is crucial.
- High speed machining center is required.
- Cost is high compared to conventional machining.

2. Literature review

Bieterman and Sandstrom have described a novel curvilinear tool path generation method but it is not suitable for pockets that are too concave. They showed experimentally that morphing leads to reductions in tool wear when cutting hard metals and machining time up to 30% in cutting all metals [2]. Topal and Eyüp Sabri have showed the role of the step over ratio in surface roughness prediction studies. It was found that surface roughness values are influenced by step over and it could not be possible to predict the surface roughness precisely without considering step over [4]. Held, Martin and Christian Spielberger proposed a geometric heuristic to disintegrate an arbitrarily complex pocket with or without an island into uncomplicated sub-pockets by considering cutter engagement angle and step over for acceptable tool path for efficient spiral high-speed machining. They showed that pocket disintegration improved quality parameters, improvement in step over variation, the maximum slope of the engagement angle and the tool path length [5]. Kloypayan, Jirawan and Yuan-Shin Lee have presented a technique for analyzing the material removal rate when a tool moves in linear, circular or parametric curved motions. They showed that optimal material removal rate is obtained by increasing the feed rate in the ball end milling process [6].

Gupta et al. suggested a geometric algorithm described for computing piecewise stable closed-form cutter engagement functions for 2.5D milling operations to determine an efficient cutter path and to improve it. Further results are compared with discrete simulations which showed that cutter engagement angle increases in circular cuts and linear half-spaces of the same [7]. Dharmendra and Lalwani created a spiral tool path of elliptical pockets for CNC machine using PDE. It was found that machining time depends on the ratio of the major to minor axis of the elliptical pocket and tool path length also increased [8]. Further, they carried out an investigation on AISI SS material using a spiral tool path for elliptical pockets. They reported that tool path length, tool utilization, machining time and surface roughness etc. was affected by variation in the shape of pockets and different tool path strategies [3].

Stori and Wright proposed a generative spiral-in algorithm for 2.5D material removal of convex geometries. It was found that there were decreased changes in cutting forces during cornering and pocketing application [9]. Kaymakci et al. found that the cutting forces for complicated sculptured surfaces can be forecast precisely using new forced based feed rate scheduling strategy. It was validated experimentally that the cycle time of sculptured surface machining is reduced up to 38.1% greatly with forced based feed scheduling strategy [10]. Bae et al. proposed an automatic feed rate adjustment method for cutting force model, they showed that cutting load and feed rate can be easily determined without any computations [11]. Chen et al. proposed the feed rate optimization of the high-speed ball end milling process. It was found that the feed-interval scallop height limits the feed rate for high efficient machining with use of advanced tool technology and if the specifications of the notch cut profile can be optimized then the feed rate can be increased more [12].

Dong et al. investigated the chances of scheduling or changing the feed rate by considering the geometry of the contour. By regulating the magnitude of cornering errors, the different jerk constraints were fixed [13]. Gong and Feng invented a new method to resolve the cutter workpiece engagement for general milling processes which were validated by a series of case studies of increasing machining complexity to indicate its usability to general milling processes [14]. Ko and Cho invented an analytical model of off-line feed rate scheduling to resolve desired feed rates for 3D ball-end milling. It was found that the presented feed rate scheduling model

decreased machining time with more accuracy [15]. Merdol and Altintas presented the modeling of process simulation in a potential environmental and computationally effective algorithm for optimal selection of machining specifications while considering process constraints and changes in the part geometry along the tool path. Results showed a maximum material removal rate and productivity without affecting torque, power, and tool deflection limits [16].

Uddin et al. invented a new tool path modification plan for constant engagement with a workpiece in 2.5D end milling. Machining results were analyzed and results showed that this plan can increase the machining accuracy related to feeding rate control strategies [17]. Tounsi and Elbestawi suggested an optimized feed scheduling approach increasing the metal removal rate in 3-axis machining while assuring the machining accuracy. It had been concluded that this approach gives great adjustment of the cutting force and develops the reference tool locations for a given tool path [18]. Desai et al. suggested a technique to minimize surface error variation due to engagement changed in pocket end milling by adjusting machining approach for the curved components. It was observed that the suggested technique is quite effective for reducing the variation in surface error [19]. Pateloup et al. suggested a method to minimize machining time and tool path advancement by adjusting the corner radius using computer-aided manufacturing system. It was concluded that the use of B-spline for the tool path calculation is a significant advancement related to lines and arcs [20].

3. Conclusions

Many researchers have studied work on pocket machining with an aim to improve the process in terms of surface quality, the accuracy of pockets and machining time. 2.5D pocket machining has proved to be an efficient process for high-speed machining. After a detailed investigation of the published work, the following conclusions were developed from the existing published work:

- Most of the research focused on a 2.5D pocket machining as well as high-speed machining.
- Feed rate and cutter engagement angle are the most dominating factors that affect surface roughness, cutting load, tool wear while machining of 2.5D pocket on HSM.
- Also, it was found that the spiral tool path helps to reduce step over variation, machining time and increase the tool life etc.
- Very scarce amount of work is reported on feed rate optimization of spiral tool path using cutter engagement angle and step over.

DOI: http://dx.doi.org/10.5772/intechopen.81083

Author details

Shriprakash V. Dwivedi* and Divyangkumar D. Patel
Sardar Vallabhbhai Patel Institute of Technology, Vasad, India

*Address all correspondence to: shriprakash527@gmail.com

References

[1] Choy H, Chan K. A corner-looping based tool path for pocket milling. Computer-Aided Design. 2003;**35**(2):155-166

[2] Bieterman MB, Sandstrom DR. A curvilinear tool-path method for pocket machining. In: ASME 2002 International Mechanical Engineering Congress and Exposition. American Society of Mechanical Engineers; 2002

[3] Patel DD, Dodiya HR, Lalwani D. Experimental investigation of CNC machining of elliptical pockets on AISI 304 stainless steel. International Journal of Experimental Design and Process Optimisation. 2016;**5**(1-2):94-116

[4] Topal ES. The role of stepover ratio in prediction of surface roughness in flat end milling. International Journal of Mechanical Sciences. 2009;**51**(11):782-789

[5] Held M, Spielberger C. Improved spiral high-speed machining of multiply-connected pockets. Computer-Aided Design and Applications. 2014;**11**(3):346-357

[6] Kloypayan J, Lee Y-S. Material engagement analysis of different endmills for adaptive feedrate control in milling processes. Computers in Industry. 2002;**47**(1):55-76

[7] Gupta SK et al. Geometric algorithms for computing cutter engagement functions in 2.5 D milling operations. Computer-Aided Design. 2005;**37**(14):1469-1480

[8] Dharmendra PD, Lalwani D. A spiral toolpath for machining of elliptical pockets using partial differential equation. Materials Today: Proceedings. 2015;**2**(4-5):3394-3402

[9] Stori J, Wright P. Constant engagement tool path generation for convex geometries. Journal of Manufacturing Systems. 2000;**19**(3):172-184

[10] Kaymakci M, Lazoglu I, Murtezaoglu Y. Machining of complex sculptured surfaces with feed rate scheduling. International Journal of Manufacturing Research. 2006;**1**(2):157-175

[11] Bae S-H et al. Automatic feedrate adjustment for pocket machining. Computer-Aided Design. 2003;**35**(5):495-500

[12] Chen J-SB, Huang Y-K, Chen M-S. Feedrate optimization and tool profile modification for the high-efficiency ball-end milling process. International Journal of Machine Tools and Manufacture. 2005;**45**(9):1070-1076

[13] Dong J, Ferreira P, Stori J. Feed-rate optimization with jerk constraints for generating minimum-time trajectories. International Journal of Machine Tools and Manufacture. 2007;**47**(12):1941-1955

[14] Gong X, Feng H-Y. Cutter-workpiece engagement determination for general milling using triangle mesh modeling. Journal of Computational Design and Engineering. 2016; **3**(2):151-160

[15] Ko JH, Cho D-W. Feed rate scheduling model considering transverse rupture strength of a tool for 3D ball-end milling. International Journal of Machine Tools and Manufacture. 2004;**44**(10): 1047-1059

[16] Merdol SD, Altintas Y. Virtual simulation and optimization of milling applications—part II: Optimization and feedrate scheduling. Journal of Manufacturing Science and Engineering. 2008;**130**(5):051005

[17] Uddin MS et al. Constant engagement tool path generation to enhance machining accuracy in end milling. JSME International Journal. Series C, Mechanical Systems, Machine Elements and Manufacturing. 2006;**49**(1):43-49

[18] Tounsi N, Elbestawi M. Optimized feed scheduling in three axes machining. Part I: Fundamentals of the optimized feed scheduling strategy. International Journal of Machine Tools and Manufacture. 2003;**43**(3):253-267

[19] Desai K, Rao P. Machining of curved geometries with constant engagement tool paths. Proceedings of the Institution of Mechanical Engineers, Part B: Journal of Engineering Manufacture. 2016;**230**(1):53-65

[20] Pateloup V, Duc E, Ray P. Corner optimization for pocket machining. International Journal of Machine Tools and Manufacture. 2004;**44**(12):1343-1353

Chapter

A Review on Carbon Nanotube-Based Dry Electrode for EEG Recording

Parmar Prashant and Anand Joshi

Abstract

The electroencephalography (EEG) is the way that the brain communicates with a computer and electronic devices also referred to as a mind-machine interface (MMI) or a brain-machine interface (BMI). Human organs such as the brain, heart and muscles producing μV to mV biopotential which can be measured through electroencephalography (EEG), electrocardiography (ECG) and electromyography (EMG) respectively. With the advancement in electronics, microelectromechanical manufacturing and biocompatible material, controlling of electronic actuating devices has become an area of great research interest. The EEG signal is captured by an electrode which is either classified as a dry and wet electrode. This study focuses on a new emerging field of dry EEG electrode design with a carbon nanotube (CNT) as the sensing material. Clinical research has proved that CNT does not have cause any skin allergic and irritation effects when compared to wet electrodes, which use a conductive gel that has an adverse effect on the skin in the long-term. The multiwall CNT is used with conductive polymers with a variation in electrode design aspects such as shape, size, thickness, microneedle array and amount of CNT in composition with the conductive polymer. In this article, the quality of the acquired EEG signal is discussed based on variations of the above-mentioned design aspects.

Keywords: electroencephalography, carbon nanotube, conductive polymer, EEG electrodes, microelectromechanical system

1. Introduction

There is rapid growth in medical electronic devices in the wearable health monitoring system such as wheelchair control, robotic prosthetic arm, brain disease, virtual reality and augmented reality etc. [1–4]. In medical diagnosis, biopotentials, such as an electroencephalogram (EEG) from brain, electromyogram (EMG) from muscles, and electrocardiogram (ECG) from heart are commonly used techniques to measure the electrical activity also termed as electrophysiology. Currently, the signal is captured from the outer layer of skin with the help of hydrolytic gel and an Ag/AgCl electrode. The hydrolytic gel becomes dehydrated on long-term measurement which adds noise as well as deteriorates signal quality [5, 6]. Moreover, this conductive gel can cause skin irritation and allergic effects. To overcome this issue, the need arose to develop a dry EEG electrode having long-term signal acquisition

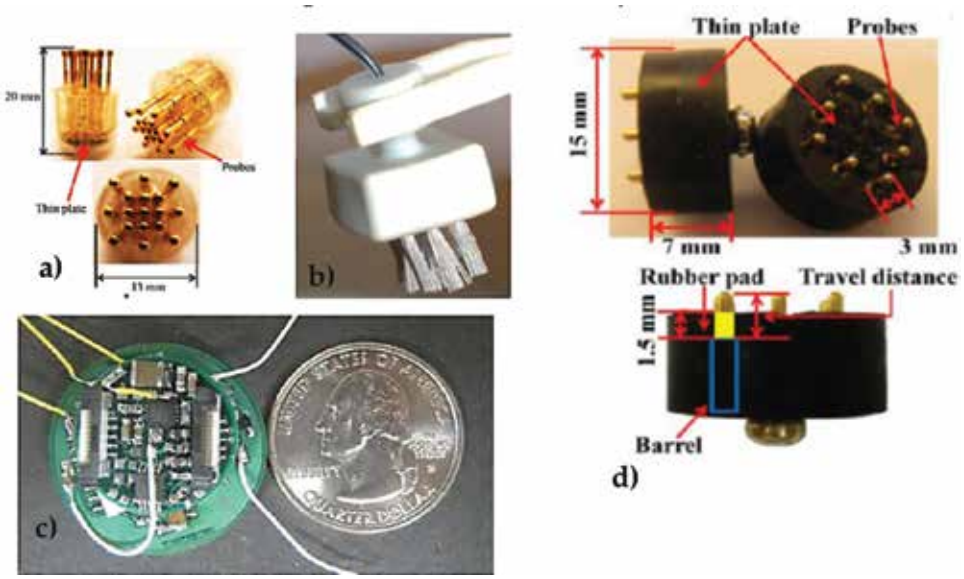

Figure 1.
Various EEG electrodes (a) spring loaded dry electrode [9], (b) bristle type dry electrode [10], (c) nano contact type dry electrode [11], (d) dry sensor electrode [12].

stability with minimum noise. Earlier, some dry electrode were proposed with sensing material such as gold, silver, Ti/TiN, iridium oxide (IrO), platinum, tin, stainless steel etc. [7, 8]. The focus of researchers was on the design of the sensing part of the EEG electrode (**Figure 1**) [9–12]. To match the scalp skin curve and to minimize the effect of motion artifacts, screen-printed electrodes were also proposed and results showed that they were less prone to motion artifacts and noise [13, 14]. It was found that the carbon nanotube does not cause any skin irritation or allergic effects [15]. The carbon nanotube is a nanomaterial because of its excellent physical and chemical property and is now popular in medical field [16, 17]. Mostly, polydimethylsiloxane (PDMS), epoxy-based PTF silver ink (XCMS-015), polypyrrole (PPy) polythiophene (PTh) etc., is used to create the conductive matrix along with CNT. CNTs are also used for the coating material to improve the electrical conductivity [18, 19]. There are several CNT based electrode designs such as a micro-needle array, ENOBIO, CNT/PDMS, vertical CNT, polypyrrole (PPy) conductive polymer coating of dry patterned vertical CNT (pvCNT), self-adhesive and capacitive, and skin like CNT [4, 20–25]. In this article, the design, fabrication and response of this type of electrode will be discussed.

2. Electrode design

2.1 Electrode standard

International Federation of Clinical Neurophysiology (IFCN) [26] has standardized 16 channels as a minimum requirement for satisfactory results.

To acquire signal, the electrode-position has a letter F, T, C, P and O, which stand for frontal, temporal, central, parietal, and occipital lobes, respectively as per 10–20 system [26]. The electrode should be provided with reference and electronics grounding. Furthermore, the digital sampling rate should be 200 samples/s, minimum resolution of at least 12 bits and must have minimum steps of 0.5 mV,

minimum electrode impedances below 5 kΩ. Any other noise in the recording should be less than 1.5 mV peak-to-peak and 0.5 mV root-mean-square at any frequency from 0.5–100 Hz including 50–60 Hz [26].

2.2 Coating type dry electrode design

The electrode with application of the multiwall carbon nanotube (MWCNT) was tested on a pig and then human with an aim to eliminate the application of skin preparation, conductive gel and improve wearability [20, 27]. This electrode penetrates inside the outer layer of skin called the Stratum Corneum (SC). Here, two designs were proposed: first, non-polarized with a silver/silver chloride (Ag/AgCl) coating and, second, polarizable electrode without coating the MWCNT with a diameter of ca. 50 nm and length 20–30 μm. A vertical aligned CNT on Parylene-C polymer substrate was used to acquire a signal from the crayfish nerve cord. The electrode was fabricated with the chemical vapor deposition technique and proposed in [28]. Similar to conventional electrode design and ready to plug with existing EEG device, a CNT/PDMS wearable monitoring device was proposed in [21]. The MWCNT with 1–25 μm length had a 93% purity. Ultra-flexible micro-ECoG poly (ethylenedioxythiophene) PEDOT-CNT coated electrodes were introduced by [18]. In this technique, the signal was acquired from the below the scalp skin and this classifies as an invasive method of EEG recording. In this experiment, a 4 μm thick polyimide was deposited on a silicon wafer. A 20 nm thick titanium layer was added onto polyimide then 200 nm thick gold (Au) file placed over titanium. Finally, a 20 nm thick chromium (Cr) layer was used to cover the underlying metal. Through the lithography process, the 100 μm × 100 μm pad was obtained. For a hairy scalp, a self-adhesive and capacitive carbon nanotube based electrode design proposed [4]. The electrode consists of mainly three layers namely solderable metal Ti/Au, PDMS polymer as a middle ring and CNT/aPDMS sensing layer. The high conductive CNT/aPDMS sensing material has an adhesive property as well as being flexible in shape. It is adjusted on the hair and decreases the electrode-skin impedance.

Another research group designed CNT and adhesive PDMS matrix and recorded alpha rhythm steady state to evoke potential and auditory steady state response. They proposed an electrode with three layers—bottom aPDMS layer comes in contact with skin while CNT/aPDMS is the middle layer and Au/Ti/polyimide is the upper layer [24]. A research group [23] proposed a novel dry electrode where a vertical MWCNT was coated by polypyrrole (PPy) conductive polymer. This coated pillar was placed over a stainless steel foil of ϕ10mm. The CNTs with 1–1.5 mm growth taken at the space interval of 50, 100 and 200 μm.

2.3 Conductive polymer

Most of the proposed electrodes for EEG, ECoG, ECG etc., use Parylene-C, polydimethylsiloxane (PDMS), poly-ethylenedioxythiophene (PEDOT), polyimide and polypyrrole (PPy) as conductive polymers [4, 18, 21, 23, 24, 28]. This is mainly due to the flexibility, high conductivity and biocompatibility and these materials have been used for vision prosthesis [29], neural prosthetic and neural interface [30, 31], and microneedle type sensing for neural interface.

3. Electrode response discussion

The alpha waves (8–12 Hz) and β waves (15–30 Hz) were recorded at position Fp2 with limited trails and they found less noisy signal compared to a wet electrode.

A flexible CNTs electrode [28] received signal from a crayfish nerve cord with a 1 kHz frequency at 11.07 kΩ impedance which falls under the typical EEG recording. The result shows that CNTs and polymer matrix-based electrodes adhered along the bio-tissue for long-term recording. The research group noticed that CNT based electrodes had low impedance values when compared to Au or Pt based micro fabricated electrodes as well as smaller plastic capacitance. CNT/PDMS electrodes [21] with variation in CNT/PDMS composition, electrode thickness and diameter for a long-term wearable application were designed with samples 1, 1.5, 2 and 4.5 wt% CNTs in composition and 1, 2 and 3 mm variation in thickness while 20, 30, 40 mm variation in diameter. It was concluded through an electrical conductivity test that the conductivity of the electrode depends on the CNTs concentration. The proposed design was adjustable to current EEG setup by replacing the wet electrode. The results noticed that there was a negligible effect of electrode thickness on quality of ECG signal. Furthermore, the signal quality was increased with high wt% of CNTs.

The commercially available Ag/AgCl electrode is prone to motion artifact due to high skin-electrode impedance and this can be avoided using CNTs based electrodes. Further, another research group did a study on the effect of the vertically aligned CNTs electrode [22] on ECG signal and found similar results. Here, the CNTs were vertically deposited on the stainless steel material with 50, 100, 200 and 500 μm spacing. It has been noted that the impedance remained stable over the period of time in the pvCNT type electrode. The same design was improved by coating the electrode with the electrically conductive polymer (PPy) to increase the bonding strength with a substrate. To record the EEG signal from the hairy scalp is a challenging task as the presence of hair and air will increase the skin-electrode impedance and will result in degradation of signal quality. For this challenge, a self-adhesive and capacitive electrode design proposed in [4]. The alpha and steady-state evoke potential acquired by placing a dry electrode close to a wet electrode, the reference and ground electrodes placed at A2 and Fpz location respectively. The electrode was fabricated with 2.5 mm height and 3 mm diameter, on applying gentle pressure, its CNT/aPDMS layer filled the air gap and comes in contact with the skin even in the presence of hairs. Signal to noise ratio was recorded 3.71 ± 0.17 dB, the same aspect was noted 2.79 ± 0.13 dB in aPDMS without CNT. The signal quality was found to be good when compared with a wet electrode including an effect of motion artifacts.

4. Conclusion

All the proposed designs and results of CNTs indicate that it can be used as a substitute for a wet electrode to avoid the skin irritation and allergic effects without compromising signal quality. Through CNT/PDMS, ECG electrode signals were successfully taken for 7 days without degradation, which also shows that CNTs do not cause allergy and irritation on the skin like wet electrode [21]. This electrode can be reused after cleaning with alcohol, which reduces the cost as compared to wet electrodes are disposed once gel drys or evaporates. Also, Ag/AgCl electrodes signal quality deteriorates as sweat affects the gel. Moreover, through the cytotoxicity test it was found that this design was suitable for long-term ECG monitoring due to biocompatibility. The micro-ECOG design [18] proved that electro-chemically PEDOT-CNT nanocoatings are suitable for *in vivo* application to record signal from rat somatosensory cortexes via multi-whisker deflections. Furthermore, Platinum (Pt) electrodes coated with bioactive PEDOT [29] coatings can be applied to both vision prostheses and a wide range of other neuroprosthetic implants, which also

help to study biocompatibility of conductive polymers. Most of these studies were carried out on volunteers below 35 years of age, a future scope is to test it on elderly people. These results show that in future there is scope for further experiments on CNTs and conductive polymer matrix application for human neural compatibility and commercialization.

Author details

Parmar Prashant[1]* and Anand Joshi[2]

1 TeamLease Skills University, Vadodara, India

2 G. H. Patel College of Engineering and Technology, Vallabh Vidyanagar, India

*Address all correspondence to: prashant.parmar@teamleaseuniversity.ac.in; anandjoshi@gcet.ac.in

References

[1] Cangelosi A, Invitto S. Human-robot interaction and neuroprosthetics: A review of new technologies. IEEE Consumer Electronics Magazine. 2017;**6**:24-33. DOI: 10.1109/MCE.2016.2614423

[2] Yu Y, Zhou Z, Liu Y, Jiang J, Yin E, Zhang N, et al. Self-paced operation of a wheelchair based on a hybrid brain-computer interface combining motor imagery and P300 potential. IEEE Transactions on Neural Systems and Rehabilitation Engineering. 2017;**25**:2516-2526. DOI: 10.1109/TNSRE.2017.2766365

[3] McMullen DP, Hotson G, Katyal KD, Wester BA, Fifer MS, McGee TG, et al. Demonstration of a semi-autonomous hybrid brain–machine interface using human intracranial EEG, eye tracking, and computer vision to control a robotic upper limb prosthetic. IEEE Transactions on Neural Systems and Rehabilitation Engineering. 2014;**22**:784-796. DOI: 10.1109/TNSRE.2013.2294685

[4] Lee SM, Kim JH, Park C, Hwang JY, Hong JS, Lee KH, et al. Self-adhesive and capacitive carbon nanotube-based electrode to record electroencephalograph signals from the hairy scalp. IEEE Transactions on Biomedical Engineering. 2016;**63**: 138-147. DOI: 10.1109/TBME.2015.2478406

[5] Xu J, Mitra S, Van Hoof C, Yazicioglu RF, Makinwa KAA. Active electrodes for wearable EEG acquisition: Review and electronics design methodology. IEEE Reviews in Biomedical Engineering. 2017;**10**:187-198. DOI: 10.1109/RBME.2017.2656388

[6] Kappel SL, Kidmose P. Study of impedance spectra for dry and wet EarEEG electrodes. In: 2015 37th Annual International Conference of the IEEE Engineering in Medicine and Biology Society (EMBC); 2015; pp. 3161-3164. DOI: 10.1109/embc.2015.7319063

[7] Albulbul A. Evaluating major electrode types for idle biological signal measurements for modern medical technology. Bioengineering (Basel). 2016;**3**:1-10. DOI: 10.3390/bioengineering3030020

[8] Tallgren P, Vanhatalo S, Kaila K, Voipio J. Evaluation of commercially available electrodes and gels for recording of slow EEG potentials. Clinical Neurophysiology. 2005;**116**:799-806. DOI: 10.1016/j.clinph.2004.10.001

[9] Liao LD, Wang IJ, Chen SF, Chang JY, Lin CT. Design, fabrication and experimental validation of a novel dry-contact sensor for measuring electroencephalography signals without skin preparation. Sensors (Basel). 2011;**11**:5819-5834. DOI: 10.3390/s110605819

[10] Grozea C, Voinescu CD, Fazli S. Bristle-sensors—Low-cost flexible passive dry EEG electrodes for neurofeedback and BCI applications. Journal of Neural Engineering. 2011;**8**:025008. DOI: 10.1088/1741-2560/8/2/025008

[11] Sullivan TJ, Deiss SR, Cauwenberghs G. A low-noise, non-contact EEG/ECG sensor. In: 2007 IEEE Biomedical Circuits and Systems Conference. 2007. pp. 154-157. DOI: 10.1109/BIOCAS.2007.4463332

[12] Liao LD, Wu SL, Liou CH, Lu SW, Chen SA, Chen SF, et al. A novel 16-channel wireless system for electroencephalography measurements with dry spring-loaded sensors. IEEE Transactions on Instrumentation and

Measurement. 2014;**63**:1545-1555. DOI: 10.1109/TIM.2013.2293222

[13] Lepola P, Myllymaa S, Töyräs J, Muraja-Murro A, Mervaala E, Lappalainen R, et al. Screen-printed EEG electrode set for emergency use. Sensors and Actuators A: Physical. 2014;**213**:19-26. DOI: 10.1016/j.sna.2014.03.029

[14] Myllymaa S, Lepola P, Hukkanen T, Õun A, Mervaala E, Töyräs J, Lappalainen R, Myllymaa K. Novel screen printed electrode set for routine EEG recordings in patients with altered mental status. In: 2013 35th Annual International Conference of the IEEE Engineering in Medicine and Biology Society (EMBC); 2013. pp. 6724-6727. DOI: 10.1109/embc.2013.6611099

[15] Huczko A, Lange H. Carbon nanotubes: Experimental evidence for a null risk of skin irritation and allergy. Fullerene Science and Technology; 2001;**9**:247-250. DOI: 10.1081/FST-100102972

[16] Niyogi S, Hamon MA, Hu H, Zhao B, Bhowmik P, Sen R, et al. Chemistry of single-walled carbon nanotubes. Accounts of Chemical Research. 2002;**35**(12):1105-1113. DOI: 10.1021/ar010155r

[17] Zhang Y, Bai Y, Yan B. Functionalized carbon nanotubes for potential medicinal applications. Drug Discovery Today. June 2010;**15**:428-435. DOI: 10.1016/j.drudis.2010.04.005

[18] Castagnola E, Maiolo L, Maggiolini E, Minotti A, Marrani M, Maita F, et al. PEDOT-CNT-coated low-impedance, ultra-flexible, and brain-conformable micro-ECoG arrays. IEEE Transactions onNeural Systems and Rehabilitation Engineering. 2015;**23**:342-350. DOI: 10.1109/tnsre.2014.2342880

[19] Charkhkar H, Knaack GL, Mandal HS, Keefer EW, Pancrazio JJ. Effects of carbon nanotube and conducting polymer coated microelectrodes on single-unit recordings in vitro. Conference of the IEEE Engineering in Medicine and Biology Society. 2014;**2014**:469-473. DOI: 10.1109/embc.2014.6943630

[20] Ruffini G, Dunne S, Farres E, Cester I, Watts PC, Silva SP, et al. ENOBIO dry electrophysiology electrode; first human trial plus wireless electrode system. Conference of the IEEE Engineering in Medicine and Biology Society. 2007;**2007**:6690-6694. DOI: 10.1109/IEMBS.2007.4353895

[21] Jung HC, Moon JH, Baek DH, Lee JH, Choi YY, Hong JS, et al. CNT/PDMS composite flexible dry electrodes for long-term ECG monitoring. IEEE Transactions on Biomedical Engineering. 2012;**59**:1472-1479. DOI: 10.1109/TBME.2012.2190288

[22] Abu-Saude M, Consul-Pacareu S, Morshed BI. Feasibility of patterned vertical CNT for dry electrode sensing of physiological parameters. In: 2015 IEEE Topical Conference on Biomedical Wireless Technologies, Networks, and Sensing Systems (BioWireleSS); 2015. pp. 1-4. DOI: 10.1109/BIOWIRELESS.2015.7152124

[23] Abu-Saude M, Morshed BI. Polypyrrole (PPy) conductive polymer coating of dry patterned vertical CNT (pvCNT) electrode to improve mechanical stability. In: 2016 IEEE Topical Conference on Biomedical Wireless Technologies, Networks, and Sensing Systems (BioWireleSS); 2016. pp. 84-87. DOI: 10.1109/BIOWIRELESS.2016.7445569

[24] Lee SM, Lee JH, Lee S. Skin-like electronics based on CNT/PDMS composite for long term and unconscious sensing of biosignals. In: 2015 IEEE 15th International Conference on Nanotechnology (IEEE-NANO); 2015. pp. 1155-1158. DOI: 10.1109/NANO.2015.7388829

[25] Peng H, Liu J, Tian H, Xu B, Dong Y, Yang B, et al. Flexible dry electrode based on carbon nanotube/polymer hybrid micropillars for biopotential recording. Sensors and Actuators A: Physical. 2015;**235**:48-56. DOI: 10.1016/j.sna.2015.09.024

[26] Nuwer MR, Comi G, Emerson R, Fuglsang-Frederiksen A, Guérit J, Hinrichs H, et al. IFCN standards for digital recording of clinical EEG. Electroencephalography and Clinical Neurophysiology. 1998;**106**:259-261. DOI: 10.1016/s0013-4694(97)00106-5

[27] Ruffini G, Dunne S, Farres E, Watts PCP, Mendoza E, Silva SRP, Grau C, Marco-Pallares J, Fuentemilla L, Vandecasteele B. ENOBIO—First tests of a dry electrophysiology electrode using carbon nanotubes. In: 2006 International Conference of the IEEE Engineering in Medicine and Biology Society; 2006. pp. 1826-1829. DOI: 10.1109/IEMBS.2006.259248

[28] Lin C, Lee Y, Yeh S, Fang W. Flexible carbon nanotubes electrode for neural recording. Biosensors and Bioelectronics. 2009;**24**:2791-2797. DOI: 10.1016/j.bios.2009.02.005

[29] Green RA, Suaning GJ, Poole-Warren LA, Lovell NH. Bioactive conducting polymers for neural interfaces application to vision prosthesis. In: 2009 4th International IEEE/EMBS Conference on Neural Engineering; 2009. pp. 60-63. DOI: 10.1109/ner.2009.5109234

[30] Mantione D, Del Agua I, Schaafsma W, Diez-Garcia J, Castro B, Sardon H, et al. Poly(3,4-ethylenedioxythiophene):glycosaminoglycan aqueous dispersions: Toward electrically conductive bioactive materials for neural interfaces. Macromolecular Biosciences. 2016;**16**:1227-1238. DOI: 10.1002/mabi.201600059

[31] Green R, Abidian MR. Conducting polymers for neural prosthetic and neural interface applications. Advanced Materials. 2015;**27**:7620-7637. DOI: 10.1002/adma.201501810

Chapter

Inverse Kinematics Solution for Piecewise Continuum Hyper Redundant Robot Using Vector-Space Representation

Harsh Bhatt, Saurin Sheth, Pramit Dutta and Naveen Rastogi

Abstract

Hyper-redundant robots have found their applications in many areas due to their dexterity and flexibility. Robots that are analogous in the morphology of snakes or elephant trunks can be used for inspection of confined spaces and remote locations. Due to the very high number of degrees of freedom, solution of inverse kinematics problem is difficult to obtain. In this paper, the possibility of solving the inverse kinematics problem of a piecewise continuum hyper-redundant using vector-space representation is evaluated. As continuum robots have a large number of links compared to other categories of hyper-redundant robots, it is important to identify the position and orientation of each link in order to obtain the desired shape. The algorithm that is discussed in this paper is based on vector-space representation where each link of a robot is represented by a vector. The extrinsic approach is used for controlling the positions of each link. The complete robot is divided into 4 sections, each consisting of 10 links. Thus, for up-down and left–right movement of each sections, in total 16 motors and hence 16 wires are used to control the robot. The control algorithm giving results of inverse kinematics problem in the form of wire lengths is prepared in MATLAB and its simulation is also discussed in the paper.

Keywords: hyper-redundant robot, wire-driven, bio-inspired, inverse kinematics, control algorithm, continuum robot

1. Introduction

Hyper-redundant robots are widely used in the field of medical, rescue, industries and for inspection of remote areas and confined spaces. For the application in medical or in confined spaces like nuclear reactors or any other, the precise and accurate position of each link is essential.

There are basically three methods to find the inverse kinematics of hyper-redundant robots, which are geometrical, analytical and hybrid. A geometrical method of a piecewise continuum hyper-redundant robot is discussed in [1, 2]. Assuming constant curvature, geometrical relations between bending angle and wire length is established. Analytical approach to solve the inverse kinematics problem is discussed in [3]. A hybrid approach, combining numerical and analytical

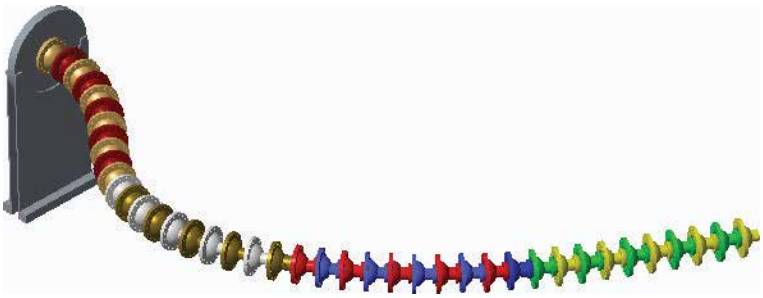

Figure 1.
Proposed design of hyper-redundant robot.

approach is discussed in [4]. Hyper-redundant robots are widely used in the medical field. Geometrical modelling of a bending section with one or two subsections at the end of an ureteroscope for urological surgery is discussed in [5]. Some other various methods include the numerical method [6], triangulation methods [7], multi-objective genetic alorithm [8], and Artificial Neural Network (ANN) [9, 10].

In this paper, the control algorithm to find the inverse kinematics solution using vector-space representation is proposed. Each link of piecewise continuum robot is represented by a vector in 3D space. There are 4 sections assumed in the robot and each section has 10 links. Thus, 40 vectors representing 40 links will be controlled using this algorithm.

Here, all the links are controlled with a group of wires. At the end of one section, four wires are attached. A motor is connected to the other end of the wires to control up-down and left–right movement of robot by pulling or releasing the wire. For another section, a group of four wires is connected at an offset of 22.5° with respect to first group and similarly all other sections are connected with wires. So, for 4 sections, 16 wires are connected to 16 motors. The solution of the inverse kinematics problem includes the length of all the 16 wires for any particular shape of robot.

Figure 1 shows the proposed design of a piecewise continuum hyper-redundant robot.

2. Control algorithm and inverse kinematics

From the literature review, it is observed that the geometrical approach to solve the inverse kinematics problem of hyper-redundant robot is more accurate among other approaches. Here, the geometrical approach is used along with vector-space representation. Each link of the hyper-redundant robot is represented by a vector where vector length is equal to the distance between two consecutive links. The direction of the first vector in the xyz-plane can be controlled and after orienting it at any direction, when the robot moves forward, the first vector will move in the same direction it has been set to and each vector will follow that direction until direction of first vector is changed. After changing the direction of first vector at any point, all following vectors will also change their direction from that particular point only. Thus, this algorithm is also called "Follow the leader" type algorithm.

Figure 2 shows the sequential movement of 4-links discrete type hyper-redundant robot in a simulation workspace.

In a continuum type robot, one common assumption is made which is proved in [11] and that is Constant Curvature Assumption. It is assumed that whenever a continuum arm rotates and takes any bending position, all the links of the robot

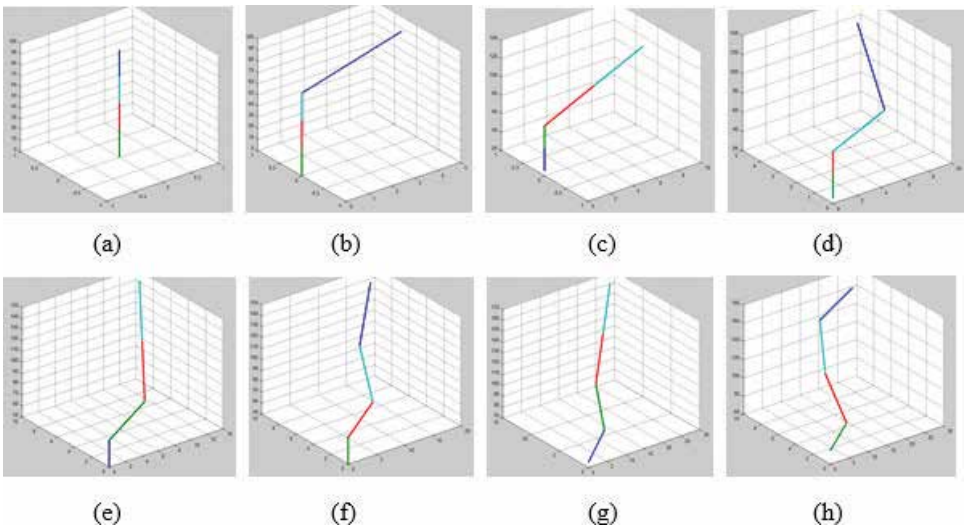

Figure 2.
Sequential movement of 4-link discrete robot: (a) initial position; (b) rotation of last link with respect to X-axis by 10° anti-clockwise; (c) move one step forward; (d) rotation of last link with respect to Y-axis by 10° anti-clockwise; (e) move one step.

bends at the same angle. Total bending angle can be calculated by multiplying the angle between two consecutive links and the number of links. After taking constant curvature assumption into consideration, a new control algorithm is prepared for 4 sections where each section contains 10 links. Here, each link is represented by a vector and 10 vectors make a group of vectors which represents a section. As shown in **Figure 3**, the direction of the first section can be controlled and when the robot moves forward, each section will follow the direction of its leader section.

A Continuum Type Hyper-redundant Robot is more flexible and dexterous compared to a Discrete Type Robot. And that also makes the solution of inverse kinematics problem of continuum robot more complicated than in the discrete robot. Using the vector-space discussed here, an inverse kinematics solution for continuum robot is obtained.

While solving the inverse kinematics problem of the hyper-redundant robot, the final results that needed to be obtained are the change in wire lengths for any desired position of robot. Here, change in wire lengths is calculated with the help of vector lengths. Whenever any vector (either first vector or following vector) changes its direction, its length in the x,y and z direction changes. These changes in lengths of vectors are used to calculate the length of the Top-Bottom and Left–Right wires by establishing geometrical relations between positions of vectors and wires. To make the calculation easy, the whole wire is divided into numbers of segments equal to the number of links. How each length of each segment of wires is calculated is shown in **Figure 4**.

Calculations are done for piecewise continuum type hyper-redundant robot considering constant curvature assumption.

Change in length of both inner and outer wires between two consecutive links:

$$L_{left} = L_0 - (d/2)^* \sin\theta$$

$$L_{right} = L_0 + (d/2)^* \sin\theta$$

where, L_0 = distance between two links on centerline.

Here, consider L_0 as our vector length.

In this arrangement, the positions of four wires of each section are different. Four wires of section 2 are offset to 22.5° from wires of section 1 as shown in **Figure 5**.

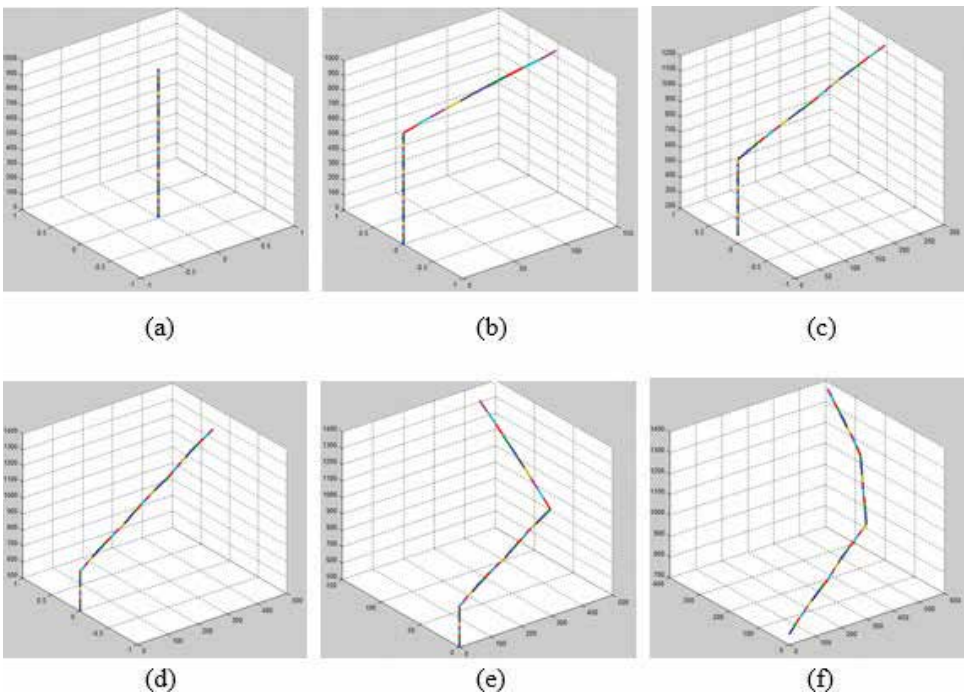

Figure 3.
Sequential movement of continuum robot: (a) initial position; (b) section-4 rotated with respect to X-axis by 10° anti-clockwise; (c) move one step forward; (d) move one more step forward; (e) rotate section-4 with respect to Y-axis by 10° anti-clockwise.

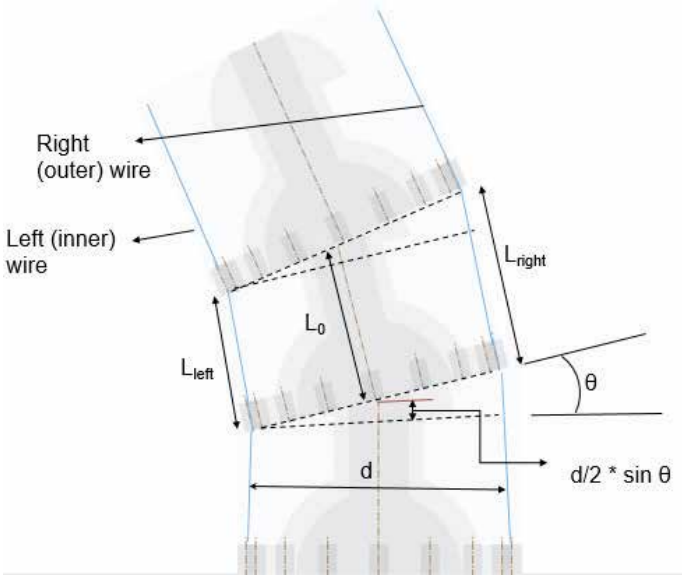

Figure 4.
Geometrical relation between vector and wire length.

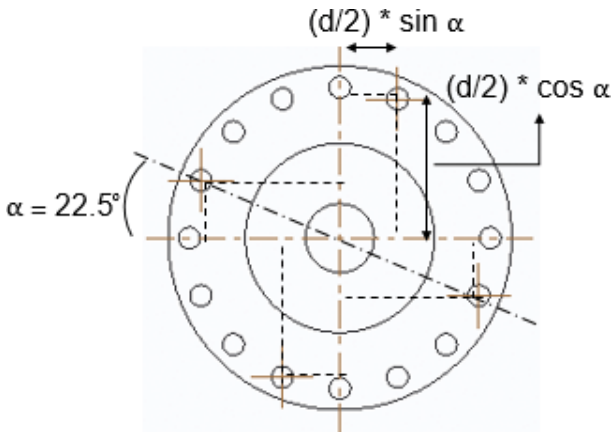

Figure 5.
Offset positions of wires in section-2.

Here, for vertical movement of section 2, both top and left wires need to be pulled and the bottom and right wires need to be released.

The amount of extra length change due to wire offset will be $(d/2)^* \cos\alpha^* \sin\theta$ in the wires for their respective assigned motions (Top-Bottom wires for vertical motion and Left–Right wires for horizontal motions) and $\{(d/2) - (d/2)^* \sin\alpha\}^* \cos\theta$ in other two wires (Top-Bottom wires for horizontal motion and Left–Right wires for vertical motions).

After offset in wire positions is considered, the change in wire lengths of all four sections is as follows:

Section 1: Vertical or Horizontal movement

$$L1_{Bottom-Top} = L_0 \pm (d/2)^* \sin\theta.$$

$$L1_{Left-Right} = L_0 \pm (d/2)^* \sin\varphi.$$

Section 2: Vertical movement

$$L2_{Bottom-Top} = L_0 \pm (d/2)^* \sin\theta^* \cos\alpha.$$

$$L2_{Left-Right} = L_0 \pm (d/2)^* \sin\varphi^* \sin\alpha \pm \{(d/2) - (d/2)^* \cos\alpha^* \sin\theta\}.$$

Section 2: Horizontal movement

$$L2_{Bottom-Top} = L_0 \pm (d/2)^* \sin\theta \pm \{(d/2) - (d/2)^* \cos\alpha^* \sin\varphi\}.$$

$$L2_{Left-Right} = L_0 \pm (d/2)^* \sin\varphi^* \cos\alpha.$$

Section 3: Vertical movement

$$L3_{Bottom-Top} = L_0 \pm (d/2)^* \sin\theta^* \cos(2\alpha).$$

$$L3_{Left-Right} = L_0 \pm (d/2)^* \sin\varphi^* \sin(2\alpha) \pm \{(d/2) - (d/2)^* \cos(2\alpha)^* \sin\theta\}.$$

Section 3: Horizontal movement

$$L3_{Bottom-Top} = L_0 \pm (d/2)^* \sin\theta \pm \{(d/2) - (d/2)^* \cos(2\alpha)^* \sin\varphi\}.$$

$$L3_{Left-Right} = L_0 \pm (d/2)^* \sin\varphi^* \cos(2\alpha).$$

Section 4: Vertical movement

$$L4_{Bottom-Top} = L_0 \pm (d/2)^* \sin\theta^* \cos(3\alpha).$$

$$L4_{Left-Right} = L_0 \pm (d/2)^* \sin\varphi^* \sin(3\alpha) \pm \{(d/2) - (d/2)^* \cos(3\alpha)^* \sin\theta\}.$$

Section 4: Horizontal movement

$$L4_{Bottom-Top} = L_0 \pm (d/2)^* \sin\theta \pm \{(d/2) - (d/2)^* \cos(3\alpha)^* \sin\varphi\}.$$

$$L4_{Left-Right} = L_0 \pm (d/2)^* \sin\varphi^* \cos(3\alpha).$$

3. MATLAB program

These formulas of length calculations are programmed in MATLAB with the control algorithm that was used for continuum robot and real-time simulation. It means for any movement of robot, the length of all 16 wires has been calculated. Some results of this program are as follows:

In **Figure 6**, the robot moves in only one plane: yz–plane. So, from the matrix indicating wire length, it can be observed that left–right wires of section 1 are not

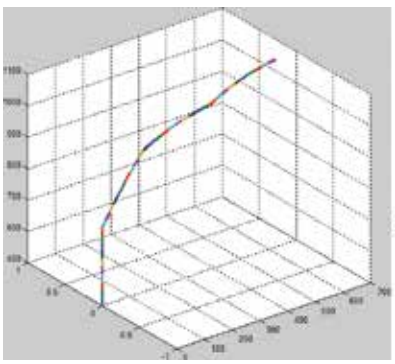

```
l_final =

   993.89      1000      1006.1      1000
   744.36    748.13      755.64    751.87
   497.84    498.73      502.16    501.27
      250       250         250       250
```

Figure 6.
Continuum robot in single plane and respective wire lengths.

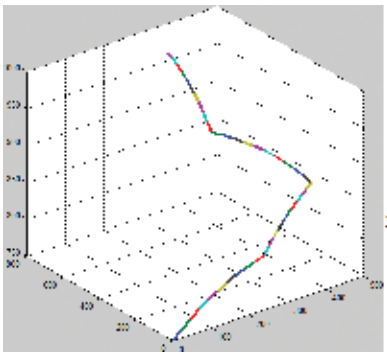

```
l_final =

   1038.9    1029.1    1032.2    1041.8
   786.63    788.05    783.83    782.41
   570.12    579.91    590.34    600.55
   240.14    247.66    254.41    262.14
```

Figure 7.
Random movement-1 with wire lengths.

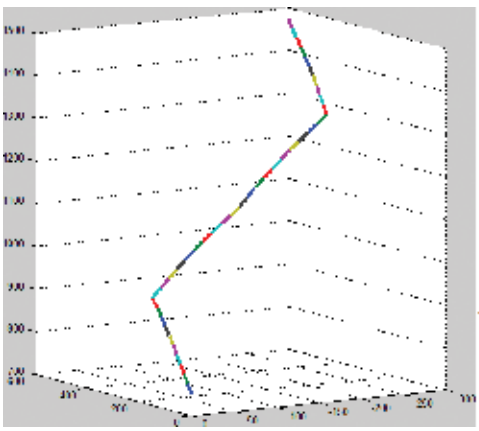

```
l_final =

   1011.1    1012.2    1012.2    1011.1
   761.31    765.2     766.96    765.07
   511.07    512.67    515.25    515.1
   238.88    241.05    251.17    258.33
```

Figure 8.
Random movement-2 with wire lengths.

changing while in another section, the left–right wire lengths are changing with top-bottom wires. In **Figures 7** and **8**, two random positions of the robot are shown and wires length to obtain that position are shown.

4. Conclusion

In this paper, the inverse kinematics solution of piecewise continuum hyper-redundant robot using vector-space representation is discussed. A continuum robot is considered for calculation as having 4 sections, each consisting of 10 links. Considering the constant curvature assumption, the control algorithm to calculate the wire lengths of 16 wires controlling up, down, left and right movement of each sections is discussed. The algorithm is prepared in such a way that to enter any confined space just the position of first link needs to be controlled and all other links will follow it. A camera can be mounted on the first link to monitor the movement of the robot and to observe the space where robot is entering. Geometric relationships between each link is considered for calculation and hence the position and orientation of each link is dependent on the position of the previous link. The algorithm is prepared in MATLAB and the simulation of movement of the robot along with the calculation of matrix of wire lengths is also presented.

DOI: http://dx.doi.org/10.5772/intechopen.81083

Author details

Harsh Bhatt[1*], Saurin Sheth[2], Pramit Dutta[3*] and Naveen Rastogi[3]

1 Mechanical Department, GMIT, Bhavnagar, India

2 Mechatronics Department, GCET, Vallabh-Vidyanagar, India

3 RHRTD Division, Institute for Plasma Research (IPR), Gandhinagar, India

*Address all correspondence to: hubhatt1994@gmail.com and pramitd@ipr.res.in

References

[1] Li Z, Du R. Design and implementation of a biomimetic wire-driven underactuated serpentine manipulator. Transaction on Control and Mechanical Systems. 2012;**1**(6):250-258

[2] Li Z, Du R. Design and analysis of a bio-inspired wire-driven multi-section flexible robot: Regular paper. International Journal of Advanced Robotic Systems. 2013;**10**:1-11

[3] Neppalli S, Csencsits MA, Jones BA, Walker ID. Closed-form inverse kinematics for continuum manipulators. Advanced Robotics. 2009;**23**(15):2077-2091

[4] Ananthanarayanan H, Ordóñez R. Real-time inverse kinematics of (2n + 1) DOF hyper-redundant manipulator arm via a combined numerical and analytical approach. Mechanism and Machine Theory. 2015;**91**:209-226

[5] Lei M, Du R. Geometry modeling and simulation of the wire-driven bending section of a flexible ureteroscope. In: Proceedings of the World Congress on Engineering and Computer Science, Vol. II; 2011

[6] Wang H, Jia Y, Xi N, Buether J. An online motion planning algorithm for a 7DOF redundant manipulator. In: Proceedings of the International Conference on Robotics and Biomimetics; 2010. pp. 1057-1062

[7] Song W, Hu G. A fast inverse kinematics algorithm for joint animation. Procedia Engineering. 2011;**24**:350-354

[8] Grac M, Machado JAT, Azevedo-perdicoúlis T. A multi-objective approach for the motion planning of redundant manipulators. Applied Soft Computing. 2012;**12**:589-599

[9] Feng Y. Inverse kinematics solution for robot manipulator based on neural network under joint subspace. International Journal of computer communication & control. 2012;**7**(3):459-472

[10] Song L. RBF networks-based inverse kinematics of 6R manipulator. International Journal of Advanced Manufacturing Technology. 2005;**26**:144-147

[11] Xu K, Simaan N. Analytic formulation for kinematics, statics, and shape restoration of multibackbone continuum robots via elliptic integrals. Journal of Mechanisms and Robotics. 2010;**2**(1):11006

Chapter

Metrological Measurements of Water Lubricated Hydrodynamic Bearings

Ketan Tamboli

Abstract

For a hydrodynamic journal bearing, it is essential to ensure that the proper dimensional accuracy is maintained during manufacture and also during operation so as to ensure the best performance. In the present work, an application of nuclear reactor feed pump bearing is considered which uses water as a lubricant. Four design procedures are applied to three bearings with different L/D ratio. The bearings and journals are manufactured and checked for the dimensional attributes. The purpose of assessing the geometry is to ensure the hydrodynamic lubrication during its operation. The dimensional checks carried out are: (1) external diameter of journal, (2) internal diameter of bearing, (3) surface roughness measurements, (4) roundness for both journal and bearing. A sample observation for diameters using the optical tool microscope with an accuracy of 1.0 μm for end plane and mid plane is presented. The surface roughness at different locations is measured using TALYSURF with an accuracy of 0.1 μm. The roundness is measured using TALYROND with an accuracy of up to 0.1 μm and is inspected for ovality. A dial comparator with an accuracy up to 1.0 μm is used at different planes axially and circumferentially. The comparison is made with the design specification and actual available dimensions.

Keywords: hydrodynamic bearing, water lubrication, metrology, measurement, dimensions

1. Introduction

In most applications such as pumps, turbines, machine tools and engines, the journal bearings use oil as a lubricant. However, if in applications where the water is a process fluid and if oil lubricated plain bearings are used, then the size of the machine increases due to usage of seals etc. If water i.e. the process fluid itself can be used as the lubricant then the size reduces to a great extent as seals etc. are not required. The advanced boiler reactor is an example of such an application. The feed pumps used here house the bearings which can be water lubricated as the process fluid is water only. The material of the bearing and journal need to be changed and the clearances in such applications are to be maintained accurately.

The materials of the journal and the bearing are required to be changed as corrosion needs to be avoided. Wang et al. [1] and Zhongqian et al. [2] discussed

the materials to be used and the effect of friction and wear characteristics on the polymer materials. Various researchers [3–8] have experimented with water lubricated bearings used in different applications. The effect of misalignment and other geometrical parameters are studied by Sharma et al. [9] and Elsharkawy [10]. It was emphasized that the performance of the bearing suffers if the dimensions are not maintained in the journal and bearing. Also, the effect of misalignment is discussed resulting in unexpected variation of various variables. The dimensional accuracy of the bearing asks for structured measurements with highly accurate instruments. In this paper, a water lubricated journal bearing of different sizes is considered for the nuclear reactor application. These bearings and journals are designed using (1) ESDU [11], (2) Reason and Narang [12], (3) Cameron [13] and (4) Raimondi and Boyd [14] methods. The methods are applied to three bearings with different L/D ratios. Based on the outcome of designs, the bearings are manufactured and checked for the dimensional attributes. The radial clearance is a critical parameter which directly has an effect of load carrying capacity. As the clearance increases, the capacity decreases. The clearance depends on the outer diameter of the journal and inner diameter of the bearing.

2. Measurement of bearings and journals

In the following sub sections, the methodology of measurements and use of instruments are shown. The bearings (**Figure A1**) and journals are manufactured as per design outputs and are measured for dimensional precision.

2.1 Measurement of bearing sizes

Three parameters: (1) internal diameter, (2) surface roughness and (3) roundness of internal surface were measured critically. As **Figure A2** shows, the internal diameter was measured taking six observations each at 30° intervals circumferentially and axially at three planes (two end planes and one central plane) giving a total of 18 readings for each bearing. The internal diameters at the end planes were measured using an optical tool makers microscope with an accuracy of 1.0 μm. While the central plane internal diameter, being not possible to measure with an optical tool makers microscope, an optical comparator with a 1.0 μm accuracy was used. The sample readings are shown in **Table 1** for bearing 3. **Table 2** shows the summary of all the three bearing diameters measured.

Sr. no. (angular position)	Plane 1 (end plane) Φ, mm	Plane 2 (central plane) Φ, mm	Plane 3 (end plane) Φ, mm
1	61.034	61.032	61.056
2	61.038	61.029	61.062
3	61.012	61.021	61.016
4	61.016	61.019	61.072
5	61.048	61.028	61.034
6	61.028	61.029	61.048

Table 1.
Sample observations for internal diameter for bearing 3.

	Average dia. (mm)	Maximum dia. (mm)	Minimum dia. (mm)
Bearing 1	65.047	65.060	65.016
Bearing 2	61.067	61.076	61.014
Bearing 3	61.035	61.072	61.012

Table 2.
Summary of bearing diameters measurements.

2.2 Measurement of surface roughness and roundness

For the measurement of the surface roughness (as shown in **Figures A3** and **A5**) at different locations, *TALYSURF* with an accuracy up to 0.1 μm was used at two locations axially and three locations circumferentially. The axial travel was 6.4 mm of the stylus and vertical magnification for the plot (graph) was selected as 1000 and horizontal magnification as 50. The maximum surface roughness found for bearing 1, 2 and 3 were 0.89, 1.58, and 1.63 μm respectively.

For checking the roundness, *TALYROND*, with an accuracy up to 0.1 μm was used. **Figure A3** shows the locations for checking roundness of internal diameter surface. The ovality measured for bearings 1, 2 and 3 are 5, 10 and 5 μm respectively (**Table 2**).

2.3 Measurement of journal sizes

The measurement procedure for measuring the outer diameter is slightly different from the earlier one followed for bearings, though, the locations where measurements are made as shown in **Figure A5** are similar for the bearing. For the measurement of the outer diameter, a dial comparator with an accuracy up to 1.0 μm was used. Similar to the bearing locations, the observations were taken in axial directions at three different planes (two end planes and one central i.e. mid plane). Circumferentially, six readings each at 30° intervals were taken. This means, there were 18 readings for the diameter for each journal (**Figure A4**).

The surface roughness and ovality measurements (**Figure A6**) were carried out using a similar procedure and instruments as in the case of bearings discussed earlier. **Table 3** summarizes the extracted results from the measurement of journals. **Table 4** compares the specified (by design) clearances versus actual obtained clearances.

Journal	Outer diameter, mm			Surface roughness, Ra_{max}	Ovality, microns
	Avg.	Max.	Min.		
Journal 1 (L/D = 1.0)	64.992	65.006	64.988	0.87	5
Journal 2 (L/D = 0.77)	61.017	61.036	60.996	0.57	5
Journal 3 (L/D = 1.0) (stainless steel)	60.802	60.850	60.750	1.07	100 (too large)
Journal 4 (L/D = 1.0) (PTFE)	60.692	61.040	59.001	2.66	10

Table 3.
Results from measurement of journal.

Bearing/journal	Average diameter, mm	Average radial clearance obtained	Radial clearance specified
Bearing 1 (L/D = 0.5)/journal 1	65.047 64.992	27.5	32.5
Bearing 2 (L/D = 0.77)/journal 2	61.067 61.017	25.0	38.3
Bearing 3 (L/D = 1.0)/journal 3 (S.S.)	61.035 60.802	116.5 (too large)	30.62
Bearing 4 (L/D = 1.0)/journal 4 (PTFE)	61.035 60.970	32.5	30.62

Table 4.
Clearances from measurements.

3. Conclusions from measurement

From the measurements of the bearings and journals, the following conclusions are drawn.

1. From the measurement of the external diameter of journals and the internal diameter of bearings, considering the average diameter (out of all 18 observations as shown in **Table 3**) the clearances are obtained accordingly.

2. The surface roughness values, as can be seen from **Table 3**, are satisfactorily achieved for journals 1, 2 and 3. Journal 4, the material being PTFE, has the limitation for grinding and so the desired surface roughness could not be achieved. However, with best possible combination of feed and depth of cut, a considerably good finish is achieved.

3. The ovality checks show that the ovality for journal 3 of stainless steel is large, possibly, due to certain error in fixing it on the lathe.

4. Discussion

The journal and bearing combinations resulting into high clearances are not recommended as the load carrying capacity will be greatly reduced. Also, the ovality needs to be within range as it also has a direct impact (an increase in ovality leads to a decrease in performance). The measurements of OD, ID, surface roughness and ovality prove that the specified dimensions of the design are mostly maintained during manufacturing except in one or two cases. However, the user or application engineer needs to ensure that these geometric parameters are maintained during running condition of the bearing, which is a challenging task.

Acknowledgements

The authors wish to express gratitude to the authorities of IIT Delhi for permission to use the workshop and metrology laboratory for fabrication and measurement of journals and bearings.

A. Appendix

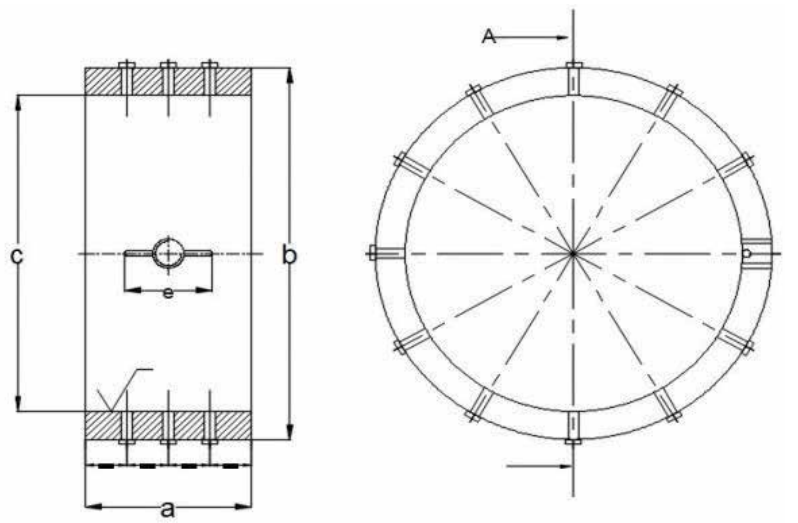

Figure A1.
Two views of bearing with rivets. The rivets are to be used for temperature measurements.

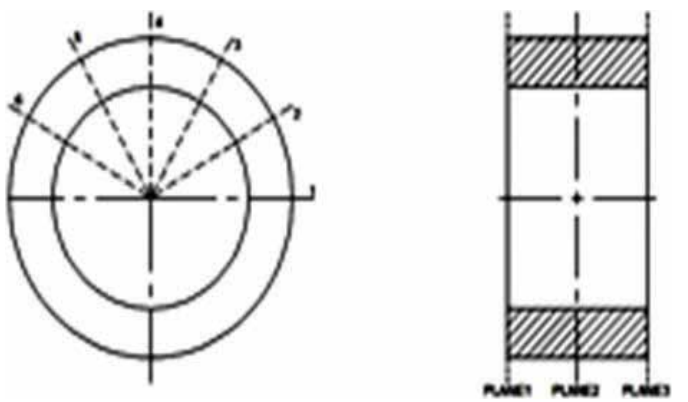

Figure A2.
Three planes 1, 2, 3 and radially 30° intervals for ID measurements of bearing (total 18 readings).

Figure A3.
Three radial locations each at 120° in one plane and to be measured in three planes for bearing (total 9 readings).

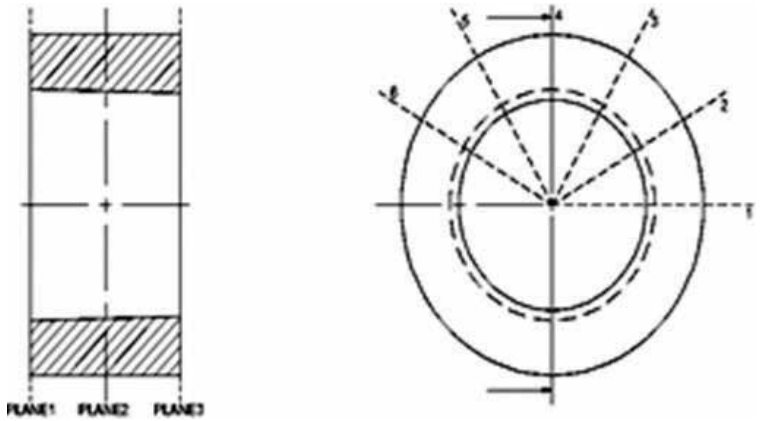

Figure A4.
Three planes 1, 2, 3 and radially 30° intervals for OD measurements of journal (total 18 readings).

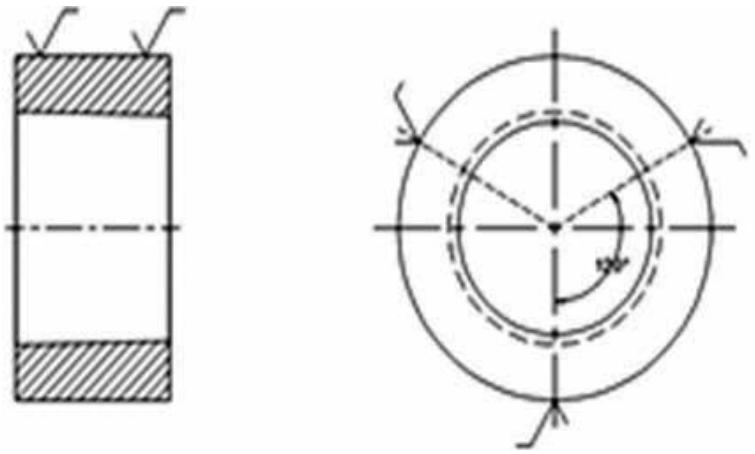

Figure A5.
Three radial locations each at 120° in one plane and to be measured in three planes for journal (total 9 readings).

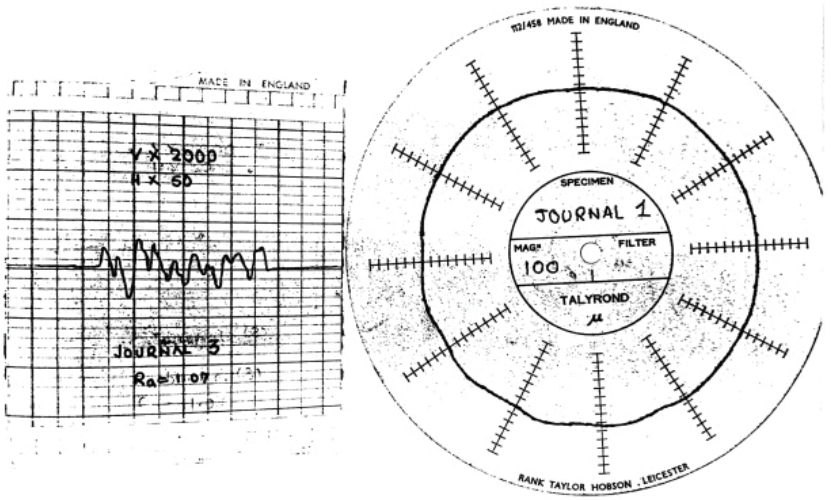

Figure A6.
Sample observation for linear surface roughness measurement and ovality measurement.

Author details

Ketan Tamboli

Mechatronics Department, G H Patel College of Engineering and Technology, V V Nagar, Gujarat, India

*Address all correspondence to: ketantamboli2000@yahoo.com

References

[1] Wang X, Haiye L, Wei H. Development status and trend of the water lubrication materials. Journal of Mechanical Engineering and Automation. 2012;**4**:5-8

[2] Zhongqian Y, Hailin G, Shouqing X, Dongming H. Polymer Materials of Water Lubrication Friction and Wear Characteristics. Shanghai: Shanghai Institute of MC; 2012

[3] Gennan G. The ship water lubricated bearing use study. Jiangsu Ship. 2004;**21**:17-20

[4] Shiwei Y, Wang Y, Wang J, et al. Water lubrication rubber bearing friction behavior and experimental study. Journal of Marine Science and Technology. 2009;**31**(12):32-35

[5] Cheng Z, Jiaxu W, Jiangbo Y, Ke X. Rubber layer thickness and hardness of water lubricated integral bearing friction factor. Journal of the Influence of Lubrication and Sealing. 2006;**174**(2):40-41

[6] Pan P. Several kinds of water lubricated stern bearing material tribology experiment research [thesis]. Wuhan: Wuhan University of Science; 2013

[7] Tamboli K, Athre K. Experimental investigations on water lubricated bearing. Procedia Technology. 2016;**23**:68-75

[8] Cabrera DL, Wooley NH, Allanson DR, Tridimas YD. Film pressure distribution in water-lubricated rubber bearings. Proceedings of the Institution of Mechanical Engineers, Part J: Journal of Engineering Tribology. 2005;**219**(2):125-132

[9] Sharma S, Hargreaves D, Scott W. Journal bearing performance and metrology issues. Journal of Achievements in Materials and Manufacturing Engineering. 2009;**32**(1):98-103

[10] Elsharkawy AA. Effects of misalignment on the performance of flexible porous journal bearing. Tribology Transactions. 2008;**46**(1):119-127. DOI: 10.1080/10402000308982608

[11] Engineering Science Data Unit (ESDU), Item No.: 66023, List. of Mech. Engineers, London. 1982

[12] Reason BR, Narang P. Rapid design and performance evaluation of steady state journal bearings—A technique amenable to programmable hand calculator. ASLE Transactions. 1982;**25**(4):429-444

[13] Cameron A. The Principles of Lubrication. London: Longman Green & Co. Ltd.; 1966

[14] Raimondi AA, Boyd J. Applying bearing theory to the analysis and design of journal bearings. Journal of Applied Mechanics. 1951;**73**:298-316

Chapter

Identification of Wear Condition in IC Engine by Wear Debris Monitoring

Mohit Kumar, R.B. Sharma, Kuldeep Chaudhary and Ranjeet Singh

Abstract

The objective of the present work is to develop a simple technique to predict and quantify the presence of wear condition in an IC engine based on wear debris monitoring. Wear debris are formed in the engine oil mostly due to friction between two parts of engine and/or extraction of material from the various parts of the engine. A test rig has been developed based on the Ferrography principle to perform the experimental investigation for engine oil analysis. A series of engine oil samples from an IC engine during different time intervals were considered and the wear debris analysis was performed based on total particle concentration of different material (ferrous material and non-ferrous material), size of wear debris and visual inspection of particles. The results demonstrate that the concentration, size and visual inspection of ferrous and non-ferrous debris, which was present in the oil correlated well with the severity of the condition of the IC engine. This is also useful to diagnosis the fault present in the engine.

Keywords: wear monitoring, IC engine, engine oil, ferrography, wear debris analysis

1. Introduction

IC engines are mostly used in the automotive sector due to their better fuel economy and low maintenance. Condition monitoring of the IC engine or its various components is very important for its appropriate functioning. The various studies that are available in the literature for condition monitoring of the machine components use different techniques such as vibration analysis, acoustic emission, wear debris analysis, and thermography. Some studies are also available regarding the modeling of acoustic emission, which are significant to comprehend the concrete mechanism of the generation of acoustic emission during the operating condition of the gear pair as well as rolling element bearing [1–3]. IC engines suffer from several problems such as wear debris, high levels of exhaust NOx, particulate matter and black smoke [4]. These problems are generated due to improper combustion, oil burning and friction between two parts of engine. The lubrication system used in IC engines is splash lubrication system, which is used to lubricate all parts of the engine. In the lubrication system, the oil flows through the splash system in which the crankshaft rotates which in turn splashes the oil on the various parts of the engine. The oil first lubricates the crankshaft then goes into the main gallery and

proceeds by connecting rod to piston and then cylinder. The oil then lubricates the camshaft proceed by rocker arm and then the valves. After lubricating the parts of engine, the oil flows back to the sump through the oil gallery [5]. The oil lubricating the engine parts carries the wear debris back into the sump.

The wear debris analysis technique is extensively used in monitoring the condition of an IC engine, machine and gearbox. Many researchers use oil-monitoring techniques for condition monitoring such as the ferrography technique [6], grey system theory [7, 8], FTIR [9], rotary particle depositor (RPD), particle quantifier (PQ) and spectrometric oil analysis. Ferrography is used to quantify the amount of wear particles within a given oil sample and to conduct microscopic analysis of that debris in order to identify its size and shape [10]. Spectrometric oil analysis can determine the residual life of IC engines and gearboxes by performing tests on the engine oil at regular intervals. The tests performed on the engine oil reveal the chemical composition of any metal particles suspended in the oil samples, any pre-time wear of engine parts can be identified and preventive maintenance can be done [11]. The relationship between oil monitoring information and the residual life is established, which states that the predicted residual life may be proportional to the wear increment measured by the oil analysis. In spectrometric analysis, the metal concentration found includes many variables such as Fe, Cu and Al etcetera [12]. Color plays an important role in wear debris analysis [13, 14]. Wear can also be identified using their color features.

2. Experimental investigation

2.1 Experimental setup

Engine oil tests were carried out using a simple experimental setup, which is shown in **Figure 1**. The experimental setup consists of three chambers: the first chamber is called the magnetic chamber with turbine, second chamber is called non-magnetic chamber with turbine and last chamber is the sump chamber. The magnetic chamber consists of a circular magnet which collects the ferrous particles from the oil and after that oil is fed into the non-magnetic chamber, which collects and separates the non-ferrous particles from oil. Then the oil is passed into the

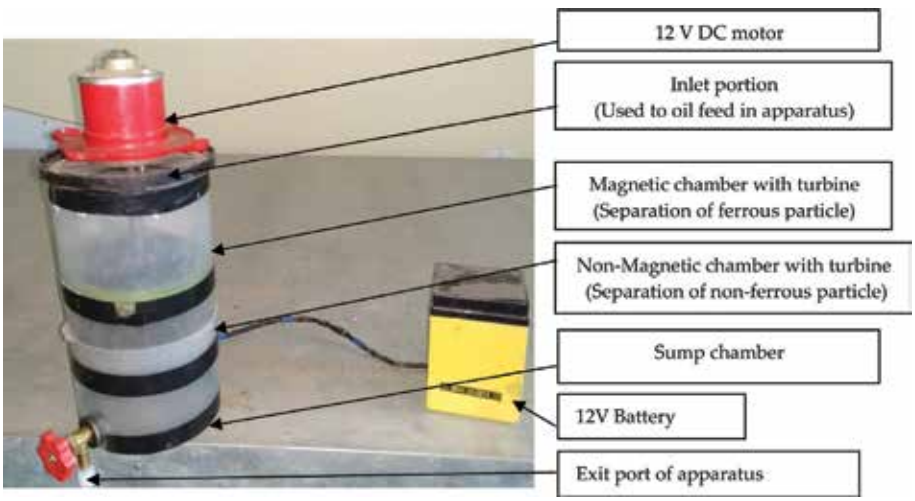

Figure 1.
Experimental set up for engine oil analysis.

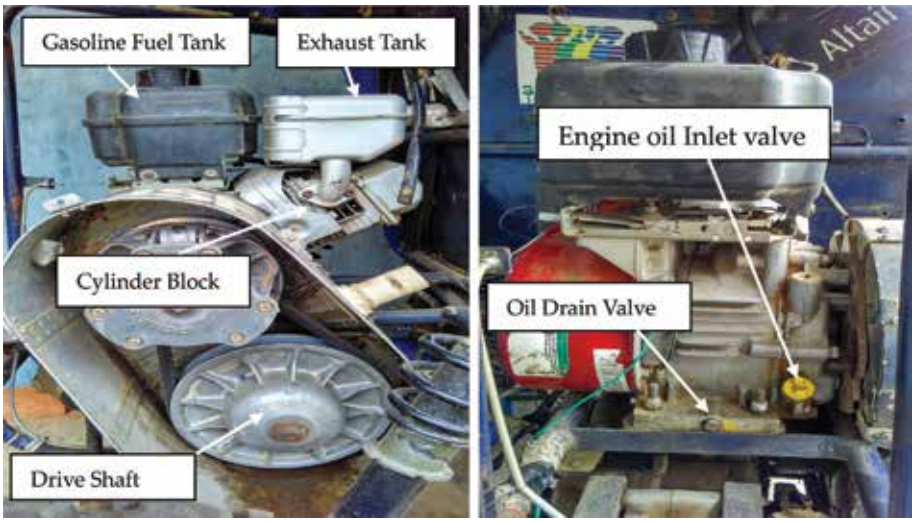

Figure 2.
10 HP SI engine.

sump chamber which collects the filtered lubrication oil. The 12-volt DC motor present at the top of the experimental setup rotates at 200–220 rpm. The 12-volt battery supplies the DC current to the motor, which in turn rotates.

2.2 Experimental procedure

A test rig has been developed based on the ferrography principle to perform the experimental investigation for engine oil analysis as shown in **Figure 1**. A series of engine oil samples from an IC engine at different time intervals of service were collected and the wear debris analysis was performed based on data obtained from the analysis of wear particles.

The engine used for the experimental investigation was a 10 HP SI engine developed by Briggs & Stratton Co. Ltd. as shown in **Figure 2**. This engine is generally used in SAE BAJA events organized by SAE INDIA. The specifications of this engine are detailed in **Table 1**.

Specification	Value	Specification	Value	Specification	Value
Type	4-Stroke	Length (in)	12.3	Fuel tank capacity (gallons)	0.8
Torque	14.50	Width (in)	17.0	Lubrication system	Splash lubrication
Engine displacement (cc)	306	Height (in)	16.4	Oil capacity (oz)	20
No. of cylinders	Single	Weight (lbs)	58.2	Oil filter	N/A
Engine configuration	Horizontal shaft	Bore (in)	2.28	Starter	Manual choke
Engine fuel	Gasoline	Stroke (in)	2.04	Air filter	Dual element

Table 1.
Engine specifications.

SAE grade	**5 W-30**	**Phosphorous, wt%**	**0.08**
Viscosity @ 100°C, cSt	11.0	Viscosity, mPa.s @ 150°C	3.1
Viscosity, @ 40°C, cSt	61.7	Pour point, °C	−42
Density @15.6°C, kg/l	0.855	Flash point, °C	230
Viscosity index	172	Temperature range	−20 to 120° F
Sulfated ash, wt%	0.8	—	—

Table 2.
Properties of engine oil.

Test sample	**Operating time (hours)**	**Weight of debris (mg)**	**Running conditions**
1	26	22	On-road
2	50	15	On-road
3	80	14	On-road
4	105	15	On-road

Table 3.
Weight of wear debris collected from oil samples at different time intervals.

The lubrication oil SAE 5W-30 has been used in the engine. The lubrication properties of engine oil at the time of beginning of experiments are detailed in **Table 2**.

To find out the wear condition of the engine, 4 engine oil samples were collected from the 10 HP Petrol engine at different intervals. The load condition and speed condition are 12.0 Nm and 4200 rpm respectively. The engine was mounted on the BAJA vehicle. The total weight of wear debris extracted from each oil sample is given in **Table 3**.

3. Results and discussion

The engine oil is the most effective tool for condition and health monitoring of an IC engine. The lubrication oil carries detailed information about the condition of the engine. In the present investigation, two types of metals were found in the engine oil, ferrous and non-ferrous. The ferrous and non-ferrous particles are identified separately with the developed experimental setup. The deposition of ferrous and non-ferrous particles in the different.

chambers of the experimental set-up are shown in **Figure 3(a)** and **(b)** respectively.

The experimental results i.e. weight of wear debris from different test or oil samples are mentioned in **Table 3**. A graph between weight of wear debris and time is presented in **Figure 4** by using experimental results which shows the wear rate of engine. The experimental results demonstrate that the wear of engine parts is high at the starting phase of the engine. As the engine continues to run during different time intervals in same running conditions, the wear of engine parts decreases and then remains almost constant as shown in **Figure 4**.

It is found that the engine parts such as the cylinder liners, camshaft, crankshaft, valve seat and rocker arms are made from ferrous material and the piston, piston head and cylinder head are made from non-ferrous material, tend to deteriorate and are shown in **Table 4**.

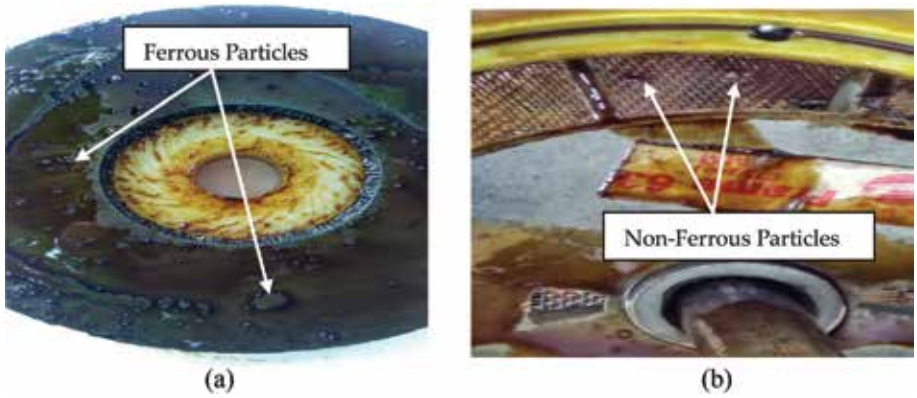

Figure 3.
Experimental setup for oil analysis: (a) magnetic chamber (ferrous particles) and (b) non-magnetic chamber (non-ferrous particles).

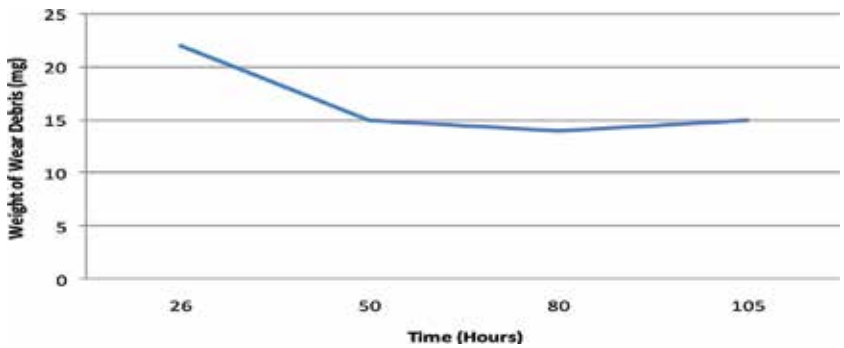

Figure 4.
Wear rate of engine.

S. No.	Particle status	Metal	Sources/deteriorated parts
1	Ferrous	Iron	Camshaft, crankshaft, valve seat, rocker arms
2	Non-ferrous	Al alloy	Piston, piston head, cylinder head

Table 4.
Various deteriorated parts of engine.

4. Conclusion

Condition monitoring of the IC engine is very significant to avoid catastrophic failures. Various techniques are available in the literature for this monitoring. This study presents an experimental investigation to identify the wear condition of an SI engine by wear debris monitoring. Experimental results demonstrate that the wear rate of the engine decreases as life of engine increases and after some time interval, it remains almost constant. The condition of the deteriorated parts of the engine are also identified.

Author details

Mohit Kumar*, R.B. Sharma, Kuldeep Chaudhary and Ranjeet Singh
RJIT, Border Security Force Academy Tekanpur, Gwalior, Madhya Pradesh, India

*Address all correspondence to: mamhooda@gmail.com

IntechOpen

References

[1] Sharma RB, Parey A, Tandon N. Modelling of acoustic emission generated in involute spur gear pair. Journal of Sound and Vibration. 2017;**393**:353-373

[2] Sharma RB, Parev A. Modelling of acoustic emission generated in rolling element bearing. Applied Acoustics. 2018;**41**:1-7. DOI: 10.1016/j.apacoust.2017.07.015

[3] Sharma RB, Parev A. Modelling of acoustic emission generated by crack propagation in spur gear. Engineering Fracture Mechanics. 2017;**182**:215-228

[4] Singh SK, Agarwal AK, Sharma M. Experimental investigations of heavy metal addition in lubricating oil and soot deposition in an EGR operated engine. Applied Thermal Engineering. 2006;**26**:259-266

[5] Ganeshan V. Internal Combustion Engine. India: Tata Mc-Graw Hill Company; 2003

[6] Roylance BJ. Ferrography—Then and now. Tribology International. 2005;**38**:857-862

[7] Wang J, Wang X. A wear particle identification method by combining principal component analysis and grey relational analysis. Wear. 2013;**304**:96-102

[8] Chen S, Li Z, Xu Q. Grey target theory based equipment condition monitoring and wears mode recognition. Wear. 2006;**260**:438-449

[9] Adams MJ, Romeo MJ, Rawson P. FTIR analysis and monitoring of synthetic aviation engine oils. Talanta. 2007;**73**:629-634

[10] Stachowiak GW, Podsiadlo P. Characterization and classification of wear particles and surfaces. Wear. 2001;**249**:194-200

[11] Bierlein JA. Particle-Size Analysis of Engine Oils: A Supplement to Spectrometric Analysis. Southern Center, Elec. Eng. Ed. (SCEEE. Inc.). Wright-Patterson AFB, Ohio 45433: Air Force Materials Laboratory; 2004

[12] Wang W, Zhang W. A model to predict the residual life of aircraft engines based upon oil analysis data. Naval Research Logistics. 2005;**52**(3):276-284

[13] Anderson DW. Wear Particle Atlas. Report No. NAEC-92-163. Naval Air Engineering Center; 1992

[14] Barwell FT, Bowen TP, Westcott VC. The use of temper colors in ferrography. Wear. 1973;**44**:235-242

Edited by Sanket N. Bhavsar, Anand Y. Joshi and Ketan M. Tamboli

The Mechatronics Department (Accredited by National Board of Accreditation, New Delhi, India) of the G H Patel College of Engineering and Technology, Gujarat, India arranged the 4th International Conference on Innovations in Automation and Mechatronics Engineering 2018, (ICIAME 2018) on 2–3 February 2018. The papers presented during the conference were based on Automation, Optimization, Computer Aided Design and Manufacturing, Nanotechnology, Solar Energy etc and are featured in this book.

Published in London, UK

IntechOpen

ISBN 978-1-83962-030-0